Soft Matter at Interfaces:

Adhesion, Wetting, and Capillary Interactions

Maarten van Heek

Soft Matter at Interfaces: Adhesion, Wetting, and Capillary Interactions | Maarten van Heek

Propositions

1. Patterning is not a significant factor for the improvement of structured adhesives. (this thesis)
2. The wetting dynamics of hydrogels are primarily determined by the surface affinity of the used polymer. (this thesis)
3. “All’s well that ends well” is in contradiction with the first law of thermodynamics.
4. For the understanding of advanced mathematics, a redesign of our counting methods is needed.
5. Collaboration is becoming a curse in industry, but it is not professed enough in academia.
6. Any PhD candidate should make at least one contribution to the ‘Journal of Failure’.
7. The current implementation of the Dutch Freedom of Information Act is a farce.
8. Income inequality in itself is a poor measure for welfare inequality.

Propositions belonging to the PhD thesis, titled ‘Soft Matter at Interfaces: Adhesion, Wetting, and Capillary Interactions’

M. van Heek

Wageningen, 07-04-2020

Soft Matter at Interfaces:

Adhesion, Wetting, and Capillary Interactions

Maarten van Heek

Thesis committee

Promotors
Prof. Dr J. van der Gucht
Professor of Physical Chemistry and Soft Matter
Wageningen University & Research

Prof. Dr J. Sprakel
Personal chair, Physical Chemistry and Soft Matter
Wageningen University & Research

Other members
Prof. Dr C.G.P.H. Schroën, Wageningen University & Research
Prof. Dr M.M.G. Kamperman, University of Groningen
Dr V. Saggiomo, Wageningen University & Research
Dr M.F. Haase, Utrecht University

This research was conducted under the auspices of the Graduate School VLAG (Advanced studies in Food Technology, Agrobiotechnology, Nutrition and Health Sciences).

Soft Matter at Interfaces:
Adhesion, Wetting, and Capillary Interactions

Maarten van Heek

Thesis
submitted in fulfilment of the requirements for the degree of doctor at
Wageningen University
by the authority of the Rector Magnificus
Prof. Dr A.P.J. Mol,
in the presence of the
Thesis Committee appointed by the Academic Board
to be defended in public
on Tuesday 4 April 2020
at 4 p.m. in the Aula.

Maarten van Heek
Soft Matter at Interfaces: Adhesion, Wetting, and Capillary Interactions
139 pages.

PhD thesis, Wageningen University, Wageningen, NL (2020)
With references, with summary in English and Dutch

ISBN 978-94-6395-294-1
DOI https://doi.org/10.18174/512765

Contents

III Colloids at anisotropically curved interfaces

Chapter 1

General introduction

Soft matter is an umbrella term in science that mostly covers the colloidal domain. This colloidal domain lives between the microscopic domain of atoms and molecules, and the macroscopic world. The name soft matter originates from the interaction strength that these materials exhibit. Compared to chemical bonds, soft matter interactions are generally weak, with interaction energies in the same order of magnitude as thermal fluctuations at room temperature. A major benefit of soft systems is the reversible nature of these interactions. However, not all is what it seems: the main thematic of this thesis is to find out how the combination of many weak interactions may result in a system that is stronger than the sum of its parts. The work described in this thesis focuses on the subdomain of soft solids interacting with or at interfaces. We work on patterned silicone rubber adhesives, where the interaction takes place at a solid-gel interface; wetting of soft solids, where interactions take place at a macroscopic gel-liquid interface, and finally the interactions of microgel or silica colloids at anisotropically curved interfaces, which display an intricate play of various soft interactions at a microscopic solid- or gel-liquid interface.

1.1 Patterned adhesives

An interesting case for soft interactions is in reusable adhesives. One of the most common applications of this is in the omnipresent sticky notes [1]. These notes have a low-tack pressure-sensitive adhesive applied to them that allows them to be attached to virtually any smooth surface. The note is then effectively held in place by Van der Waals forces. Their properties allow for facile removal and reuse, without leaving a glue residue on the substrate. However, a disadvantage of this type of material is their sensitivity to fouling of the sticky patch, due to it picking up dirt particles from the surface they are attached to. This fouling eventually leads to adhesive failure or the inability to reattach.

In order to improve these sticky notes, and reusable adhesives in general, one can turn to nature for inspiration [2–11]. One feature that many of these animals share is a phenomenon called 'contact splitting'. This describes the process of splitting a large adhesive area up in smaller subsections, schematically illustrated in Figure 1.1. One advantage of contact splitting is an increased effective surface area. This is especially obvious for spherical caps, whereas its impact decreases in the limit of infinitely flat contact patches. A second, more universal, benefit is that contact splitting also improves compliance to a rough surface; an adhesive surface with split contacts may be more flexible than a rigid surface. This means that the entire surface can achieve better alignment, while potentially allowing each individual split contact patch to align perpendicular to improve the adhesion of each individual patch.

The heaviest animal capable of holding on to its own weight on vertical or inverted surfaces without using any glue, the gecko, makes use of the same Van der Waals forces [12, 13]. Besides displaying a remarkably high adhesive strength, gecko feet are also self-cleaning [14]. This remarkable achievement is made possible due to a combination of factors, among others having a very large amount of microscopic adhesive fibrils, that can be made compliant to even rough surfaces, as well as the specific shape of these fibrils: a large amount of small forces working together creates an opportunity for an outcome that is greater than the sum of its parts.

Research into nature-inspired adhesives is ongoing, both directed at finding novel adhesives for applications in challenging environments [8, 11], as well as research into contact splitting and patterned adhesives [2, 12, 15]. But to this date, limited knowledge is available on the importance of surface hierarchy, patterns, or sample geometry, and their effects on the performance of synthetic adhesives. It is not well understood how random versus ordered, or homogeneous versus heterogenous patterns affect adhesive performance. These patterns could potentially affect stress distribution, and thereby influence crack nucleation as well as crackfront propagation.

We use patterned silicone adhesives as a model system, further supported by computer simulations. Both the macroscopic properties of the gel, such as gel strength or crosslink density and aspect ratio [3], and the interface between this patterned gel and a solid surface impact the adhesive performance of the sample. A complex adhesive interplay is the result, as the distribution of forces inside the patterned adhesive, the adhesive force of the material at the substrate, the elasticity and deformation of the gel, and the force used to detach the adhesive all play a role. For instance, a substrate patterned with relatively large features might have a large contact area, and therefore be expected to perform well in adhesive testing. However, a smaller feature size leads to effectively lower spring constant [14], a significantly more flexible and compliant adhesive, and even though the adhesive force per feature is lower, the overall performance might improve as a result of contact splitting [8, 12].

In this thesis, we attempt to answer a number of these questions regarding surface

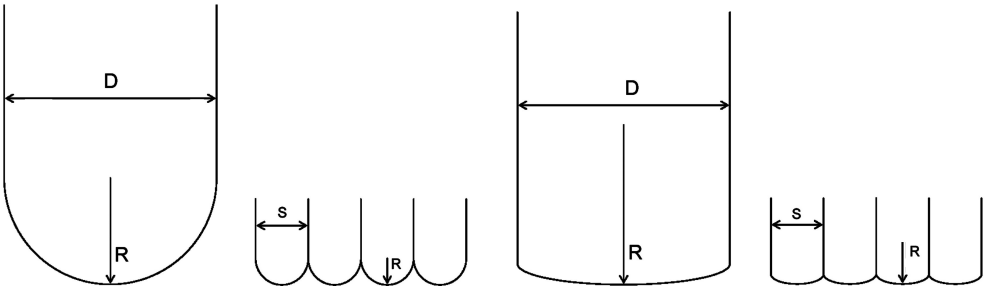

Figure 1.1 – Contact splitting, the process of subvididing a larger contact in multiple smaller sections, is commonly found in nature. Advantages include an increased effective surface area and improved compliance to rough surfaces. Adapted from [12].

hierarchy, patterning, and geometry.

1.2 Soft wetting

Other areas where soft interactions play a large role are in surface dynamics and wetting. Wetting is well understood at the macroscopic level, in particular at hard surfaces. For instance, the three-phase contact angle of an oil droplet at a solid under water can be easily characterised and defined when individual surface tensions of the three materials are known.

Wetting of soft, deformable interfaces is also reasonably well understood. At these interfaces, competition between macroscopic, microscopic, and capillary forces takes place and the interactions become more interesting. Examples are elastocapillary deformation of the gel surface induced by surface forces [16–21], by swelling of the gel in the vicinity of the droplet [22], or in extreme cases even the effect of gravity of a droplet resting at the surface of a very soft gel, or at the interface of another liquid [23]. For the case of contact line deformation on soft substrate, literature describes this phenomenon as owing to geometric forces [23]: the liquid surface tension exerts pressure on the contact line, pulling it up as a ridge [16, 21, 24–27].

It is also known that polymer chains in soft polymer gels have the ability to adjust their conformation, and in certain cases adsorb to interfaces. Literature suggests that the material composition of a gel plays an important role in wetting dynamics [28]. In this article, the authors suggest that a polymer brush has the ability to stabilise out-of-equilibrium contact angles. However, most studies on soft wetting appear to neglect these molecular interactions. As a result, it is not well known how these interactions influence wetting. In this thesis, we study the effect of chemical composition of a hydrogel on its static and dynamic wetting properties, and, for hydrogels composed of

surface-active polymers, how adsorption of polymers at the interface affects wetting.

Hydrogels also offer the possibility to incorporate environment-sensitive building blocks within the gel, by co-polymerizing the gel with various organic and ionic groups. We investigate the possibility of making hydrogels pH- or ion-sensitive, and study their wetting properties. A potential application for switchable, environment-sensitive gels is in microfluidics, where these systems could be employed to allow for selective opening and closing of channels.

1.3 Directed colloidal assembly

As we mentioned before, the colloidal domain is the main arena for soft matter, but the previous examples have shown that other materials may exhibit soft interactions as well. The colloidal domain consists of particles with typical dimensions between 1 nm and 1 µm. A field that has received significant attention is the study of colloidal suspensions. These colloidal systems and their interactions can act as a macroscopic counterpart to atomic systems, where their larger size facilitates experimental observations. Because colloids can be prepared from a wide range of materials—organic, inorganic, pH-sensistive, charged, neutral—and the vast choice of liquids available for density or index matching of colloidal dispersions, colloidal systems have helped greatly in the understanding of crystal formation, phase change, and many more fundamental phenomena. Colloidal self-assembly, such as crystal formation, deserves a special mention [29]. During the formation of crystals with large bond strengths, such as is the case in ionic crystals, a small misalignment breaks crystal symmetry with no possibility for repair. However, in a colloidal crystal, the weak interactions allow for trial and error: thermal fluctuations are enough to overcome these issues, improve bond alignment, and facilitate crystal growth. This enables for growing macroscopic colloidal crystals with a much longer-range order than could be expected from the relatively small interaction energies.

It has been known for a long time that colloidal particles can adsorb to liquid-liquid interfaces [30, 31]. A practical application of this phenomenon is their use in particle-stabilised Pickering emulsions. The particle 'shell' around emulsion droplets stabilises against Ostwald ripening and coalescence. As a result of a reduction of the interfacial energy between the continuous phase and the emulsion droplets, due to the adsorbed particles reducing the interface area, particles are generally adsorbed very strongly to the interface, as opposed to detergent- or polymer-stabilised emulsions. A drawback of particle-stabilised emulsions is that solid particles generally do not adsorb spontaneously to interfaces. However, literature studies show that hybrid microgel core-shell particles, i.e. particles with a silica core and a hydrogel shell, are capable of spontaneous, polymer-like adsorption and strong, particle-like anchoring to liquid-liquid interfaces [32].

This spontaneous adsorption and strong anchoring opens a route to directing two-dimensional colloidal self-assembly at interfaces. Isotropic particles at isotropically curved interfaces generally arrange in a hexagonal lattice; the particle density at such an interface is governed by effects like steric and electrostatic repulsion. Also, if the combination of wetting angle and particle position at the interface leads to a deformation of said interface, this deformation is isotropic and any resultant additional particle interactions are also isotropic. It has been shown before that anisotropic particles exhibit anisotropic interactions [33–37]. Other, more recent, studies show that isotropic micrometer-sized colloids adsorbed to interfaces with anisotropic curvature can also lead to an anisotropic particle arrangement at the interface [38]. The origin of this effect is the deformation of the liquid interface by the particle. Because the contact angle is not constant around a spherical particle at an anisotropically curved interface, the liquid interface is lifted in one direction, and depressed in another. This generates an anisotropic excess surface energy, and as a result, particle interactions are now also anisotropic.

Based on the analysis of 'equilibrium' interfaces already populated with colloids at different packing densities, the authors propose a model that predicts power law scaling for the colloid interaction potential as a function of the deviatoric curvature $\mathcal{D} = 0.5|k_1 - k_2|$, where $k = 1/r$, and r the principal radius of curvature in a given direction [38]. Interfaces with a nonzero deviatoric curvature can be prepared in many shapes: a meniscus in a square container has a curvature gradient near its corners, dumbbell-shaped interfaces show a saddle point, and donut-shaped interfaces are curved in only one direction. Their model has not been validated with kinetic data. In this thesis, we attempt to validate the proposed model by following the formation of colloidal fractals at anisotropically curved interfaces in time, and to construct the complete particle interaction potential through analysis of particle approach trajectories. Probably the most facile way to generate interfaces with nonzero deviatoric curvature is by using a channel. For these interfaces, r_1 is limited by the channel width, and to a certain extent the choice of the liquid phases, while $r_2 = \infty$. In this case, the deviatoric curvature of the interface becomes a controlled parameter, which facilitates systematic research into the effects of interface curvature anisotropy on colloid interactions.

1.4 Outline of this thesis

This thesis consists of three parts under the umbrella term 'soft matter', focused on interactions at their interface with liquids or solids. We investigate the interplay between surface forces (adhesion, capillarity) and elastic deformations in soft solids, to understand how the competition between two opposing forces influences phenomena such as adhesion, wetting, and capillary colloidal assembly. A graphical outline is

provided in Figure 1.2.

In Part I we focus on gel-solid interfaces as we investigate the effectiveness of clustering on patterned adhesives. Chapter 2 describes our work on nature-inspired patterned adhesives. We start with a top-down laboratory approach, where we study the effect of clustering on patterned samples with fixed dimensions and feature size, and compare this to samples with homogeneously distributed features. We continue with an investigation of the effect of ordering on adhesive properties. For this, we look at samples with square or hexagonally ordered features, and compare this to samples with randomly positioned features. We conclude our study of patterned adhesives with computer simulations, in order to scan a wider range of possible experimental parameters.

In Part II we look at gel-liquid-liquid and gel-air-liquid interfaces to study the effects of hydrogel wetting and contact line pinning. Chapter 3 describes our work on the wetting properties and contact angles of air and oil at the hydrogel/air and hydrogel/water interface. We first look at the static wetting properties of these materials. The findings of these experiments trigger additional questions that we attempt to resolve with extensive dynamic contact angle experiments. Besides neutral hydrogels, we also investigate charged hydrogels, and show that we are able to synthesize pH-sensitive switchable hydrogels, with possible applications in microfluidics.

Part III focuses on the behaviour of microgel and solid colloid interactions at liquid-liquid interfaces with anisotropic curvature. We allow these colloids to adsorb to and self-assemble at anisotropically curved oil/water interfaces. In Chapter 4, we look at the behaviour of microgel core-shell colloids. These particles have been known to adsorb spontaneously and strongly to oil/water interfaces. For this system we show that the particle interaction potential is strongly dependent on the deviatoric curvature of the interface. Over time, these particles adsorb into stable macroscopic anisotropic superstructures with long-range order.

As we find that our experiments do not satisfactorily match computational predictions, we move from the relatively complex microgel particles to a relatively more straightforward model system using silica particles. Our research on these particles is described in Chapter 5. With some experimental modifications, we show that this system is also capable of self-assembling anisotropic colloidal structures at oil/water interfaces. However, we find much weaker particle interactions here. In contrast to the previously described stable macrostructures obtained with microgel particles, the silica system shows a much weaker particle interaction potential, resulting in anisotropic structures consisting of only a few particles at a time being found. We attribute this to a combination of different factors, and conclude that further simplification of the experimental system is required to obtain deeper fundamental insights.

We end this thesis with a general discussion in Chapter 6 and a summary in Chapter 6.3.

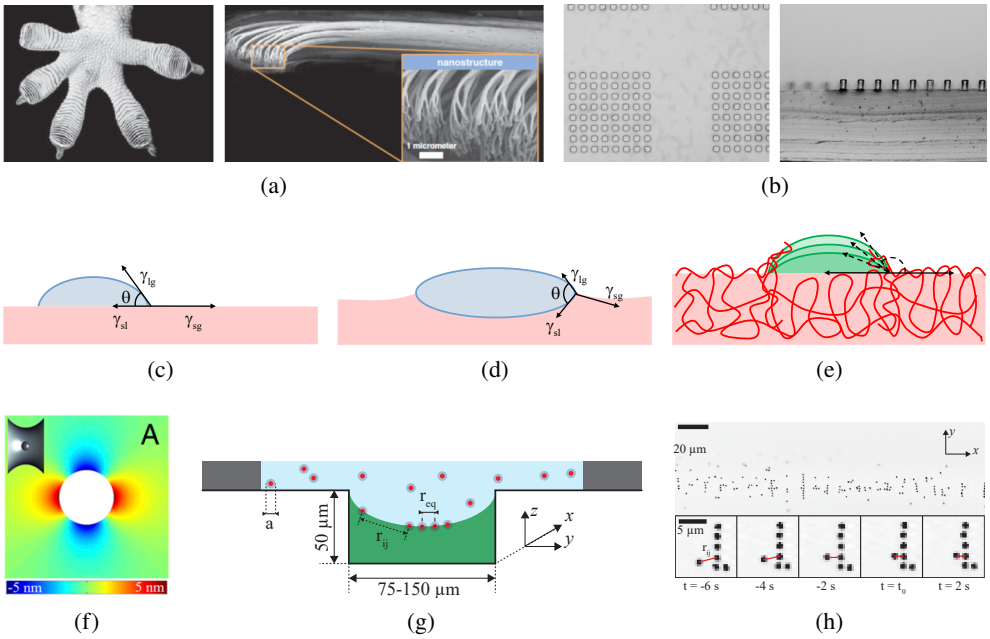

Figure 1.2 – Graphical outline of this thesis. Part I: (a) Nature's top performer on the adhesive spectrum, the gecko, employs a wide variety of hierarchical structures and patterning, from the macroscopic toes to the microscopic setae, all working in unison to yield a highly compliant, self-cleaning adhesive contact pad; reproduced from [14]. (b) The effects of clustering and patterning have been neglected in studies so far. We investigate these effects with patterned silicone adhesives in this thesis. Images show a top and side microscopic image of a silicone adhesive with a clustered pattern.
Part II: (c) Wetting of hard surfaces is easily understood and reduced to Young's law, which yields all relevant angles once individual surface tensions are known. (d) Wetting of soft surfaces can alter this picture, as liquids are able to deform the soft surface through capillary interactions. This is also relatively well understood, but research focuses mostly on macroscopic effects. (e) In this thesis, we study the wetting properties of soft hydrogels, and investigate the effects of sample composition and polymer adsorption at the interface on the dynamic contact angle.
Part III: (f) Isotropic particles generally show isotropic capillary interactions, unless placed on interfaces with anisotropic curvature. In order to satisfy Young's law's requirement of a constant contact angle at equilibrium, these particles have to deform the interface. This leads to anisotropic capillary interactions; image reproduced from [38]. (g) and (h) In this thesis we study the strength and range of these interactions for two different types of colloidal particles at semi-cylindrical oil-water interfaces.

References

[1] Arthur L. Fry. Repositionable pressure-sensitive adhesive sheet material, **1993**.

[2] S. Akerboom, J. Appel, D. Labonte, W. Federle, J. Sprakel, and M. Kamperman. Enhanced adhesion of bioinspired nanopatterned elastomers via colloidal surface assembly. *Journal of the Royal Society, Interface / the Royal Society*, **2015**. *12*, 20141061. doi:10.1098/rsif.2014.1061.

[3] M. D. Bartlett, A. B. Croll, and A. J. Crosby. Designing bio-inspired adhesives for shear loading: From simple structures to complex patterns. *Advanced Functional Materials*, **2012**. *22*, 4985–4992. doi:10.1002/adfm.201201344.

[4] C. Greiner, A. Del Campo, and E. Arzt. Adhesion of bioinspired micropatterned surfaces: Effects of pillar radius, aspect ratio, and preload. *Langmuir*, **2007**. *23*, 3495–3502. doi:10.1021/la0633987.

[5] C. Heinzmann, C. Weder, and L. M. de Espinosa. Supramolecular polymer adhesives: advanced materials inspired by nature. *Chem. Soc. Rev.*, **2016**. *45*, 342–358. doi:10.1039/C5CS00477B.

[6] S. Hu and Z. Xia. Rational design and nanofabrication of gecko-inspired fibrillar adhesives. *Small*, **2012**. *8*, 2464–2468. doi:10.1002/smll.201200413.

[7] A. Jagota and C.-Y. Hui. Adhesion, friction, and compliance of bio-mimetic and bio-inspired structured interfaces. *Materials Science and Engineering: R: Reports*, **2011**. *72*, 253–292. doi:10.1016/j.mser.2011.08.001.

[8] M. Kamperman, E. Kroner, A. Del Campo, R. M. McMeeking, and E. Arzt. Functional adhesive surfaces with "Gecko" effect: The concept of contact splitting. *Advanced Engineering Materials*, **2010**. *12*, 335–348. doi:10.1002/adem.201000104.

[9] M. K. Kwak, C. Pang, H. E. Jeong et al. Towards the next level of bioinspired dry adhesives: New designs and applications. *Advanced Functional Materials*, **2011**. *21*, 3606–3616. doi:10.1002/adfm.201100982.

[10] M. Röhrig, M. Thiel, M. Worgull, and H. Hölscher. 3D Direct laser writing of nano- and microstructured hierarchical gecko-mimicking surfaces. *Small*, **2012**. *8*, 3009–3015. doi:10.1002/smll.201200308.

[11] J. Yang, J. Keijsers, M. van Heek, A. Stuiver, M. A. Cohen Stuart, and M. Kamperman. The effect of molecular composition and crosslinking on adhesion of a bio-inspired adhesive. *Polymer Chemistry*, **2015**. *6*, 3121–3130.

[12] E. Arzt, S. Gorb, and R. Spolenak. From micro to nano contacts in biological attachment devices. *Proceedings of the National Academy of Sciences*, **2003**. *100*, 10603–10606. doi:10.1073/pnas.1534701100.

[13] D. Labonte, C. J. Clemente, A. Dittrich et al. Extreme positive allometry of animal adhesive pads and the size limits of adhesion-based climbing. *Proceedings of the National Academy of Sciences*, **2016**. *113*, 1297–1302. doi:10.1073/pnas.1519459113.

[14] K. Autumn. Gecko adhesion: Structure, function, and applications. *MRS Bulletin*, **2007**. *32*, 473–478. doi:10.1557/mrs2007.80.

[15] H. E. Bakker, S. B. Lindström, and J. Sprakel. Geometry- and rate-dependent adhesive failure of micropatterned surfaces. *Journal of Physics: Condensed Matter*, **2012**. *24*, 065103. doi:10.1088/0953-8984/24/6/065103.

[16] C. Extrand and Y. Kumagai. Contact Angles and Hysteresis on Soft Surfaces. *Journal of colloid and interface science*, **1996**. *184*, 191–200. doi:10.1006/jcis.1996.0611.

[17] T. Kajiya, A. Daerr, T. Narita, L. Royon, F. Lequeux, and L. Limat. Dynamics of the contact line in wetting and diffusing processes of water droplets on hydrogel (PAMPS–PAAM) substrates. *Soft Matter*, **2011**. *7*, 11425. doi:10.1039/c1sm05944k.

[18] A. Leh, H. E. N'guessan, J. Fan et al. On the role of the three-phase contact line in surface deformation. *Langmuir*, **2012**. *28*, 5795–5801. doi:10.1021/la3000153.

[19] S. Mangili, C. Antonini, M. Marengo, and A. Amirfazli. Understanding the drop impact phenomenon on soft PDMS substrates. *Soft Matter*, **2012**. *8*, 10045. doi:10.1039/c2sm26049b.

[20] G. Pu and S. J. Severtson. Dependence of wetting behavior on the thickness of highly viscoelastic films. *Journal of Physical Chemistry C*, **2011**. *115*, 18729–18735. doi:10.1021/jp205662v.

[21] R. W. Style, R. Boltyanskiy, Y. Che, J. S. Wettlaufer, L. A. Wilen, and E. R. Dufresne. Universal deformation of soft substrates near a contact line and the direct measurement of solid surface stresses. *Physical Review Letters*, **2013**. *110*, 66103. doi:10.1103/PhysRevLett.110.066103.

[22] F. Boulogne, F. Ingremeau, L. Limat, and H. A. Stone. Tuning the Receding Contact Angle on Hydrogels by Addition of Particles. *Langmuir*, **2016**. *32*, 5573–5579. doi:10.1021/acs.langmuir.6b01209.

[23] A. Marchand. *Mouillage statique et dynamique: Influences géométriques aux échelles moléculaires*. Ph.D. thesis, UNIVERSITÉ PARIS VII – DENIS DIDEROT, **2011**.

[24] J. Snoeijer. Analogies between Elastic and Capillary Interfaces. *Physical Review Fluids*, **2016**. *1*, 060506. doi:10.1103/PhysRevFluids.1.060506.

[25] A. Pandey, S. Karpitschka, L. A. Lubbers et al. Dynamical theory of the inverted cheerios effect. *Soft Matter*, **2017**. *13*, 6000–6010. doi:10.1039/c7sm00690j.

[26] S. Karpitschka, S. Das, M. van Gorcum, H. Perrin, B. Andreotti, and J. H. Snoeijer. Droplets move over viscoelastic substrates by surfing a ridge. *Nature Communications*, **2015**. *6*. doi:10.1038/ncomms8891.

[27] M. van Gorcum, B. Andreotti, J. H. Snoeijer, and S. Karpitschka. Dynamic Solid Surface Tension Causes Droplet Pinning and Depinning. *Physical Review Letters*, **2018**. *121*, 208003. doi:10.1103/PhysRevLett.121.208003.

[28] M. A. Cohen Stuart, W. M. de Vos, and F. A. M. Leermakers. Why surfaces modified by flexible polymers often have a finite contact angle for good solvents. *Langmuir*, **2006**. *22*, 1722–1728. doi:10.1021/la052720v.

[29] J. Zhang, Y. Li, X. Zhang, and B. Yang. Colloidal self-assembly meets nanofabrication: From two-dimensional colloidal crystals to nanostructure arrays. *Advanced Materials*, **2010**. *22*, 4249–4269. doi:10.1002/adma.201000755.

[30] M. P. Boneschanscher, W. H. Evers, J. J. Geuchies et al. Long-range orientation and atomic attachment of nanocrystals in 2D honeycomb superlattices. *Science (New York, N.Y.)*, **2014**. *344*, 1377–80. doi:10.1126/science.1252642.

[31] A. D. Dinsmore, M. F. Hsu, M. G. Nikolaides, M. Marquez, A. R. Bausch, and D. A. Weitz. Colloidosomes: selectively permeable capsules composed of colloidal particles. *Science (New York, N.Y.)*, **2002**. *298*, 1006–1009. doi:10.1126/science.1074868.

[32] H. Monteillet, M. Workamp, J. Appel, J. M. Kleijn, F. A. M. Leermakers, and J. Sprakel. Ultrastrong Anchoring Yet Barrier-Free Adsorption of Composite Microgels at Liquid Interfaces. *Advanced Materials Interfaces*, **2014**. *1*. doi:10.1002/admi.201300121.

[33] E. P. Lewandowski, M. Cavallaro, L. Botto, J. C. Bernate, V. Garbin, and K. J. Stebe. Orientation and self-assembly of cylindrical particles by anisotropic capillary interactions. *Langmuir*, **2010**. *26*, 15142–15154. doi:10.1021/la1012632.

[34] M. Cavallaro, L. Botto, E. P. Lewandowski, M. Wang, and K. J. Stebe. Curvature-driven capillary migration and assembly of rod-like particles. *Proceedings of the National Academy of Sciences*, **2011**. *108*, 20923–20928. doi:10.1073/pnas.1116344108.

[35] L. Botto, L. Yao, R. L. Leheny, and K. J. Stebe. Capillary bond between rod-like particles and the micromechanics of particle-laden interfaces. *Soft Matter*, **2012**. *8*, 4971. doi:10.1039/c2sm25211b.

[36] S. Dasgupta, M. Katava, M. Faraj, T. Auth, and G. Gompper. Capillary assembly of microscale ellipsoidal, cuboidal, and spherical particles at interfaces. *Langmuir : the ACS journal of surfaces and colloids*, **2014**. *30*, 11873–82. doi:10.1021/la502627h.

[37] G. B. Davies, T. Krüger, P. V. Coveney, J. Harting, and F. Bresme. Assembling ellipsoidal particles at fluid interfaces using switchable dipolar capillary interactions. *Advanced Materials*, **2014**. *26*, 6715–9. doi:10.1002/adma.201402419.

[38] D. Ershov, J. Sprakel, J. Appel, M. A. Cohen Stuart, and J. van der Gucht. Capillarity-induced ordering of spherical colloids on an interface with anisotropic curvature. *Proceedings of the National Academy of Sciences of the United States of America*, **2013**. *110*, 9220–4. doi:10.1073/pnas.1222196110.

Part I

Adhesion

Chapter 2

Patterned adhesives as a structural gecko mimic

Abstract

We attempt to improve existing adhesives by patterning materials in order to serve as a gecko mimic. Two practical attempts are described here: clustering, as a hierarchy mimic, and ordering, as a means of directing crack front propagation. The results of our experiments mostly suggest that the peak force per unit area $F_{\max}/A \approx$ const, hence structured adhesives at the scale investigated here do not improve adhesive properties. We then perform computer simulations to address a larger parameter space. Depending on simulation parameters we are able to distinguish two different pillar detachment regimes; a stochastic regime, where individual pillars detach in a random sequence, and a deterministic regime similar to the ones found in our laboratory experiments, where detachment occurs by crack propagation. Further simulations are performed in the deterministic regime. We find that the peak force, normalised by pillar count, at the onset of adhesive failure $F_{\max}/N$ scales as $F_{\max}/N \approx$ const at low separation velocities, and develops as $F_{\max}/N \sim \log v$ at higher separation velocities. We find a positive effect of clustering, with a reported increase in $F_{\max}/N \approx 4$–$12\,\%$ for square clustered samples, compared to a homogeneous square array of pillars. Patterns with random pillar placement perform on par with samples with square pillar arrangement.

2.1 Introduction

Adhesives are widely used in every aspect of daily life. They range from the simple starch-based glue used to hold pieces of a child's artwork together, to multi-component epoxy glues for bonding a wide variety of materials in construction applications, to high-tech speciality glues that keep high-performance devices together. A very early example is the use of Neanderthal-manufactured pitch to join blade and haft for a tool [1]. In industrial applications, adhesives can be preferred over or used in conjunction with mechanical fastening. Various advantages of adhesives include them being (nearly) invisible in a finished assembly, their ability to bond irregularly shaped surfaces together [2], and their low weight [3] and cost [4]. Another advantage is their ability to bond different materials together, such as metals, ceramics, polymers, wood and other materials [4]. Adhesion also plays an important role in various high-tech applications. Examples include the application of hybrid nanocomposite fillers in polymeric elastomers to enhance their adhesive properties [5], adhesives in aerospace [6, 7] or in applications with extreme temperature requirements [2].

Adhesives are often balanced on the edge between being strong enough to hold materials together, and not so strong that eventual separation or removal of the adhesive results in destruction of the materials it held together. In certain scenarios this behaviour is appropriate, for instance in construction applications. However, destructive separation is undesirable in various high-tech applications, such as in medical applications or soft robotics, where reversible glue applications are a key benefit.

Most adhesives are intended for single use only. Depending on their application, these single-use adhesives can hold relatively large loads. However, they are often limited in the range of operation, both with regards to environmental conditions as well as the materials that can be bound together, and they usually require destructive mechanical force to allow separation of parts. Furthermore, many adhesives require a very clean, grease- and water-free porous surface to maximize adhesive strength.

Reusable adhesives are occasionally used. Post-it notes are the prime example [8]. However, the adhesive strength of these materials is severely limited compared to that of even the most basic single-use adhesive. Fouling of the sticky patch is the main reason for the limited number of times a reusable adhesive can be applied. As a result of this fouling, the adhesive strength gradually decreases until the sticky object eventually completely fails to adhere.

In order to arrive at a superior reusable adhesive, we have to combine advantages of mechanical bonding, single-use glue and reusable adhesives. The adhesive should be able to sustain a considerable load for a prolonged duration, while allowing for facile removal when desired, without a need for mechanical separation and the associated damage. After this separation, its adhesive strength should remain standing. For this, many researchers have looked for inspiration in nature. One approach is inspired

by aquatic organisms, such as mussels, and leads to advances in supramolecular adhesives [9, 10]. Another significant research effort focuses on patterned adhesives, inspired by animals such as geckoes and spiders [11–23].

Various animals are capable of walking and holding on to vertical, or even inverted, surfaces. A prime example is the gecko, the animal with the largest mass to foot surface area ratio still capable of suspending its own weight [24, 25]. It is also known that a gecko does not have to apply a continuous force in order to remain attached, as a dead gecko has the same adhesive performance as a live one [26]. In itself, this is quite an achievement. Generally speaking, a force larger than the maximum adhesive force of the material is required to detach an adhesive. For a gecko walking around freely, repeatedly applying this removal force could become prohibitively energy-intensive, or would require excessively large muscular structures that add weight without improving adhesion. However, it is found that the gecko can detach at will through the application of a relatively small, directional force. This force is known as hyperextension, a curling of the toes similar to tape peeling [27, 28], essentially making gecko adhesion completely reversible. The gecko achieves this by localising stress forces to the edge of the foot, thereby nucleating adhesive failure. Nature achieves this through the use of hierarchical structures [14, 17]. If we descend the gecko hierarchy, we find the animal itself as the macrosctructure. As a mesostructure we consider the feet that branch in toes, each of which branches once more in ridges, somewhat comparable to fingerprints. The microstructure of these ridges reveals clusters of fibrils, similar in size to human hair, called setae. Each seta branches again at the end in keratin fibrils, that end in a spatula shape [29]. This hierarchy is shown in the images in Figure 2.1. It is calculated that a shear force of 1300 N is needed to detach a gecko. While the origins of the exceptional adhesive mechanics have been debated, it is now clear that they are entirely due to attractive van der Waals forces and that capillary interactions play no substantial role [29]. The authors also note that as a result of their small size, these keratin fibrils have a shear modulus in the 0.1 MPa order of magnitude. This is several orders of magnitude lower than that of bulk keratin, which has a shear modulus in the 1 GPa range. As a the Dahlquist criterion for tackiness has an upper limit of 0.1–0.3 MPa, these fibrils fall just inside the tacky range [29].

An adhesive starts to give in when a certain stress threshold is exceeded. This stress buildup usually starts at the edge or in a corner of a sample, as applied stresses concentrate there due to the mechanical geometry. This leads to the nucleation of an adhesive crack, upon which the adhesive lets go of the surface. The applied force then concentrates on the new edge upon which this also fails. This triggers a cascade that ultimately leads to failure of the adhesive contact as a whole.

Despite a wealth of research on micropatterned adhesives inspired by natural systems, the effects of the geometry such as pillar clustering or order versus disorder,

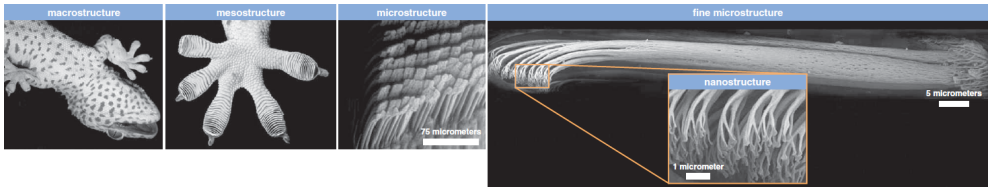

Figure 2.1 – The structural hierarchy of the gecko adhesive system. Reproduced from [29]. Scale bares indicate 75 µm in the microstructure image, 5 µm in the fine microstructure image, and 1 µm in the nanostructure image.

remain partially unclear. Here we develop an experimental approach to study these effects. We investigate hierarchically patterned structures as a means to improve adhesive strength. Many researchers investigate patterned adhesion in an attempt to improve adhesive properties. However, measurements on patterned adhesives produce a variety of artefacts due to various experimental challenges, which may lead to misinterpretation of results. In this work, we strive to find a reproducible method to prepare three-dimensional patterned surfaces on a larger scale, in order to investigate the speculated significance of pattern on adhesive performance [12]. Various patterning methods exist, such as colloidal surface assembly [11], electron beam templating, or soft lithography [30]. We use soft photolithograpy as a templating technique to create silicone rubber adhesive structures. To test adhesive properties, a number of test layouts exist. In shear tests, adhesive performance is measured as a function of an applied shear force to a sample. In peel tests or tape peel tests [9, 31], the sample is attached like regular adhesive tape to a substrate or to itself, and pulled off under an angle. A fourth common test method is a pull test, in which the sample is removed from the substrate it is attached to in a perpendicular motion [9, 32]. We exclusively use the pull test in the experiments described in this work.

After careful experimentation, we find that patterning has very little influence on the adhesive properties of a structure. We conclude that any observed increase in adhesion between patterned and non-patterned adhesives is likely a result of improved compliance between substrate and adhesive due to contact splitting by the micropillars themselves, independent of the used pattern. In our studies we also observe that adhesive failure is postponed until the first pillars fail, after which catastrophic failure is unavoidable. These first pillars are almost always edge pillars, indicating that focus should be on improving adhesive edges, not the adhesive as a whole.

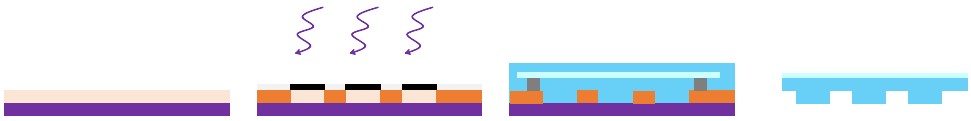

Figure 2.2 – The lithography process illustrated: (a) A layer of photoresist (orange) is coated onto a wafer (purple) and given a soft bake to evaporate solvent. (b) A masked exposure selectively activates part of the photoresist, which is crosslinked in a subsequent hard bake step (dark orange). (c) After etching of the non-crosslinked photoresist, we fill the sample with a liquid PDMS premix. A spacer (dark gray) and a fluorinated glass slide are used to ensure a constant sample thickness. (d) After the PDMS is baked, it is removed from the wafer, bonded to another glass slide, and ready for adhesive testing.

2.2 Materials and methods

2.2.1 Soft lithography

We used silicon wafers as the lithographic substrate. Wafers were obtained from Wafernet, Inc. (ø150 mm) or Siltronic AG (ø75 mm). The large wafers were first cut into smaller chips and subsequently cleaned in a piranha solution, rinsed with distilled water, and dried prior to use. Cleaning was necessary to remove silicon splinters and (organic) residue. Siltronic wafers were used as received, therefore, the cleaning step was omitted.

We used a Laurell WS-650MZ spincoater to coat substrates. SU-82 5 (Microchem) was used as the negative photoresist. To improve wetting, we first coated a thin layer of photoresist by introducing SU-8 to the substrate while spinning at high speed. The spincoater was then stopped to add additional SU-8. Approximately 0.2 mL cm^{-2} SU-8 was used for the final coating. If necessary, air bubbles were removed from the SU-8 droplet prior to engaging the spin cycle. The photoresist was spun to its final thickness of 30–40 µm with a two-step spin cycle. Parameters are given in Table 2.1.

After spincoating, a soft-bake step was applied to remove most solvent in the photoresist prior to UV patterning. Wafers were placed on a pre-heated hotplate at 65 °C. Wafers were covered by a petri dish for the first 15 min of this bake step. After a total baking time of 45 min, the hotplate was switched off and wafers were either left on the hotplate, or removed immediately from the hotplate to cool down to room temperature.

Photomasks were designed in AutoCAD and ordered as high-resolution emulsion

on film negatives from CAD/Art[1] or JD Photo-Tools[2]. The print resolution was 10 µm. After sufficient cooling, a masked exposure of the photoresist was done with an EXFO OmniCure S1500 UV lamp, with a 200 W mercury lamp equipped with a 365 nm line filter. The lamp was set up to project a homogeneous 13 cm diameter light spot on the workbench. Samples were exposed for 30 s. Immediately after exposure, wafers were placed on a hotplate pre-heated to 65 °C. After 1 min, the temperature was increased to 95 °C at a rate of 30 °C min^{-1}. After a total baking time of 6 min, the wafer was removed from the hotplate and placed in a petri dish in a drawer, to prevent additional exposure. Exposed wafers were allowed to rest overnight prior to development.

Development was done in a bath of propylene glycol monoethyl ether acetate (PGMEA, Sigma Aldrich) for 6 min, with intermittent stirring or shaking every 30 s. After development, wafers were rinsed with additional PGMEA or acetone, followed by a rinse with isopropyl alcohol. Wafers were then dried under a stream of nitrogen, directed at the center of the exposed area to expel any remaining solvent. This yields master templates from which adhesive structures could be replica moulded. The quality of wafers was assessed with an optical microscope at a magnification of 10–50 ×. A schematic overview of the entire lithographic process is shown in Figure 2.2.

2.2.2 Silicone rubber moulding

Suitable wafers were used to prepare patterned adhesives. First, the master was glued in a 15 cm diameter petri dish. To promote the ease of removal of the replica moulded structure from the template, the master was first modified by fluorinating it. This was achieved by placing the master in a vacuum desiccator in the presence of a small quantity of *N*-methyl-*N*-(trimethylsilyl)trifluoroacetamide (MSTFA, Sigma Aldrich). The desiccator was then evacuated, sealed, and left overnight. This procedure was also used to coat the microscope slides that were used as spacers in the next step.

A silicone rubber premix was prepared by thoroughly mixing an elastomer base and curing agent (PDMS, Dow Corning Sylgard 184) in a 10:1 ratio by mass. This

[1] www.outputcity.com
[2] http://www.jdphoto.co.uk/

Table 2.1 – Final photoresist coating spin cycle parameters

	Speed (rpm)	Acceleration (rpm/s)	Time at speed (s)
SU-8 deposition	2000		
Step 1	500	100	10
Step 2	1250	300	30

was done in ca. 25–40 g quantities in 50 mL Falcon tubes in a tumbler for 15–30 min. To prevent air bubble formation in the final adhesive samples, the tubes were first centrifuged, and subsequently evacuated in a vacuum desiccator to remove the majority of air bubbles present in the mixture. The degassed silicone mixture was then poured in the petri dishes with the fluorinated wafers. Additionally, the petri dishes with silicone rubber premix were then thoroughly degassed in the vacuum desiccator for at least 15 min, or until no more air bubbles appeared.

The thickness of an adhesive sample is known to affect its compliance and thereby its adhesive performance. To ensure a constant sample thickness, 1.5 mm capillary glass filaments or tubes were placed alongside the etched pattern, to act as spacers. A fluorinated glass microscope slide was then carefully lowered into the elastomer on top of these spacers, and gently pressed down, avoiding the entrapment of new air bubbles. The petri dishes were then placed in a laboratory oven preheated to 65 °C and left overnight. Samples were then removed from the oven and allowed to cool down to room temperature.

After cooling down, the glass slide was removed from the top of the cured silicone rubber. The patterned patch of silicone rubber was subsequently removed from the mould by cutting along the edges, and lifting the substrate very slowly, in order not to damage the features. Upon successful removal, adhesive samples were assessed again with an optical microscope. To achieve a stable, non-compliant anchoring point, samples were then plasma-bonded with their non-patterned back to an untreated glass microscope slide. This was done by placing the adhesive sample and an uncoated microscope slide side-by-side in a Harric PDC-32G plasma chamber. During this process, the patterned side of the silicone samples was covered with a piece of Scotch tape to prevent activation. After evacuation of the chamber, the plasma was briefly turned on at high power, until a purple glow was emitted. The top, non-patterned side of the silicone sample and the glass slide were then brought together to form the bond. After this procedure, samples were left for at least 24 h prior to adhesive testing.

2.2.3 Patterns

Two distinctive sets of patterned surfaces were designed. First, we designed a set of clustered patterns. The size of this arrangement was 240×240 square pillars of $25 \times 25\,\mu m^2$ each, with a center-to-center pillar spacing $d_p = 75\,\mu m$. This resulted in a square sample with side $L = 18$ mm. The pillar density, defined as the ratio between the total area of the sample and the area covered by pillars, was approximately 10 %. Within a cluster, the pillar spacing was reduced to $d_c = 20\,\mu m$. Clusters were then spaced out to cover the same total sample area. A schematic drawing of this arrangement, together with some photomasks and some actual results are shown in Figure 2.3.

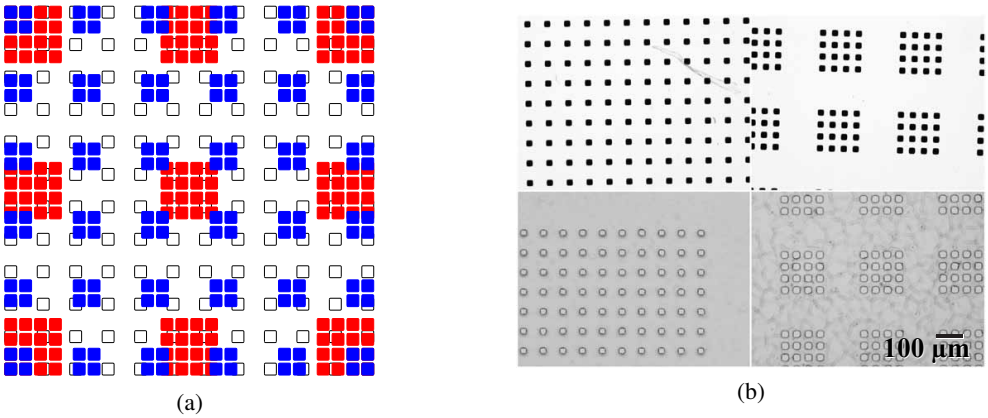

(a) (b)

Figure 2.3 – Design of clustered adhesive samples. (a) Overlay of a homogenous square distribution, a 2x2 and a 4x4 cluster. The overall sample dimension L is fixed by determining a feature size and separation. A significantly smaller pillar spacing d_c is selected to create clusters. (b) Example of photomasks (top) and their corresponding lithographic prints (bottom), showing a homogeneous and a 4×4 clustered sample.

The second set of patterned samples was designed to investigate the effect of pillar order, by arranging them in different patterns. Here, we used circular pillars, with $r = 12.5\,\mu m$. We designed patterns with square or hexagonally ordered pillar arrays. We also designed samples with a built-in grain boundary, obtained by rotating the pattern 45° (square) or 90° (hexagonal) in the middle of the sample. Lastly, we designed samples with random pillar placement. Samples were designed with either 67×67 or 100×100 pillars in a square with side $L = 5\,mm$, to yield a pillar density of either 10 % or 20 %. In order to investigate a potential edge effect on the sample as a whole, we also designed masks for the square, hexagonal and randomly patterned samples as the inscribed circle of this square. Examples of these patterns are shown in Figure 2.4.

2.2.4 Adhesive testing

Two adhesion test setups were used: a rheometer (TA Instruments DHR-3), operated in vertical traction mode, and a custom-made total internal reflection microscope (TIRM), equipped with a motorized stage and force sensor. For the rheometer setup, we placed a large glass microscope slide on the rheometer base to test the adhesive samples against. The slide was fixed to the rheometer base with paraffin wax. For the TIRM setup, we directly used the surface of the optical prism as the adhesive substrate. The glass surfaces were pre-stamped with PDMS to ensure constant surface properties

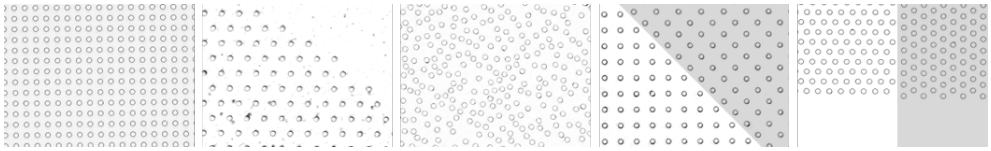

Figure 2.4 – Patterned samples with circular features, showing examples of three regular samples and two grain boundary samples. From left to right: a 20 % square pattern, a 10 % hexagonal pattern in a circular shape, a 20 % random pattern. Then a 10 % square with a 45° grain boundary, and a 20 % hexagonal pattern with a 90° grain boundary. The two sides of the grain boundary are shaded differently.

over the course of experiments. Surfaces were cleaned with a piece of Scotch tape prior to experiments in order to remove dust particles.

In adhesion experiments, proper alignment between sample and substrate is of key importance. A small misalignment already leads to a large stress gradient on the sample in the best case, or in the worst case it leads to the sample only being partially attached. To ensure optimal alignment between the adhesive sample and the surface, the sample was placed with its feature side on the surface. The rheometer or TIRM probe was then lowered to hover just above the sample, carefully avoiding touching the sample in order to avoid the application of pressure before the adhesion experiment. The glass backing layer was then glued to the probe with Norland optical adhesive.

Adhesion tests were carried out as following: after bonding the sample to the probe, the sample was lifted from the surface, after which the force sensor was set to zero. Samples were then brought into contact with the surface. A constant preload of 0.5 N was applied for 60 s. The sample was then retracted at a constant velocity of $1\,\mu m\,s^{-1}$. This procedure was repeated at least five times for each sample. The data acquisition rate is set to $1\,s^{-1}$ for the rheometer, or $10\,s^{-1}$ for the TIRM setup.

2.3 Results and discussion

2.3.1 Sample microfabrication

For the experiments in this chapter, the lithography step is one of the most significant determiners of sample quality, and a significant amount of time was spent on developing a reproducible, high-quality lithography process.

The quality of a lithography print is (subjectively) assessed on three categories: feature sharpness or clarity, photoresist surface cracks, and residual photoresist in nonexposed areas. Naturally, high feature sharpness is desired, as this gives the

closest approximation of the intended feature shape. Mild cracking in the photoresist surface is generally not a problem and simply arises from the various stresses the material goes through as it is heated, cooled, exposed to UV light, and etched with solvent. However, severe cracking is an indicator of a poorly optimized process. This can also lead to delamination of the photoresist from the substrate. Residual photoresist in wells is particularly undesirable, as the surface at the bottom of the well is what ultimately determines the surface quality of the final adhesive sample. Such a residue leads to increased surface roughness and possibly unevenness of features in different parts of the sample, and therefore decreased adhesive properties.

The generic protocol is described in Section 2.2.1. The protocol above generally leads to reproducible, good quality results, but it appears that different environmental conditions have a significant effect on lithography quality. Sample quality appears to decrease somewhat with increasing room temperatures. Humidity seems to have a more significant effect, with a significant loss of sample quality at a relative humidity of about 75 %. Samples prepared under more humid conditions show an increased tendency towards adhesive failure between the photoresist and substrate, as well as reduced sharpness and increased surface residue accumulation in wells. Significant improvements in reproducibility are expected when the lithography process is moved to a climate-controlled room.

Some lithography results are shown in Figure 2.3. Here we observe that the square pillar design is not optimal, as pillars have rounded corners. With a 20 µm feature size and a 10 µm print resolution, corner sharpness, or the lack thereof, can significantly affect the outcome of the final sample. We can already see this if we look at a magnification of the photomasks, as shown in Figure 2.3b. Edge sharpness is further reduced in the various steps of the lithography process; be it as a result from stray UV light around the edges of the mask, diffusion of activated radicals into non-activated parts of the photoresist, or as a result of the etching steps. The image in Figure 2.3b shows one of the best results obtained with this lithography process, and although features are relatively clean and sharp, they are distinctively rounded squares, and not square features. This design flaw was addressed in the second set of (patterned) surfaces, where the features were designed as circles instead.

By cutting a sample along the features, and placing a slice sideways under an optical microscope, we can determine the pillar aspect ratio l/w. We also measure the angle between the horizontal and vertical part to gain some addition insight in the quality of the lithography process. We expect our features to be present at an angle of 90°; a deviation of this suggests a serious problem with the process.

We find an average aspect ratio of 1.67 ± 0.23, at an average angle of $(90.0 \pm 1.7)°$ for both clustered samples and patterned samples (Figure 2.5). We observe no significant differences for the average angle nor aspect ratio between any of these samples. These results indicate that soft photolithography is a suitable technique to produce

(a)

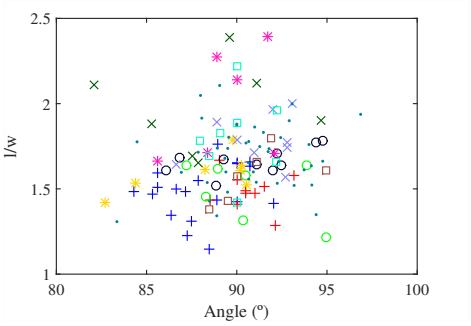

(b)

Figure 2.5 – Determination of the aspect ratio of PDMS structures. (a) A PDMS slice viewed sideways, allowing to determine the pillar aspect ratio. (b) A plot of the observed aspect ratio l/w as a function of orientation. Different colours and symbols indicate different samples.

patterned samples with a high degree of reproducibility.

2.3.2 Adhesion testing: Rheometer

Protocol optimisation

For initial adhesion tests we use a TA Instruments DHR-3 rheometer. We use the setup with a glass slide mounted to the rheometer base to act as a surface to test adhesive samples against, and we glue the glass-backed PDMS adhesive samples to a flat rheometer probe. The rheometer is equipped with magnetic thrust bearings and is capable of high-precision normal force measurements. While rheometer engineering is optimized for torque measurements, the sensitive normal force sensor allows adhesion measurements to be performed with reasonable accuracy.

Typical adhesion curves are shown in Figure 2.6. Starting at a positive magnitude as a result of the applied preload, the adhesion curve linearly decreases to a given minimum. At this point, the adhesive force of the sample has reached its maximum, and adhesive failure starts to take place. The force then rapidly decreases to zero as the sample is released.

As described in the Materials and Methods section, we use a repeated preload and retract cycle to measure adhesive force. During these measurements, we find that the probe tends to rotate while the sample is released from the surface. This leads to misalignment, and a significant loss of adhesive force in subsequent measurements, or to a shift in the position of the adhesive maximum (Figure 2.6a). We address this issue

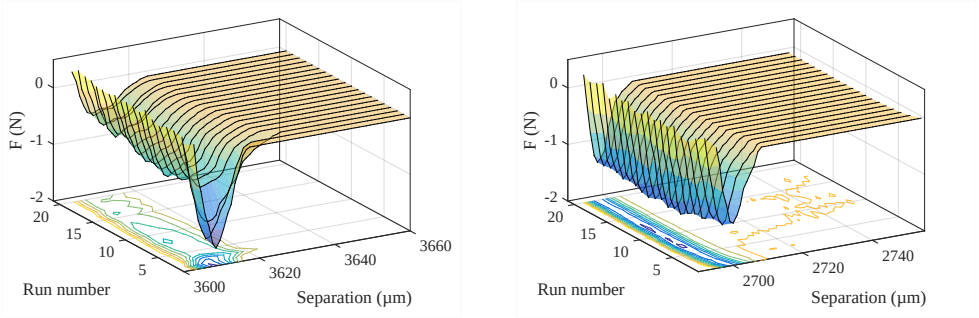

(a) (b)

Figure 2.6 – Adhesion measurements and protocol improvement.(a) Free rotation of the rheometer probe can lead to misalignment, which results in a significant decrease in adhesive force, an potentially a shift in peak position, as appears from included contour plot. (b) With the rotor locked in place, both peak height and position are much more reproducible over the course of several runs, as indicated by the constant 'depth' of the waterfall plot, as well as the sharp lines in the contour plot.

by locking the probe in place by taping its position to the rheometer head. This leads to a significant improvement of experimental reproducibility (Figure 2.6b), although we still observe a small decrease in adhesive force between the first and subsequent runs. However, this is negligible compared to the previous effect.

Patterned adhesive with a clustered design

We first look at the adhesive properties of samples with a clustered pattern. In this experiment we compare the adhesive properties of a sample patterned with a homogeneous distribution of pillars to samples in which the pillars are clustered together. Examples of such patterns are shown in Figure 2.3b. To measure adhesive strength, we look at the peak force. We divide the results by the contact area of the sample. This calculation lets us arrive at an adhesive stress $P = F/A$. This facilitates comparison between samples of different size. For rheometer experiments, we have to calculate the contact area from the design specifications, as it is not feasible to obtain a representative 'actual' contact area from microscope images.

We do a large number of measurements with clustered samples. Results are shown in Figure 2.7a. When we consider the average peak force for each of the cluster types, there appears to be an increase in adhesive force with increasing cluster size. However, we find no statistically significant effect of pillar clustering.

The challenging nature of these experiments means that the lack of an effect of clustering on the adhesive performance could either be due to the lack of a true effect, or because this effect is hidden in the significant error bars. The relatively large spread in the data results from a number of experimental details. One contribution is the relatively low data rate of $1\,s^{-1}$ at which these samples are measured. Additionally, the sample size is rather large relative to the feature size. This makes that a slight convex or concave curvature of the sample can significantly impact the adhesive properties of the entire sample. This effect is partially addressed through the application of a preload cycle. A more minor effect may be hiding in the shape of the micropillars. The lithography process results in rounded square features in the final sample, as well as some variation between samples; starting with cylindrical pillars may provide a valuable optimisation. A final consideration is the actual sample design; whereas a gecko foot displays a multi-dimensional approach to contact splitting and micropatterning, our samples only vary the cluster size, hence the average pillar spacing remains constant throughout the samples.

Nonetheless, if the effect of clustering is hidden, it must be very minor. To improve the experiment, one would need to address a vastly larger experimental space, where feature size, aspect ratio, backing layer properties, and many more parameters are adjustable. We did perform some experiments in which we decreased the backing layer thickness for clustered samples from 1.5 mm to 0.25 mm, but no significant differences were observed. The effect of backing layer thickness has been described theoretically [33]. Here, the authors define a macroscopic sample aspect ratio AR_1, which depends on the total sample size and thickness, as well as a microscopic pillar aspect ratio AR_2, comparable to the pillar aspect ratio we discussed in Section 2.3.1. The macroscopic aspect ratio is defined as $AR_1 = H/nD$, where H is the backing layer thickness, n the number of pillars and D the spacing between pillars. It is found that a very low ($AR_1 < 0.1$) or a very high ($AR_1 > 4$) aspect ratio for a backing layer thickness leads to advantageous adhesive properties [33]. The theory behind this is that for very low aspect ratios, the backing layer does not deform, and adhesive energy is mostly carried by the pillars. At increasing aspect ratios, the backing layer gradually starts to deform, and the stresses are now shared between pillars and the backing layer. As a result of the backing deformation (necking), extra stress is exerted in the edge pillars. Subsequently, at very high aspect ratios, the necking of the backing layer is reduced again as it is spread over a very large volume, reducing edge stresses. For our samples, we have $AR \approx 0.07$ for the original samples, and $AR \approx 0.01$ for the thin samples. As both samples are below the lower limit mentioned above, the absence of an effect on adhesion is indeed to be expected.

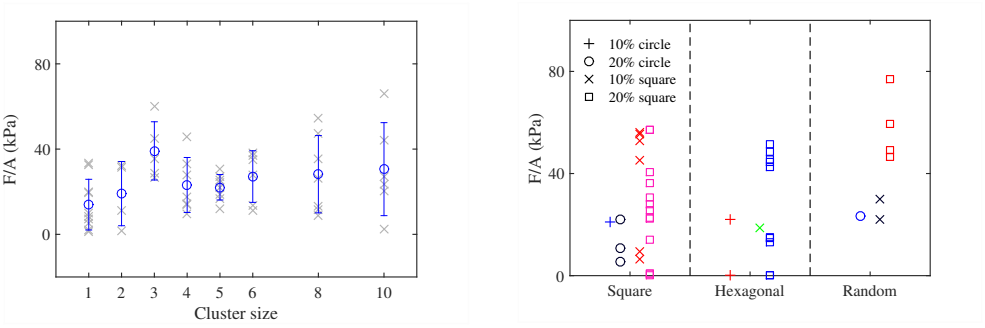

Figure 2.7 – Results of adhesion tests, showing peak force per unit area. (a) Clustered samples; gray crosses indicate independent measurements; each individual measurement is an average of 5 runs. Error bars indicate 1σ. (b) Patterned samples. Symbols indicate the sample density (10–20 %) and the overall sample shape (square or circle). We observe no significant difference between clusters, sample shape, density, or pillar arrangement.

Patterned adhesives with variable ordering

In literature it is claimed that patterning an adhesive material improves its properties [21, 24], and in certain cases, that a regularly patterned sample outperforms the adhesive properties of an adhesive with random patterning [12]. To investigate the effects of order versus disorder, as well as the presence of certain defects in an ordered structure, we compare a perfect 2D crystalline micropillar arrangement with a random placement of the same number of micropillars. In addition, we create ordered micropillar arrays with a central grain boundary defect designed into the sample. We design these samples with cylindrical instead of square pillars. This is expected to improve lithographic results, as well as eliminate potential edge effects on individual pillars. The design of these samples is described in more detail in Section 2.2.3, and examples of the resulting patterns are shown in Figure 2.4. The hypothesis is that a crackfront will follow a certain lattice direction. As there is no clearly defined lattice direction in a random array, the expectation is that the force required to propagate the crackfront in an ordered sample is higher than in a random sample. The reason for this is that if the crackfront occurs in a straight line, continuation of the front requires a large number of pillars to detach simultaneously in an ordered sample, whereas in a random sample, pillars do not occur in a straight line, and are expected to detach on an individual basis.

By comparing adhesive properties of a square with an otherwise identically or-

dered or disordered circular sample we hope to investigate the effect of corners of the sample as a whole. We choose to keep the diameter of the circle equal to the side of the square sample, to keep the maximum sample size identical. The difference in (effective) contact area is corrected afterwards, when we calculate the adhesive force or energy per unit area. These samples are tested in the same manner as before. In addition to the measurements on the rheometer, we complement these data with measurements on the TIRM setup to visualise the adhesive contact during failure. We initially discuss the force measurements obtained with this setup, and continue with an investigation of the optical data in the next section.

A plot of peak force per unit area is shown in Figure 2.7b. A direct comparison with literature [12] is not possible, as this article shows a dependence on force per unit area on retraction speed, and the lowest speed tested in their article ($4\,\mu m\,s^{-1}$) is significantly higher than our retraction speed of $1\,\mu m\,s^{-1}$. Nevertheless, the peak force per unit area for ordered samples for both experiments is in the same order of magnitude, as we find an average of approximately 20–60 kPa, where literature shows a peak force of approximately 30 kPa for ordered samples retracted at $4\,\mu m\,s^{-1}$.

Next we compare samples to find a potential effect of pillar density. The most suitable samples are those with square pillar order in a square geometry, as for these samples a similar number of data points is acquired for both densities. From this, we observe no difference in the two densities. With regards to global sample geometry, we find that circular samples perform slightly worse than square samples, as this trend is visible for all three pillar geometries. This is counterintuitive, as sharp corners in general lead to stress buildup. We have no explanation for the absence of this phenomenon here.

Lastly, we compare the effect of ordered (square or hexagonal) versus disorderded (random) pillar placement. Where literature finds that the peak force of an ordered sample is nearly an order of magnitude higher than that of random samples [12], we find that the two best performing samples in our investigation have random order. Besides this, the average peak force per unit area is the highest for this sample category, albeit in the same order of magnitude as that of ordered samples. We also find a relatively low standard deviation for random samples, although this may be within experimental error. To explain these results, we have to look at the microscopic effects described in Section 2.3.3, followed by a discussion of the observed differences on page 32.

2.3.3 TIRM

Macroscopic effects

While the adhesion measurements provide insight into the mechanical performance of a micropatterned adhesive, they do not provide direct insight into the microscopic

mechanisms by which detachment occurs. To study adhesive failure at the scale of the individual pillars, we use total internal reflection microscopy (TIRM) to visualise the detachment process at the microscopic scale.

We first consider the macroscopic side of the data. With particle tracking software, we determine the number of attached features as a function of time. From these detachment curves we can reconstruct the speed and acceleration of adhesive failure, and determine the driving process. First, we attempt to find distinguishing features in the failure curves of various samples. Examples are shown in Figure 2.8. In these graphs, the number of counted features N in a given frame is normalised to the total number of pillars in that sample $N_{\max}$, such that for full coverage and complete tracking accuracy, the normalised number of attached pillars $N_a = N/N_{\max} = 1$, regardless of sample shape or density. Detachment curves are plotted against time, where we define t_0 as the time when the number of counted features drops below an arbitrary threshold. The threshold chosen here is $N_a < 0.1$. In nearly all cases, the particle tracking algorithm is able to find most pillars. Only in a few samples we find that the maximum number of attached pillars is smaller than $N_{\max}$. This can be due to sample defects or due to a partly attached sample. In some cases, it is a result of optical misalignment, leading to the sample being partially out of focus, limiting the efficiency of the tracking algorithm.

The different samples show very similar detachment curve shapes, regardless of pillar order, density, or the presence of a grain boundary. We find that once a few pillars detach, we observe an increasingly rapid decrease in the number of adhered pillars. This corresponds to the description of a kinetic crack growth situation for the adhesive fracture of polymer bonds [34]; it is interesting to find that adhesive failure pattern of our macroscopic structures is akin to polymer bond fracture.

Microscopic effects

Although macroscopic effects determine the overall adhesive behaviour of a sample, and offer a facile comparison between samples, we also investigate the microscopic effects of adhesive failure by examining the starting point of adhesive failure, as well as the direction and shape of the developing crackfront. As described before, we expect adhesive failure to start in a corner, and (for ordered samples) progress over the sample along one of its lattice directions, as indicated in earlier literature studies [12].

However, typical experiments show that although failure frequently starts in a corner, the actual crackfront is not linear. An example of this behaviour on a sample with square pillar order is shown in Figure 2.9a. Here we see that the crackfront starts at the top right corner of the sample, but then spreads to the center of the sample, before peeling off towards the top right corner of the sample. Although this shows that there is not a clearly defined crackfront along one of the lattice directions of the

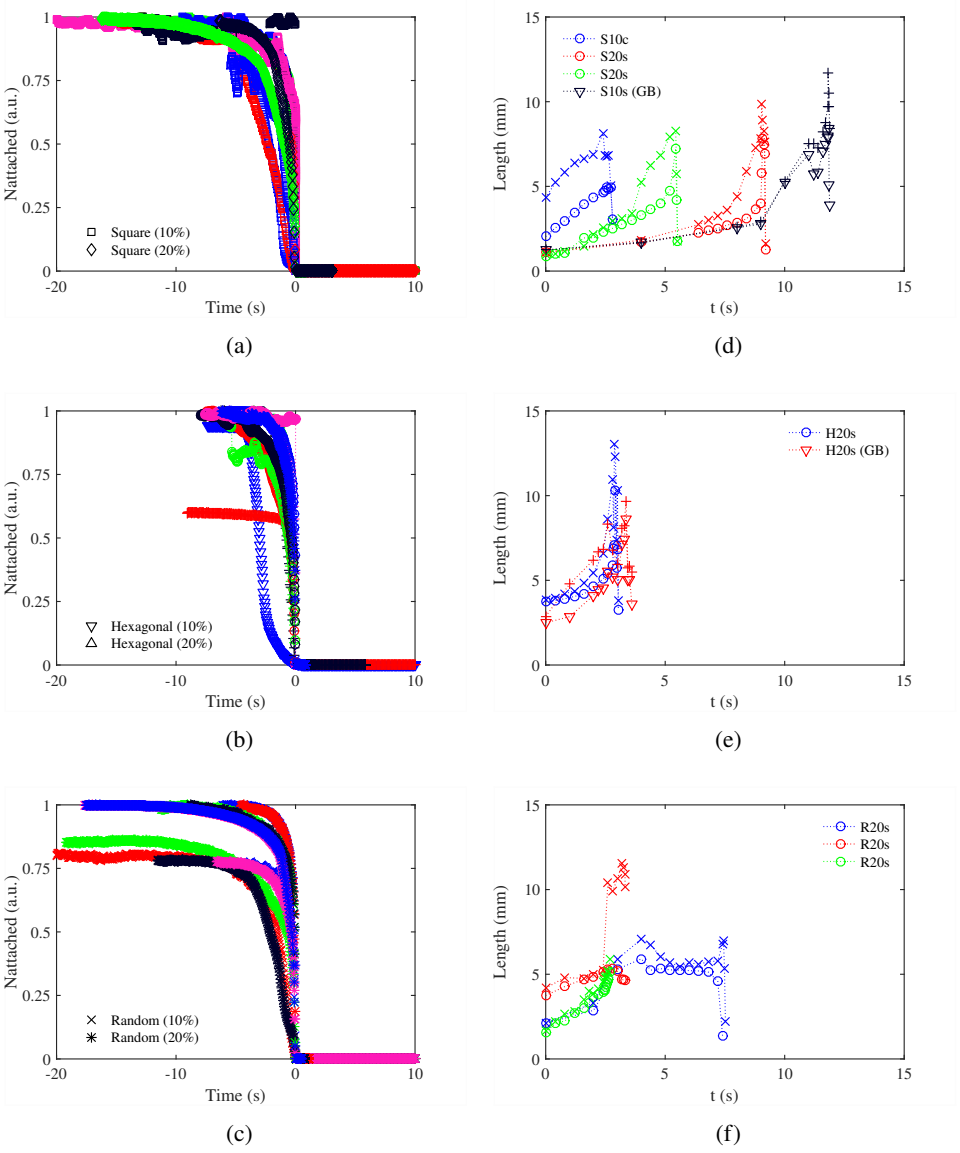

Figure 2.8 – Left column (a, b, c): Detachment of patterned surfaces from a glass slide. The plots show the normalised number of attached pillars N_a at a given time, with $t_0 \equiv N_a < 0.01$. We observe no significant differences between patterns or pillar densities. Right column (d, e, f): The evolution of front length $(+, \times)$ and chord length $(\circ, \Delta)$ as a function of time. The legend indicates the sample geometry (Square, Hexagonal, Random), density (10 or 20 %), and sample shape (square or circle), as well as the presence of an artificial grain boundary (GB).

sample, to the eye it appears that the *average* crackfront may follow lattice directions.

In order to quantify this effect, we manually trace the outline of the crackfront in a sequence of frames for a given sample, in order to calculate the total crackfront length. We also look at the average crackfront angle and length, which we define as the angle of the chord connecting the outermost edges of the crackfront in the sample. We follow the development of this angle as a function of time in order to determine whether adhesive failure follows lattice directions. We determine the crackfront length for 11 different samples. We define t_0 at the onset of adhesive failure. Of these, 9 samples show a steep, exponential-like increase in crackfront length from t_0, until the last pillar detaches. For the remaining two samples we find that the crackfront length increases initially, then stabilises until the sample is completely detached. This happens to one of the square samples, a hexagonal sample with grain boundary, and one of the two analysed random samples. We therefore conclude that it is most likely experimental variation, and not caused by certain sample features. Front length and chord length graphs are plotted in Figure 2.8 d–f. The difference between each set of curves shows that front length and chord length do not overlap. This is a result of the fact that adhesive failure does not follow a straight front. Also, the slow increase and sudden drop in front length is another indication that the crackfront does not progress as a parallel sweep across the sample, as would be the case for purely lattice-driver behaviour.

If we look at the crackfront on a per-frame basis, we find no obvious pattern. However, after some initial fluctuation at the start of adhesive failure, we find that the crackfront reaches a stable direction, until it touches on the opposite side of the sample. At that moment, we reach the moment of catastrophic failure, and the crackfront rapidly sweeps over the remainder of the sample.

With these results, we can now continue the discussion on the observed discrepancy between our finding that samples with random pillar placement have a slightly higher adhesive force per unit area than ordered samples, as opposed to results published in literature [12], where the adhesive performance of ordered samples is nearly an order of magnitude better than that of random samples. In their article, the authors show a number of stills from one of the experiments with an adhesive array of square order, reproduced in Figure 2.10a. These stills clearly show the propagation of a perfectly 'flat', linear crackfront across the sample, switching a few times between the (1 2) and (2 3) lattice directions. No results are shown for random samples, but in their discussion it is suggested that also for these samples, the crackfront can be approximated by a straight line for all samples [12]. This forms the basis for the hypothesis that propagation of a crackfront in a straight line requires a much higher force for ordered samples than for random samples. However, in our samples, we rarely find a straight crackfront, instead, we nearly always observe adhesive failure to propagate towards the center of the sample and then spreading out to the edges. In

this case, the straight line hypothesis is flawed. Now, there is no lattice direction to follow, and in this case, random samples are not a priori expected to perform worse than ordered samples.

In order to further investigate the presence or absence of lattice-driven behaviour, we analyse the average crackfront angle for a large number of samples. We normalise the angle to 0°–45° for samples with square order and random samples, and to 0°–30° for samples with hexagonal order, taking the sample symmetry into consideration. Results are shown in Figure 2.10b. We find that there is very little indication of this lattice-driver behaviour, as only the hexagonal sample seems to adhere somewhat to a lattice direction, in particular the (4 -1) direction, which has an angle of 10.89°. If we forgo the hypothesis of lattice-driven adhesive failure, we can draw one more important conclusion from our data. For samples with square order, the number of pillars per unit length is highest in the (1 0) direction, corresponding to an angle of 0°. The second highest pillar density is at the (1 1) lattice direction at an angle of 45°. From here, the pillar density decreases with decreasing angle. For a sample with length $L \sim \infty$, we only touch two pillars at the $(1\,n)$ lattice direction, which equates to a pillar density $n/L \sim 0$. As we can see in the graph, the lower angles appear with higher frequency. The peak at 27° may be indicative of the (1 2) lattice direction, but this is highly speculative considering the spread in the distribution. If we combine these observations, as well as the images in Figure 2.9a, we conclude that our experiments contain no proof that ordered adhesive samples follow lattice directions upon adhesive failure, and therefore are not expected to exceed the performance of similar but disordered adhesive samples.

2.3.4 Lens probes and preload effects

We also explored the possibility of performing adhesion tests using a convex lens, as suggested in literature [14, 23]. The advantage of using the convex side of a lens instead of a flat contact area is that alignment effects are averaged out. However, a major disadvantage is that the effective contact area is drastically lowered. Another disadvantage is the presence of a preload effect with this setup. One can imagine that at precisely zero load, only a very small number of pillars is attached to the center of the lens, i.e. the spot with the largest protrusion into the sample. As the preload increases, so does the contact area; unlike for a flat probe, where the contact area is virtually 100 % from zero load onwards.

With said flat probe we investigated the reported load effect by measuring adhesion curves with a preload between 0.2–1 N in 0.2 N increments. We find the peak adhesive force to be constant in this range. However, it is expected that at extremely high preload, pillars eventually start to buckle or even break, thereby reducing their effectiveness. As a result of these findings, we conclude that our alignment method

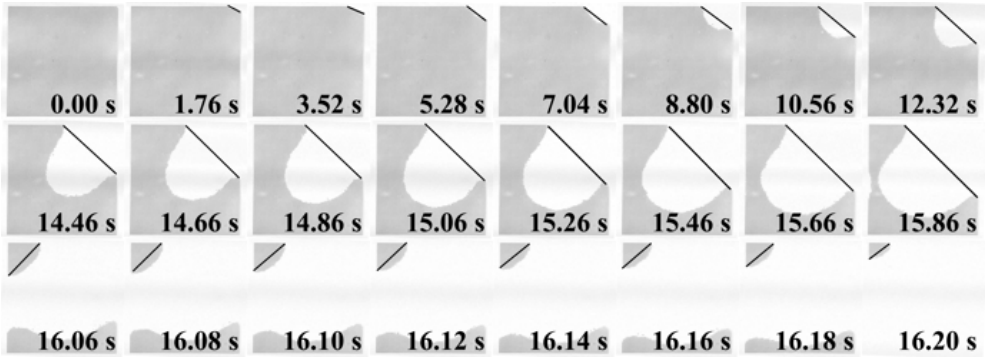

(a)

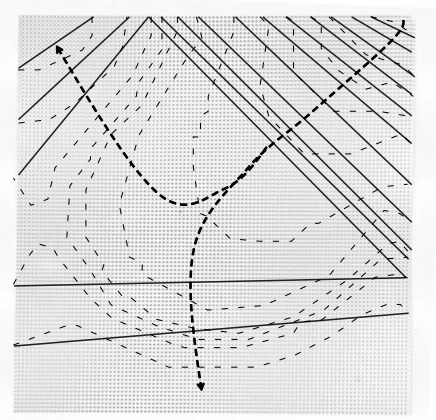

(b)

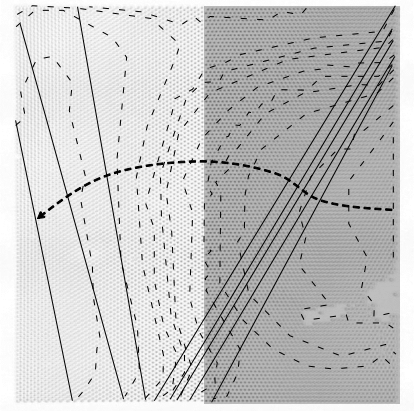

(c)

Figure 2.9 – Microscopic overview of adhesive failure. (a) A sequence of images showing adhesive failure. The time is shown in the bottom right corner. The solid black line shows the chord of the crackfront, the angle of which is used to estimate the average crackfront angle. The crackfront length is defined as the length of the perimeter of the detached area, enclosed by the chord. (b) Tracing the outline of the crackfront (dashed line) and the chord (solid line) on an adhesive sample with square geometry, and (c) a similar trace for a sample with hexagonal pillar placement and an artificial grain boundary. The two sides of the grain boundary are shaded differently for clarity. Note how the crackfront appears to arrest at the boundary: once the outer edge of the crackfront reaches the grain boundary, we observe a temporary decrease in front length until the front nearly completely coincides with the grain boundary, followed by an increase in front length and further detachment of the sample. Traced outlines are not equidistant in time; the dashed arrow indicates the general direction of adhesive failure in these particular samples.

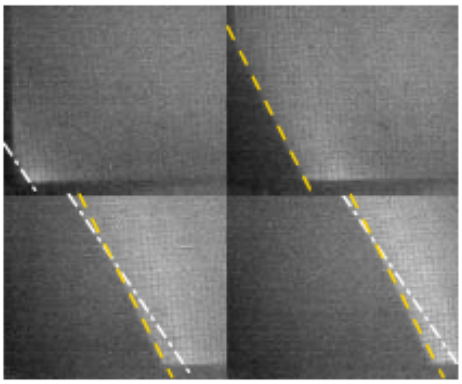

(a)

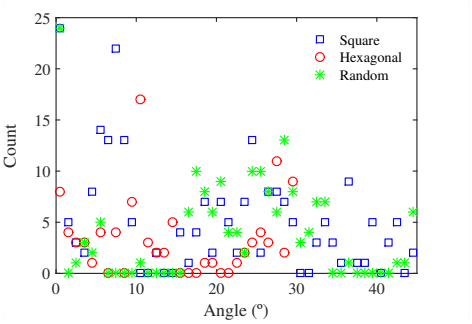

(b)

Figure 2.10 – (a) Square-ordered samples following a lattice direction upon adhesive failure. Reproduced from [12]. (b) A histogram showing the normalised crackfront angle for a number of square, hexagonal, and randomly oriented samples. We observe no clear lattice-driven behaviour for our ordered samples.

of placing the adhesive sample on the substrate, followed by attachment of the probe to the sample provides sufficiently precise alignment for our experiments.

2.3.5 Qualitative assement of a 'supercompliant' adhesive

As mentioned in the introduction, literature describes that very thin keratin fibrils, such as gecko setae, have a shear modulus and as a result, a spring constant several orders of magnitude smaller than the corresponding bulk material [29]. As a result, these setae are tacky and highly compliant. We qualitatively investigated this effect, which we call the 'compliant pillar' theory, with a laboratory experiment by creating an adhesive sample with an excessively long and flexible backing layer. For this, we start with a regular 10 % crosslinked PDMS adhesive sample, but we do not remove it from the wafer yet. We prepare a number of 1 mL BD Plastipak syringes by fluorinating them, and fill these with a 5 % crosslinker PDMS premix. In filling the syringes, we remove the plunger, and place them 'handle down' on top of the as-prepared adhesive samples. A number of these are placed over a patterned surface, but we also prepared an example on a flat wafer surface. The entire assembly with the standing, inverted syringes is carefully degassed and subsequently baked according to the normal PDMS curing protocol. To separate the syringe from the sample, we cut off the tip and reinsert the syringe from this side, and carefully push the PDMS tube out. The resulting sample as a regular 10 % PDMS adhesive 'head' with a ca. 5 cm long, 5 mm diameter cylindrical 'tail'. What we effectively made here is one

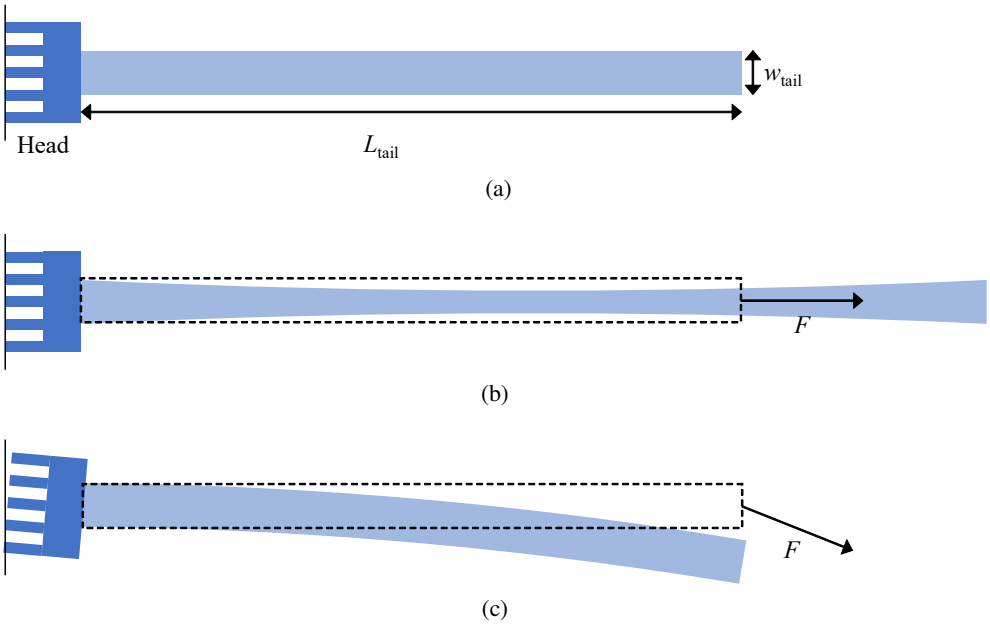

Figure 2.11 – (a) Illustration of an adhesive sample (crosslink density 10 %) with an excessively thick backing layer (crosslink density 5 %); $L_{\text{tail}} \approx 5$ cm, $w_{\text{tail}} \approx 5$ mm. (b) Upon the application of a force F parallel to the 'tail', the backing layer stretches and significant necking occurs, before the sample is finally detached. (c) If a perpendicular component is added to F, the 'tail' just buckles, and the sample releases, virtually without resistance.

pillar with an aspect ratio of 1000. Unfortunately, due to the flexibility of the tail it proves impossible to test the sample with the regular adhesive setup. However, when we attach the sample and attempt to removed it by hand in the direction of the 'tail', we find that the 'tail' stretches considerably, and that the (subjective) adhesive force is significantly increased compared to a regular adhesive sample. On the other hand, when the sample is peeled of at an angle, the 'tail' buckles and the adhesive force is virtually zero. This is remarkably close to the gecko behaviour: highly adhesive in one direction, facile peel-off at an angle. An illustration of the sample and the stretching and buckling of the 'tail' is shown in Figure 2.11.

2.4 Computer simulations

Besides the experiments described above, we performed computer simulations to investigate adhesive properties of patterned samples. Computer simulations allow for variation of a wide range of experimental parameters at relatively low cost in a short amount of time. In this simulation, we model an array of N pillars that are attached to a semi-infinite elastic solid with a given Young's modulus E and Poisson ratio ν. From this we can calculate an effective modulus $Y = E/(1-\nu)$. Pillar variables are their length L_0, radius a. Their effective spring constant is calculated as $k = \pi a^2 E/L_0$. We simulate a displacement u_0 of the substrate, which leads to stretching of the pillars and deformation of the solid. The force exerted on a pillar is calculated as $f_i = k_i(u_0 - u_i)$, where u_i is the local deformation of the substrate. To calculate the deformation of the matrix by the pull of a cylindrical pillar, we use the well-known literature result for the deformation of an elastic matrix by a solid cylindrical punch [35]:

$$u_i(\rho) = \begin{cases} \frac{f_i}{2aY} & (\rho \le a) \\ \frac{f_i}{a\pi Y} \arcsin\frac{a}{\rho} & (\rho > a), \end{cases} \tag{2.1}$$

hence the deformation is proportional to the applied force at any position within the pillar radius ρ itself, while the function $\arcsin a/\rho$ ensures that the deformation falls to zero when moving away from the pillar centre.

We consider the total deformation of the entire slab of elastic solid by calculating the effect of all pillars together, and use a Green's matrix to calculate the effect of each pillar on every other. The total deformation at position r is the sum of the individual pillar contributions

$$u(r) = \sum_i u\left(|r - r_i|\right), \tag{2.2}$$

or

$$u_i = u(r_i) = \sum_j G_{ij}(u_0 - u_j), \tag{2.3}$$

where G_{ij} is the Green's matrix that describes the response at pillar i to a force at pillar j:

$$G_{ij} = \begin{cases} \frac{k_j}{2a_jY} & (i = j) \\ \frac{k_j}{a_j\pi Y} \arcsin\left(\frac{a_j}{r_{ij}}\right) & (i \ne j) \end{cases}. \tag{2.4}$$

For detached pillars, $G_{ij} = 0$. A sketch of the effect of separation on matrix and pillar deformation is provided in Figure 2.12.

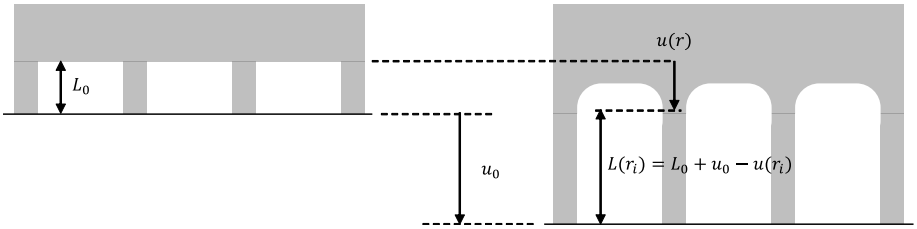

Figure 2.12 – Illustration of pillar and matrix deformation as a result of an applied separation. Pillars with length L_0 are attached to an elastic matrix. The application of a force leads to a separation u_0, which deforms the matrix by an amount u_r, and stretches the pillars to a length $L(r_i) = L_0 + u_0 - u(r_i)$.

We assume that pillars detach stochastically, with a detachment rate that depends on the force exerted on the pillar. We use the stochastic Gillespie algorithm [36] to simulate the detachment of the pillars; after each detachment event we calculate the forces on each pillar, and the resulting detachment rate. This is used to determine the next pillar to detach, and the time needed for this event to happen. Following the experiments, we assume a constant separation rate v, which implies that the rate constants change continuously as a function of time. To account for this, we implement the modified Gillespie algorithm according to Anderson [37], and calculate the detachment rate k_d as

$$k_{\mathrm{d},i} = \begin{cases} k_{\mathrm{d},0}\left[\exp\left(\frac{f_i - f_c}{f^*}\right) - 1\right] & (\text{if } f_i > f_c) \\ 0 & (\text{if } f_i \leq f_c) \end{cases}, \tag{2.5}$$

where $k_{d,0}$ a detachment rate parameter, f_c is the critical force below which the pillar cannot detach, and f^* sets the force dependence of the detachment rate.

The model contains a number of parameters:

- The ratio k/aY gives the compliance ratio between the pillars and the elastic backing matrix. For $k \gg aY$, the matrix is soft, so that elastic deformations can propagate from one pillar to the next; for $k \ll aY$ the matrix is rigid and pillars cannot interact.

- The average distance $\langle r \rangle$ between neighbouring pillars: for $\langle r \rangle \gg a$ pillars are far apart, so that they do not influence each other.

- f_c and f^*: for $f_c \gg f^*$, pillars detach rapidly once the force exerted on it exceeds the critical force f_c; for $f_c \ll f^*$ the detachment rate increases more gradually, so that the detachment becomes more stochastic. Here we use $f_c/f^* = 0.1$.

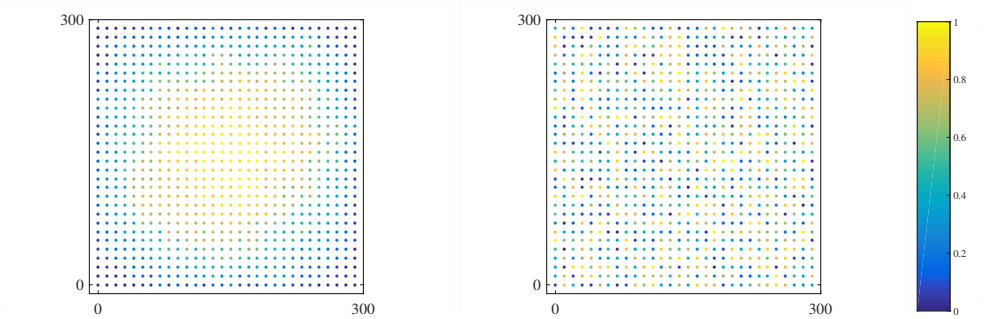

Figure 2.13 – Two different detachment regimes, (a) $k/aY \gg 1$ and $\langle r \rangle$ is small. Pillars influence each other, stress concentration occurs near the sample edges, and pillar detachment is deterministic. (b), $k/aY \ll 1$ and $\langle r \rangle$ is large, and pillar detachment is stochastic. The colour bar indicates the relative pillar release time $t/t_{\max}$.

- The relative detachment rate $v/k_{\mathrm{d},0}$ specifies how fast the surfaces are separated compared to the pillar detachment rate.

We use $k = 1$, $a = 3$, and $k_{\mathrm{d},0} = 1$ in all our simulations.

2.4.1 Results

As described above, two different detachment scenarios exist. In the first scenario, for experiments where $k/aY \gg 1$ and $\langle r \rangle$ is small, pillars influence each other, and stresses concentrate. In this case, pillar detachment occurs by crack propagation. In the second scenario, $k/aY \ll 1$ and $\langle r \rangle$ is large, individual pillars detach in a random sequence. Both scenarios are illustrated in Figure 2.13.

Effects of separation velocity As the simulations in the deterministic regime are most similar to our experimental observations, all following simulations are performed in this regime. We thus fix $Y = 1$, and $\langle r \rangle / a = 10$. First, we investigate the effect of velocity. We look at the normalised force F/Nf_c versus displacement vt, the normalised number of attached pillars as a function of displacement, as well as the normalised force maximum $F_{\max}/Nf_c$ versus velocity. We find that the resulting curves are very similar to our experimental results, with a linear increase in force until a certain maximum force is reached, followed by a rapid dropoff and catastrophic adhesive failure. Results are shown in Figure 2.14. We observe that with increasing separation velocity, the peak force increases. As indicated in Figure 2.14c, this

increase is limited or nonexistent for low separation velocities. In this regime, once a certain pillar exceeds the critical force f_c, a crack nucleates that leads to adhesive faillure. At higher separation velocities, we find that the separation velocity is faster than crack propagation. As a result, the maximum force $F_{\max}$ keeps increasing as $F_{\max} \sim \log v$ for higher separation velocities. This is similar to results reported in literature for the process of bond rupture in gels under increasing shear strength [38].

Pattern effects We investigate the effect of patterns by comparing square arrays of pillars, placed in a homogeneous square grid, in square clusters, or with random placement. For the random sample, we keep the number of pillars N and the total sample size equal to that of the homogeneous sample, such that the average pillar spacing remains constant. We run the simulation with two different velocities, one from each regime indicated in Figure 2.14c. In both regimes, we find that patterns with random pillar placement do not differ significantly from the sample with a homogeneous square pattern, but we do observe a higher margin of error for these samples. Results are shown in Figure 2.15. There appears to be an optimum cluster size, as the maximum force increases with increasing cluster size, and decreases again for samples consisting of only 4 superclusters. A possible reason for this is that clusters leave larger gaps between pillars at regular intervals. They might act as 'crack stoppers'. However, within a cluster, stress concentration at the edges increases with increasing cluster size, and as a result, a compromise is best. We note that the effect is relatively weak, with a 4 % increase at high separation velocity, or up to 12 % for low separation velocities.

2.4.2 Discussion and comparison of adhesive experiments and simulations

In the section above, we have described our efforts into computer simulations of adhesive samples. We find two distinct detachment regimes, a stochastic regime, where pillar detachment is independent of its position within the sample, and a deterministic regime. We find this deterministic regime for sample conditions where pillars are allowed to influence each other, such as is the case for densely packed samples, and samples with an elastic backing matrix. These conditions allow for stress concentration at the sample edges, and in particular the corners. As the most stressed pillars at the corners detach first, a crack front nucleates that gradually progresses towards the sample center. This behaviour is similar to our laboratory experiments described before.

In our laboratory experiments we failed to distinguish a significant effect of clustering or patterning on adhesive performance, partially due to a large margin of error in these experiments. The simulations presented in the previous section suggest

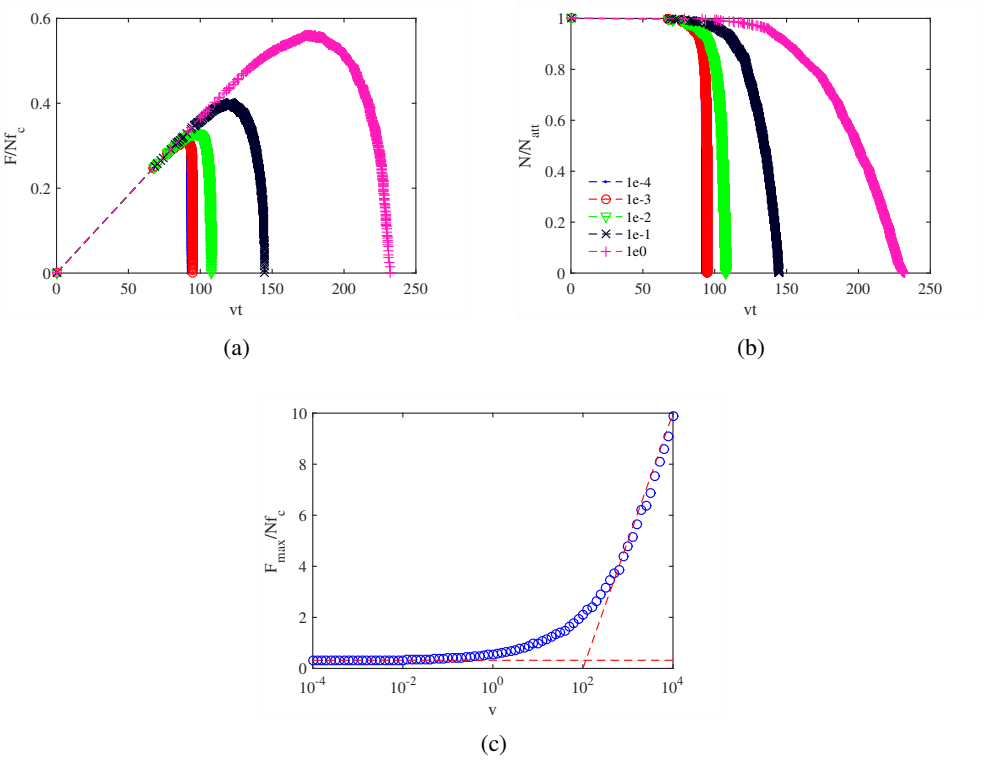

Figure 2.14 – Effects of separation velocity. (a) Normalised force and (b) ratio of attached pillars versus displacement vt for a selection of simulated velocities, as indicated in the legend. (c) Plot of the normalised force maximum as a function of separation velocity v. We observe two regimes, at low v, $F_{\max} \approx$ const, and at high separation velocity, $F_{\max} \sim \log v$. The red dashed lines are added as a visual aid to highlight the two regimes.

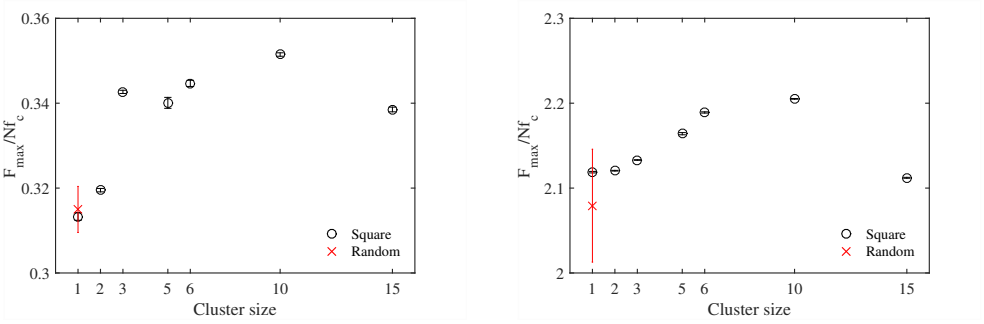

Figure 2.15 – Computer simulation results: Effects of sample patterning

that random pillar placement does not significantly affect adhesive performance, but leads to a higher margin of error. This is to some extent in disagreement with our laboratory experiments, where results indicate a slight performance edge of random samples over those with regular pillar placement, although the significance of that observation was limited. We did not include the hexagonal pattern in our simulations. However, simulations show a clear advantage of clustering on adhesive performance, unlike our laboratory experiments. We make two observations regarding this point. First, although the increase in peak force is significant, it is rather limited and easily concealed by noisy experimental data. More important is the position of the optimum. In our simulations, this is found at a cluster to sample size ratio of $1/6$–$1/3$. In our laboratory experiments, this ratio was $1/24$ or lower. This essentially means that all our laboratory experiments have been performed at the very low end of cluster sizes compared to the simulations, further obscuring the potential of clustering.

2.5 Conclusion

The above research presents our efforts to investigate and improve the effects of surface patterning on adhesive properties. In literature, earlier research points out a beneficial effect of patterning, in particular regularly ordered patterning, towards adhesive properties. However, from our investigations we conclude that it is difficult to prove this theory. We find that many trivial experimental details affect the outcome of our experiments. Above we described our efforts to limit the number of these details, or to improve their reproducibility, for instance through improving the lithography process, by using a constant backing thickness between the samples, and by various different experimental and protocol enhancements. Regardless, we find no statistically

significant impact of either clustering or ordered versus disordered patterning methods on adhesive properties within the experimental noise.

Computer simulations can be a valuable tool in investigating a large parameter space with a relatively low effort in cost and time, compared to lab experiments. Our model shows that under certain circumstances, clustering of pillars can have a beneficial effect on adhesive performance. The most important observation of this study, both in vitro as well as simulated, is that adhesive failure nearly always starts at the sample edges. We speculate that this is a result of an increased build-up of normal stresses near the sample edges, strongly supported by our computer simulations. This in turn results in the nucleation of adhesive fracture in those positions. Combined with our observation that adhesive failure is a self-catalytic catastropic event, corroborated by earlier literature studies [34], the prevention of fracture nucleation would initially have a more significant impact on adhesive properties. This can be attained by optimising the edge conditions. At a later stage, one can move on to fracture retardation or even arrest by tuning the bulk of the sample.

References

[1] J. Koller, U. Brauner, and D. Mania. High-Tech in the Middle Palaeolithic: Neanderthal Manufactured Pitch Identified. *European Journal of Archaeology*, **2001**. *4*, 385–397. doi:10.1179/eja.2001.4.3.385.

[2] E. A. Marques, L. F. Da Silva, M. D. Banea, and R. J. Carbas. Adhesive joints for low- and high-temperature use: An overview. *Journal of Adhesion*, **2014**. *91*, 556–585. doi:10.1080/00218464.2014.943395.

[3] D. Small and P. Courtney. Fundamentals of industrial adhesives. *Advanced Materials and Processes*, **2005**. *163*, 44–47.

[4] M. D. Banea, L. F. M. da Silva, R. D. S. G. Campilho, and C. Sato. Smart Adhesive Joints: An Overview of Recent Developments. *The Journal of Adhesion*, **2014**. *90*, 16–40. doi:10.1080/00218464.2013.785916.

[5] V. A. Gerasin, E. M. Antipov, V. V. Karbushev et al. New approaches to the development of hybrid nanocomposites: from structural materials to high-tech applications. *Russian Chemical Reviews*, **2013**. *82*, 303–332. doi:10.1070/RC2013v082n04ABEH004322.

[6] M. B. Jakubinek, B. Ashrafi, Y. Zhang et al. Single-walled carbon nanotube-epoxy composites for structural and conductive aerospace adhesives. *Composites Part B: Engineering*, **2015**. *69*, 87–93. doi:10.1016/j.compositesb.2014.09.022.

[7] L. M. Butkus, P. D. Mathern, and W. S. Johnson. Tensile properties and plane-stress fracture toughness of thin film aerospace adhesives. *Journal of Adhesion*, **1998**. *66*, 251–273. doi:10.1080/00218469808009968.

[8] Arthur L. Fry. Repositionable pressure-sensitive adhesive sheet material, **1993**.

[9] C. Heinzmann, C. Weder, and L. M. de Espinosa. Supramolecular polymer adhesives: advanced materials inspired by nature. *Chem. Soc. Rev.*, **2016**. *45*, 342–358. doi:10.1039/C5CS00477B.

[10] J. Yang, J. Keijsers, M. van Heek, A. Stuiver, M. A. Cohen Stuart, and M. Kamperman. The effect of molecular composition and crosslinking on adhesion of a bio-inspired adhesive. *Polymer Chemistry*, **2015**. *6*, 3121–3130.

[11] S. Akerboom, J. Appel, D. Labonte, W. Federle, J. Sprakel, and M. Kamperman. Enhanced adhesion of bioinspired nanopatterned elastomers via colloidal surface assembly. *Journal of the Royal Society, Interface / the Royal Society*, **2015**. *12*, 20141061. doi:10.1098/rsif.2014.1061.

[12] H. E. Bakker, S. B. Lindström, and J. Sprakel. Geometry- and rate-dependent adhesive failure of micropatterned surfaces. *Journal of Physics: Condensed Matter*, **2012**. *24*, 065103. doi:10.1088/0953-8984/24/6/065103.

[13] M. D. Bartlett, A. B. Croll, and A. J. Crosby. Designing bio-inspired adhesives for shear loading: From simple structures to complex patterns. *Advanced Functional Materials*, **2012**. *22*, 4985–4992. doi:10.1002/adfm.201201344.

[14] C. Greiner, A. Del Campo, and E. Arzt. Adhesion of bioinspired micropatterned surfaces: Effects of pillar radius, aspect ratio, and preload. *Langmuir*, **2007**. *23*, 3495–3502. doi:10.1021/la0633987.

[15] S. Hu and Z. Xia. Rational design and nanofabrication of gecko-inspired fibrillar adhesives. *Small*, **2012**. *8*, 2464–2468. doi:10.1002/smll.201200413.

[16] E. Huovinen, J. Hirvi, M. Suvanto, and T. A. Pakkanen. Micro-micro hierarchy replacing micro-nano hierarchy: A precisely controlled way to produce wear-resistant superhydrophobic polymer surfaces. *Langmuir*, **2012**. *28*, 14747–14755. doi:10.1021/la303358h.

[17] A. Jagota and C.-Y. Hui. Adhesion, friction, and compliance of bio-mimetic and bio-inspired structured interfaces. *Materials Science and Engineering: R: Reports*, **2011**. *72*, 253–292. doi:10.1016/j.mser.2011.08.001.

[18] M. Kamperman, E. Kroner, A. Del Campo, R. M. McMeeking, and E. Arzt. Functional adhesive surfaces with "Gecko" effect: The concept of contact splitting. *Advanced Engineering Materials*, **2010**. *12*, 335–348. doi:10.1002/adem.201000104.

[19] M. K. Kwak, C. Pang, H. E. Jeong et al. Towards the next level of bioinspired dry adhesives: New designs and applications. *Advanced Functional Materials*, **2011**. *21*, 3606–3616. doi:10.1002/adfm.201100982.

[20] B. Pokroy, S. H. Kang, L. Mahadevan, and J. Aizenberg. Self-organization of a mesoscale bristle into ordered, hierarchical helical assemblies. *Science (New York, N.Y.)*, **2009**. *323*, 237–240. doi:10.1126/science.1165607.

[21] C. Poulard, F. Restagno, R. Weil, and L. Léger. Mechanical tuning of adhesion through micro-patterning of elastic surfaces. *Soft Matter*, **2011**. *7*, 2543. doi:10.1039/c0sm01099e.

[22] M. Röhrig, M. Thiel, M. Worgull, and H. Hölscher. 3D Direct laser writing of nano- and microstructured hierarchical gecko-mimicking surfaces. *Small*, **2012**. *8*, 3009–3015. doi:10.1002/smll.201200308.

[23] T. Thomas and A. J. Crosby. Controlling Adhesion with Surface Hole Patterns. *The Journal of Adhesion*, **2006**. *82*, 311–329. doi:10.1080/00218460600646610.

[24] E. Arzt, S. Gorb, and R. Spolenak. From micro to nano contacts in biological attachment devices. *Proceedings of the National Academy of Sciences*, **2003**. *100*, 10603–10606. doi:10.1073/pnas.1534701100.

[25] D. Labonte, C. J. Clemente, A. Dittrich et al. Extreme positive allometry of animal adhesive pads and the size limits of adhesion-based climbing. *Proceedings of the National Academy of Sciences*, **2016**. *113*, 1297–1302. doi:10.1073/pnas.1519459113.

[26] W. J. Stewart and T. E. Higham. Passively stuck: death does not affect gecko adhesion strength. *Biology Letters*, **2014**. *10*, 20140701–20140701. doi:10.1098/rsbl.2014.0701.

[27] K. Autumn. How Gecko Toes Stick. *American Scientist*, **2006**. *94*, 124–132.

[28] A. P. Russell and T. E. Higham. A new angle on clinging in geckos: incline, not substrate, triggers the deployment of the adhesive system. *Proceedings of the Royal Society B: Biological Sciences*, **2009**. *276*, 3705–3709. doi:10.1098/rspb.2009.0946.

[29] K. Autumn. Gecko adhesion: Structure, function, and applications. *MRS Bulletin*, **2007**. *32*, 473–478. doi:10.1557/mrs2007.80.

[30] G. M. Whitesides. The origins and the future of microfluidics. *Nature*, **2006**. *442*, 368–373. doi:10.1038/nature05058.

[31] D. C. Hong and S. Yue. Deterministic chaos in failure dynamics: Dynamics of peeling of adhesive tape. *Physical Review Letters*, **1995**. *74*, 254–257. doi:10.1103/PhysRevLett.74.254.

[32] G. Josse, P. Sergot, C. Creton, and M. Dorget. Measuring Interfacial Adhesion Between a Soft Viscoelastic Layer and a Rigid Surface Using a Probe Method. *The Journal of Adhesion*, **2004**. *80*, 87–118. doi:10.1080/00218460490276821.

[33] E. Ginebre and S. B. Lindström. *Geometry-dependence of the adhesive strength of biomimetic, micropatterned surfaces*. Master's thesis, Linköping University, **2012**.

[34] M. K. Chaudhury. Rate-Dependent Fracture at Adhesive Interface. *The Journal of Physical Chemistry B*, **1999**. *103*, 6562–6566. doi:10.1021/jp9906482.

[35] I. N. Sneddon. The relation between load and penetration in the axisymmetric boussinesq problem for a punch of arbitrary profile. *International Journal of Engineering Science*, **1965**. *3*, 47–57. doi:10.1016/0020-7225(65)90019-4.

[36] D. T. Gillespie. Exact Stochastic Simulation of Copuled Chemical Reactions. *J Phys Chem*, **1977**. *81*, 2340–2361.

[37] D. F. Anderson. A modified next reaction method for simulating chemical systems with time dependent propensities and delays. *Journal of Chemical Physics*, **2007**. *127*. doi:10.1063/1.2799998.

[38] P. J. Skrzeszewska, J. Sprakel, F. A. de Wolf, R. Fokkink, M. A. Cohen Stuart, and J. van der Gucht. Fracture and Self-Healing in a Well-Defined Self-Assembled Polymer Network. *Macromolecules*, **2010**. *43*.

Part II

Soft wetting

Chapter 3

Polymer adsorption-induced contact angle hysteresis in hydrogel wetting

Abstract

We study the wetting properties of a range of different hydrogels. Hydrogel chemistry and morphology are tuned through the choice of monomer (acrylamide, *N*-isopropylacrylamide, and poly(ethylene glycol) methyl ether methacrylate). The effect of charge and salt is investigated by copolymerization of charged monomers with the hydrogel. pH-sensitive, switchable hydrogels are synthesised by copolymerising amino groups. Post-synthesis swelling depends on crosslink density and the presence of charge, either permanent or pH-induced. Counterintuitively, we find that oils spread completely, and that water only partially wets the hydrogel/air interface, regardless of the hydrophilic nature of these materials. We investigate this effect through static and dynamic contact angle measurements of air and oil at hydrogel/water interfaces. We observe unusually high contact angle hysteresis of oil on *N*-isopropylacrylamide gels, and demonstrate that this is a result of the adsorption of polymer chains at the air/water interface. Hysteresis is significantly reduced in permanently charged gels, but partly restored upon addition of salt to the water phase. To our knowledge, this is the first report of salt-induced contact angle hysteresis. Although the swelling behaviour of switchable, pH-sensitive hydrogels at pH $\ll$ pK_a is comparable to that of permanently charged hydrogels, their contact angle hysteresis is not significantly different from neutral *N*-isopropylacrylamide gels, or switchable gels at pH $\geq$ pK_a.

Maarten van Heek, Aljosha D. Filippov, Jasper van der Gucht, and Frans A.M. Leermakers. Polymer adsorption-induced contact angle hysteresis in hydrogel wetting (in preparation)

3.1 Introduction

A gel is a sparse polymer matrix, swollen with solvent. Gels are interesting materials from a number of perspectives. Their properties are adjustable through the choice of monomer, the degree of polymer crosslinking, the addition of copolymers or other additional chemical groups, and the choice of solvent. Hydrogels are a special class of hydrophilic, crosslinked polymer gels, swollen in water. These materials have existed for a considerable time, and have various established uses, both in science as well as in everyday life. An early and unremitting scientific application of hydrogels is their use in gel electrophoresis [1]. An example of a consumer application of hydrogels that has existed for a long time but is still relevant is their use as a material for contact lenses [2]. Hydrogels currently attract considerable interest in the scientific community for their use in advanced materials and biomedical applications, such as tissue engineering [3–5], and in high-tech applications such as the use of microgels for drug delivery [6], or in Pickering emulsions [7–9].

For nearly all these applications, interfacial properties play a key role when the material interacts with its surroundings, ranging from wetting properties of contact lenses to friction and (cell) adhesion in biomedical applications. However, studies on the wetting of hydrogels have received relatively little attention from the scientific community [2, 10, 11]. The phenomena investigated in these articles range from relatively straightforward dynamic wetting measurements to more complex subjects, such as the evolution of the contact angle of a droplet diffusing into a gel to the effect of addition of particles on contact angles.

Naively, one would expect that water should completely wet a hydrogel, which is essentially a hydrophilic polymer network swollen in water. However, self-consistent field calculations for hydrophilic polymer brushes suggest that this is not the case [12]. The authors argue that adsorption of polymer chains to the gel/water interface results in a finite contact angle, instead of complete wetting, and they find a correlation between the surface affinity of the polymer and the contact angle. The authors hypothesize that a similar effect should be observed for polymer gels. This wetting of gels is the subject of this chapter.

We can consider our gels as composed of a polymer material with dangling chains at the surface, and as such we expect their surface behaviour to be somewhat similar to that of a polymer brush. We expect adsorption of polymer chains at the gel-liquid interface, or at the three-phase contact line. In a static system, we expect this to result in a finite contact angle, and this adsorption might affect contact line dynamics as well, resulting in contact angle hysteresis. This effect is visualised in Figure 3.1.

For a liquid droplet at a solid surface, surrounded by vapour, the contact angle is determined by the balance of the surface tensions, according to Young's law $\gamma_{sl} = \gamma_{sg} - \gamma_{lg} \cos\theta$, where γ_{sl}, γ_{sg}, and γ_{lg} denote the surface tension of the solid-

liquid, solid-gas, and liquid-gas interface respectively, and θ the contact angle. Here, the gel is the solid, and the water is the liquid. In some of our experiments we replace the vapour phase by oil; in this case γ_{sg} and γ_{lg} are replaced by the gel-oil and water-oil surface tensions, respectively. In all our experiments, we measure the contact angle through the water phase. Young's law can be rearranged to

$$\gamma_{lg}\left(\cos(\theta) - 1\right) = \gamma_{sg} - \gamma_{sl} - \gamma_{lg}. \tag{3.1}$$

The right-hand side of this equation is known as the spreading parameter S. For polymers with no affinity for the interface, we expect depletion of polymer chains from the interface. The surface of such a hydrogel then effectively consists of water, and we expect complete wetting by a water droplet at the air/water interface. For complete wetting, $S = 0$, and then it follows that $\gamma_{sg,0} = \gamma_{sl,0} + \gamma_{lg,0}$. However, in case of polymer adsorption to the air/water interface, the polymer exerts an additional surface pressure Π, and alters the solid/gas surface tension, such that

$$\gamma_{sg} = \gamma_{sg,0} - c\Pi, \tag{3.2}$$

where c is an constant of order unity. Since the solid-liquid and liquid-gas surface tensions remain unaffected, $\gamma_{sl} = \gamma_{sl,0}$ and $\gamma_{lg} = \gamma_{lg,0}$. We can now combine Equations 3.1 and 3.2 to

$$\gamma_{sg} = \gamma_{sl} + \gamma_{lg} - c\Pi, \text{and} \tag{3.3}$$

$$\cos(\theta) = 1 - c\frac{\Pi}{\gamma_{lg}}. \tag{3.4}$$

This equation relates the contact angle θ to the surface pressure Π of an adsorbing polymer. For polymers with a finite surface pressure, we thus find partial wetting. Self-consistent-field calculations give $c = 1.391$ [12].

In this chapter we study hydrogel wetting with gels synthesised from a number of different polymers to investigate the effect of surface pressure of the polymer on static and dynamic contact angles. We synthesise hydrogels from acrylamide, *N*-isopropylacrylamide, and poly(ethylene glycol) methyl ether methacrylate (PEGMEMA) monomers. These materials allow us to test the effect of chemistry or morphology through adjustment of crosslink density or side chain mass. We test the effect of charge and salt by copolymerising potassium 3-sulfopropyl methacrylate with *N*-isopropylacrylamide, in order to obtain a permanently charged hydrogel. We also synthesise 2-aminoethyl methacrylate/*N*-isopropylacrylamide copolymers to obtain pH-sensitive hydrogels, and we demonstrate how charge and salt affect contact angle dynamics.

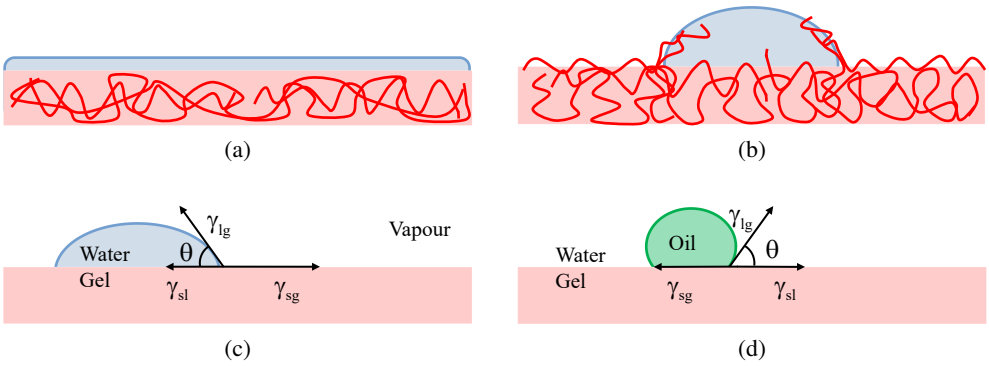

Figure 3.1 – The effect of polymer surface adsorption on wetting: (a) For hydrogels with nonadsorbing polymers we expect complete wetting of the hydrogel interface by water, whereas (b) adsorption of polymer chains to the interface could lead to partial wetting. (c) Young's law illustrated: the three-phase contact angle θ is determined by a force balance of the relative surface tensions γ_{sg}, γ_{sl}, and γ_{lg}. (d) For measurements on oil droplets we substitute the vapour phase for the oil phase in the equation.

3.2 Materials and methods

Hydrogels were synthesized in plastic petri dishes according to a free-radical synthesis method. A number of gels was supported on a methacrylated silicon wafer [13, 14]. Acrylamide (AAm), *N*-isopropylacrylamide (NIPAAm), and poly(ethylene glycol) methacrylate methyl ether (PEGMEMA, molecular weight 300, 475 or 900 g mol^{-1}) were used as monomers. Acrylamide and *N*-isopropylacrylamide gels were cross-linked with bis-acrylamide, and PEGMEMA gels with ethylene glycol dimethacrylate. Charged gels and pH-switchable gels were obtained by copolymerization of a pNIPAAm hydrogel with potassium 3-sulfopropyl methacrylate (SPMA) for permanently charged gels, methacrylic acid (MA) for base-sensitive gels, or 2-aminoethyl methacrylate HCl (AMA) for acid-sensitive gels. The reaction mixture pH was adjusted to be slightly acidic for the methacrylic acid hydrogel, or slightly basic for the amino-methacrylate gel. Hydrogel polymerisation was initiated by the addition of *N,N,N',N'*-tetramethylethylenediamine (TEMED) to a pre-gel solution. Potassium persulfate or ammonium persulfate were used as catalysts. Supported gels were synthesised by placing a floating piece of methacrylated silicon at the solution surface. The polymerisation reaction was allowed to take place for 20 h, after which the hydrogels were rinsed with excess water, and submerged in MilliQ for two weeks to swell and equilibrate. The hydrogels were washed, and the water was replaced three times in the swelling/equilibration period. One of the charged hydrogels was equilibrated

in 0.5 M NaCl. Switchable hydrogels were equilibrated in MilliQ at pH 4 or 10. The pH of these solutions was monitored with a calibrated pH electrode and adjusted as needed.

A sessile drop method was used to characterise static and dynamic contact angles of oil at the hydrogel/air or hydrogel/water interface. For measurements of air at the hydrogel/water interface, a captive bubble method was employed [15]. Contact angles were determined with a Krüss G10 setup. The hydrogel surface was dried under a flow of nitrogen for measurements at the hydrogel/air interface. For static and dynamic contact angle measurements under water, the silicon-supported hydrogel sample was cut from the bulk and placed in a quartz cuvette with water, or mounted upside down and submerged in water. The static contact angle was determined by deposition of a 1,8-dibromooctane (DBO) droplet under water on a hydrogel, or from an air bubble using the inverted setup. Dynamic contact angles of DBO at the hydrogel/water interfaces were measured by depositing an oil droplet at the interface. The bubble or droplet was then stepwise inflated in 1 µL increments to a volume V_{max} of 10–20 µL, and subsequently deflated again to a volume of 1 µL. A New Era NE-1000 syringe pump was used to precisely control the air or oil volume.

3.3 Results and discussion

3.3.1 Hydrogel swelling

Hydrogel swelling is a balance between the molecular and elastic forces that keep the gel together, and osmotic pressure. We quantify this swelling for a number of pAAm and pNIPAAm gels, and relate this to the crosslink density as $a/a_0 \sim C^{\alpha}$, where a/a_0 is the ratio between the observed diameter of a swollen gel and the synthesis diameter, and C the crosslink density in wt%. Results are shown in Figure 3.2. A fit of the data yields $\alpha \approx -0.1$. This weakly inverse proportionality of the swelling ratio to crosslink density is in line with expectations, as the higher crosslink density makes a stiffer, less stretchable hydrogel. Swelling of pNIPAAm-SPMA and pNIPAAm-AMA gels is only assessed qualitatively. The charged pNIPAAm-SPMA hydrogel swells significantly more in distilled water than the equivalent neutral gel. For pH-sensitive gels we observe swelling behaviour in line with expectation based on their charge: at pH $>$ pK_a, the gels are not charged and swelling is comparable to that of unmodified pNIPAAm gels. When the gel is equilibrated at pH $\ll$ pK_a, the gel swells comparable to a charged pNIPAAm-SPMA gel. Charge, whether permanent in pNIPAAm-SPMA copolymers or pH-induced in pNIPAAm-AMA copolymers, leads to significant increase in osmotic pressure inside the gel, as well as an increase of ionic repulsion, and the swelling ratio increases dramatically as a result.

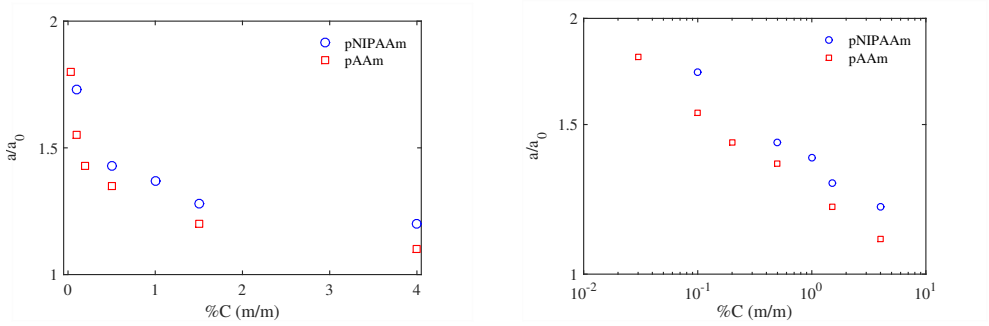

Figure 3.2 – Post-synthesis swelling of pAAm and pNIPAAm hydrogels, measured as the ratio of the observed equilibrium diameter and synthesis diameter a/a_0.

3.3.2 Static contact angle measurements

In order to measure the static contact angle of water and oil at the hydrogel-air interface, we attempt to obtain dry hydrogel surfaces by placing the gel under a flow of nitrogen. Counterintuitively, we find a finite contact angle for water, and complete wetting for oil at the hydrogel-air interface for a range of different oils, including 1,8-dibromooctane (DBO) and the highly hydrophobic Fluorinert FC-72. A possible explanation for this phenomenon is that monomers expose their hydrophobic side towards the air upon drying, effectively making the interface less hydrophilic than the bulk material. Moreover, it appears that the contact angle of water at the hydrogel/air interface depends on the dryness of the surface, and not on the hydrogel chemistry.

To remove this source of error, we submerge the hydrogel in order to measure contact angles at the hydrogel/water interface instead. We measure the static contact angle of an air bubble for a range of pAAm hydrogels, and for air and DBO at pNIPAAm hydrogels with the submerged air bubble and sessile drop method, respectively. With our setup we find a constant contact angle for both hydrogels, independent of sample composition. Results are shown in Figure 3.3a. The difference in contact angle between oil and air are likely a result of a difference in surface tension, in line with Equation 3.4. A similar experiment can be conducted with pPEGMEMA hydrogels. Here we vary the side chain mass rather than the crosslink density. This allows us to synthesise hydrogels that have the same crosslink density, but different morphologies. Results are shown in Figure 3.3b. Again we find a constant contact angle for air bubbles in water. There appears to be a slight increase in contact angle with increasing side chain mass for the oil droplet, but in either case the measured contact angles are well above the expected contact angle of 0° for complete wetting of

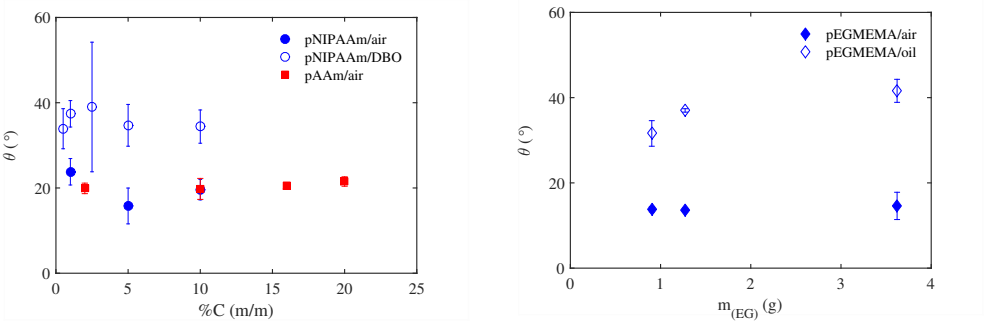

(a) (b)

Figure 3.3 – Static contact angle measurement of air bubbles or 1,8-dibromooctane droplets at the hydrogel/water interface for (a) acrylamide-type, as a function of crosslink density, and (b) poly(ethylene glycol)-type hydrogels, as a function of side chain mass. The contact angle θ is measured through the water phase. Error bars indicate the standard deviation.

the surface by water. This means that water only partially wets a hydrogel interface.

Equation 3.4 relates the surface pressure Π to the contact angle θ. In literature we find for solutions of polyacrylamide $\Pi < 10\,\mathrm{mN\,m^{-2}}$ [16, 17], for pNIPAAm $\Pi \approx 30\,\mathrm{mN\,m^{-2}}$ [16, 18, 19], and for PEG $\Pi \approx 5$–$10\,\mathrm{mN\,m^{-2}}$ [20]. Although these values are all in the same order of magnitude, pNIPAAm has a significantly higher value of Π, and therefore we expect different contact angles for these materials. However, as we do not observe a relation between the surface pressure Π and the contact angle, we conclude that the precise value of the surface pressure for the polymer solutions does not play a significant role in the determination of the static contact angle for these materials.

It is possible that polymer adsorption is limited when the polymers are crosslinked in a gel, as a result of the network structure of the gels, as opposed to free polymers or polymer brushes. A characteristic dimension here is the mesh size of the polymer gel ξ, a polymer subunit within which the polymer behaves as an ideal chain. The mesh size is related to the thermal energy and surface pressure as $\Pi \approx k_\mathrm{B}T/\xi^2$. With Equation 3.4 we can calculate Π from the contact angle. For $\theta \approx 20°$, and $\gamma_\mathrm{lg} = \gamma_\mathrm{air/water} \approx 72\,\mathrm{mN/m}$, we find $\Pi \approx 4\,\mathrm{mN/m}$. Then it follows that $\xi \approx 1\,\mathrm{nm}$. This is a reasonable length scale for a hydrogel. Since all tested gels are prepared in a similar way, we expect the mesh size to be mostly constant among the samples, which explains the constant contact angle. However, one would intuitively expect ξ, and therefore Π and θ, to depend on the crosslink density. We do not observe this

experimentally, however.

For the pPEGMEMA hydrogels we observe a small decrease in the DBO contact angle with increasing side chain mass. We speculate that this reduction is a result of stabilisation of sub-equilibrium contact angles. Relaxation of a droplet to its equilibrium contact angle requires the collective motion of the contact line and the adsorbed polymer involved. This is a slower process for longer chains. As a result, droplets adsorbed at hydrogels with longer side chains can remain longer in an out-of-equilibrium shape.

3.3.3 Dynamic contact angle measurements

Neutral gels

In the preceding section we have argued that the static contact angle of air and oil at the hydrogel/water interface is determined by polymer adsorption to the air/water or oil/water interface. We have seen that the static contact angle is likely determined by the gel's mesh size, and not by the surface pressure of the polymer. However, for a dynamic contact angle, we expect kinetics to play a role. If this is so, then the dynamic contact angle should also be affected. We measure the dynamic contact angle of DBO at the gel/water interface by inflating and subsequently deflating the oil droplet, while monitoring the contact angle. An image sequence of such an experiment is shown in Figure 3.4.

Three methods can be used to probe the contact angle hysteresis. One is to measure the difference between advancing and receding contact angle curves as a function of volume, and then take the maximum of this curve as the magnitude of hysteresis. The second is to obtain the difference between the integrals of the advancing and receding contact angle curves. A third method is to calculate the difference between the extrema of each curve. Each method has their own advantages and disadvantages. In order to accurately determine the difference between two curves, the droplet volume has to be precisely known at each point, and the measurement interval should preferably be small. Neither of these conditions is satisfactorily fulfilled in our experiments. A significant advantage of the integral method is that this evens out minor fluctuations in e.g. droplet volume. It also cancels out the effect of larger increments somewhat. However, the main drawback with this method is that the volume range needs to be constant for all experiments. As our experiments are performed with a variable maximum droplet volume, the integral method cannot be applied to most of our samples. Therefore, we use the third method and characterise hysteresis by the maximum difference between the extreme values of the advancing and receding contact angles.

First we determine if maximum droplet volume affects contact angle dynamics. For $V_{\max} \geq 10\,\mu\text{L}$ a plateau is reached for the advancing contact angle. For smaller

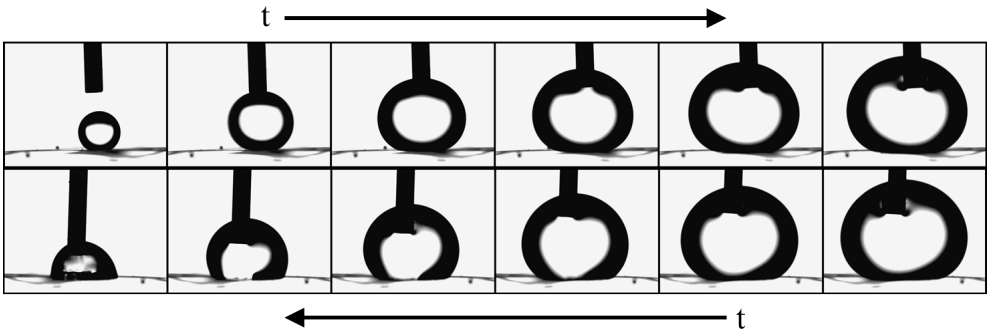

Figure 3.4 – Image series of a typical dynamic contact angle experiment. A small oil droplet at the hydrogel interface is inflated to a volume V_{max} (top image sequence) and subsequently deflated (bottom sequence). The contact angle under water is measured as a function of droplet volume.

V_{max}, we do not observe the formation of a plateau. Therefore, all experiments reported in this chapter are carried out with a maximum droplet volume of 10–21 µL. Upon deflation, we find that pNIPAAm hydrogels can stabilise out-of-equilibrium contact angles for a prolonged duration, unlike pAAm. As a result we observe a significant hysteresis for the pNIPAAm hydrogel. On the other hand, the pAAm hydrogel shows almost ideal contact angle behaviour with little or no hysteresis. Typical hysteresis curves for these two materials are shown in Figure 3.5.

To gain more insight, we test the dynamic behaviour for a range of pNIPAAm and pAAm hydrogels with varying crosslink density. For pNIPAAm we find a significant contact angle hysteresis, and there appears to be a minor increase in hysteresis with increasing crosslink density. Results are shown in Figure 3.6. Contact angle hysteresis is virtually absent for pAAm hydrogels, as was already suggested from the raw hysteresis curves shown earlier. Both effects can be explained from the chemistry of our system. In order to move a contact line, polymer chains have to desorb from the interface. The rate of desorption is low for polymers with a high interfacial affinity, such as pNIPAAm. As a result of the slow desorption of polymers from the interface, the contact line stays pinned, and hysteresis follows as a result. On the other hand, for polymers that are not or only weakly surface active, such as pAAm, the weakly bound polymer chains readily desorb from the interface, limiting the capacity of these gels to stabilise out-of-equilibrium contact angles. This process is illustrated schematically in Figure 3.7. The proportionality between crosslink density and hysteresis is also in line with expectation, as gels with a higher crosslink density have a somewhat larger contact angle hysteresis: a gel with a higher crosslink density is stronger, and we

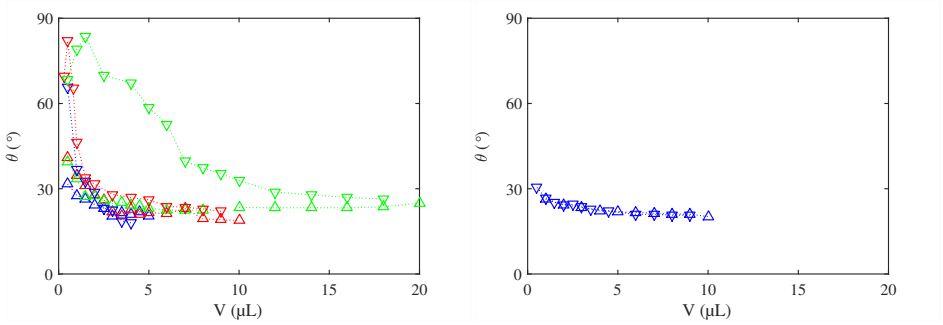

Figure 3.5 – Dynamic contact angle (DCA) measurements: (a) Typical contact angle curves for a pNIPAAm hydrogel, and (b) for a pAAm hydrogel. Symbols indicate the advancing (△) and receding (▽) contact angle.

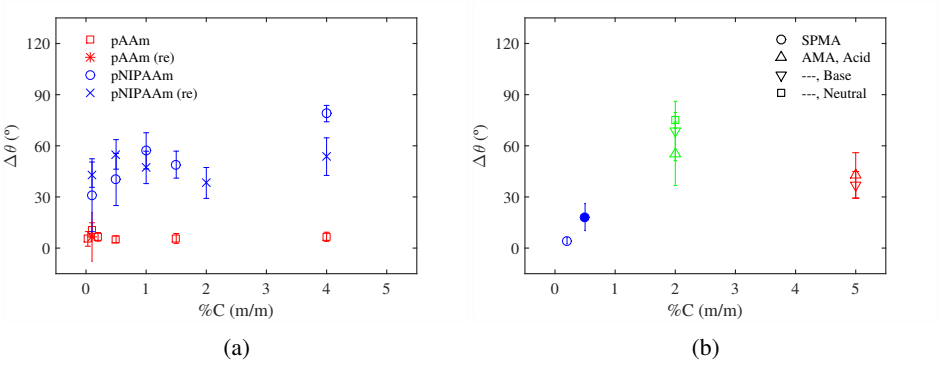

Figure 3.6 – Maximum contact angle hysteresis. (a) For pNIPAAm gels we observe significant contact angle hysteresis, which is absent for pAAm samples. Independent repeats are shown with × and ∗, respectively. (b) Charged hydrogels: for pNIPAAm-SPMA hydrogels, contact angle hysteresis is absent when measured in water (open symbol), but partially restored for a gel equilibrated in 0.5 M NaCl (filled symbol). However, all pNIPAAm-AMA hydrogels exhibit significant contact angle hysteresis, regardless of environmental conditions, and the corresponding effective charge. The 2% and 5% crosslinked samples are independent measurements. Error bars indicate the standard deviation.

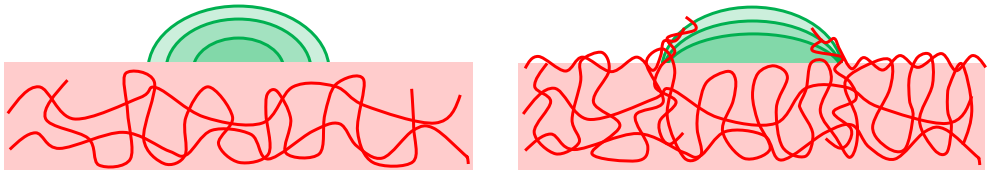

(a) (b)

Figure 3.7 – Schematic drawing of polymer adsorption as a cause for contact line pinning upon droplet deflation. (a) For polymers with a low affinity for the interface, such as pAAm, the droplet shape is determined by the surface tension alone, and the contact angle remains constant during deflation. (b) For adsorbing polymers, such as pNIPAAm, slow desorption of polymer chains from the gel-droplet interface arrests contact line motion, and we observe strong contact angle hysteresis as a result.

hypothesise that this results in slower dynamics and a lower rate of desorption, which leads to an increase in hysteresis.

Two other effects that can potentially cause contact angle hysteresis are heterogeneous wetting, as a result of surface roughness, and viscoelastic braking. Hydrogels have intrinsic surface roughness due to the nature of their synthesis; microgel particles are formed initially, and these slowly grow into a percolating network. However, since all our hydrogels are synthesized according to the same protocol, we expect a similar surface roughness for all samples. Viscoelastic braking is governed by the surface tension and elastic modulus of the hydrogel. These two variables are similar for the two gels in this experiment. This suggests that neither of these effects has a major contribution towards the significant difference in contact angle hysteresis between pNIPAAm and pAAm gels.

Charged and pH-switchable gels

We will now consider the effect of charge in a pNIPAAm network. Two systems are investigated, a hydrogel with a permanent charge (pNIPAAm copolymerised with potassium 3-sulfopropyl methacrylate, SPMA), and a hydrogel with a pH-responsive group (pNIPAAm copolymerised with 2-aminoethyl methacrylate, AMA). Surprisingly, we observe almost no hysteresis for the pNIPAAm-SPMA hydrogel when measured in distilled water, but we do observe hysteresis when the gel is equilibrated in 0.5 M NaCl. The magnitude of hysteresis is still lower than that of the uncharged network in water, but significant considering its absence in water. To our knowledge, this is the first report of salt-induced contact angle hysteresis. We can explain the phenomenon as follows: electrolytes have a low affinity for adsorption to an interface,

as their charge needs to stay hydrated. Addition of salt leads to screening of charge, and enhanced interface adsorption as a result. This adsorption leads to a subsequent partial restoration of contact angle hysteresis.

An attempt to synthesise pH-sensitive hydrogels based on a weak acid does not prove successful. First we attempt to copolymerise a pNIPAAm gel with methacrylic acid in neutral medium, but this process does not yield a gel. To prevent dissociation of methacrylic acid prior to polymerisation, we adjust the pH of the solution to be slightly acidic, as dissociation might have affected the formation of the gel. However, this procedure did not yield a gel either. A standard pNIPAAm sample prepared from the blank stock solutions carried out in neutral medium, without the addition of methacrylic acid, did yield a gel when carried out in parallel. We speculate that the radical initiator TEMED, which is a base, has been deactivated through reaction with the acid.

Subsequently we attempt to synthesise a copolymer of pNIPAAm with the weak base 2-aminoethyl methacrylate (AMA), in a slightly basic environment. With this procedure we succeed in synthesising pH-sensitive hydrogels. Literature reports a pK_a value of 8.8 for 2-aminoethyl methacrylate, or 7.6 for poly(2-aminoethyl methacrylate) [21, 22]. We expect that our pNIPAAm-AMA copolymers have a pK value in the same range. In order to obtain both charged and neutral samples, one gel sample is equilibrated in distilled water, another at pH 4 (1×10^{-4} M HCl), and a third at pH 10 (1×10^{-4} M NaOH). The comparatively mild pH-range is chosen to simultaneously keep the ionic strength of the solution low, and to protect the gels against hydrolysis in an aggressive environment. The pH is monitored and adjusted as required during the equilibration period. We observe no significant post-synthesis swelling for either the neutral or base-equilibrated pNIPAAm-AMA gel. However, the gel sample equilibrated at pH 4 shows significant swelling. From this we conclude that we managed to sucessfully synthesize a pNIPAAm-AMA copolymer, with pH-switchable characteristics.

In our experiments, however, we do not find a clear difference in hysteresis between acid- or base-equilibrated pNIPAAm-AMA hydrogels, or even plain pNIPAAm hydrogels. Results are shown in Figure 3.6b. We do find a different value for the contact angle hysteresis for pNIPAAm-AMA gels prepared with a different crosslink density, but since these values fall within or are very close to the measurement error, we believe that the difference based on crosslink density is not significant. Within each set of measurements, we find that results for acid-, base-, or neutral-equilibrated gels completely overlap. Although it seems that oil droplets adsorb less strongly to acid-equilibrated gels, we could not quantify this observation, and we do not find evidence for decreasing the contact angle hysteresis. This suggests that pH does not have a strong effect on the surface affinity of pNIPAAm-AMA gels.

Previously we explained the difference in contact angle hysteresis between acry-

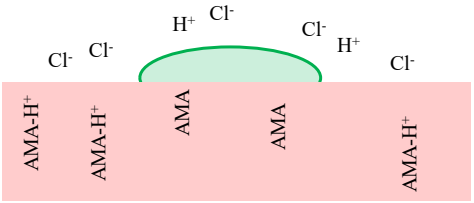

Figure 3.8 – The charge in AMA-copolymers is a result of the protonation of the weak base. We speculate that the local absence of image charges in the oil droplet leaves the amino group unprotonated, effectively rendering the hydrogel uncharged near the droplet contact line.

lamide and *N*-isopropylacrylamide gels from their affinity to the surface. We speculate that this effect also plays a role here. Although the surface pressure of a 2-aminoethyl methacrylate (co)polymer is unknown, the chemical formula is quite similar to that of *N*-isopropylacrylamide. Therefore, we assume that its effect on the net surface pressure of the pNIPAAm-AMA copolymer is less severe than that of its SPMA counterpart. Another possibility, albeit more speculative, is the occurrence of a local ion depletion layer at the interface between the water-equilibrated hydrogel and the oil droplet. The lack of a corresponding image charge in the oil droplet, due to the absence of counterions, could lead to local depletion of H^+ ions, and subsequent deprotonation of the amino group. If this is the case, the oil droplet effectively probes a neutral hydrogel in each case. This process is schematically drawn in Figure 3.8. The reason that this argument is not applicable for the SPMA copolymers is that those have a permanent charge, whereas the charge of AMA copolymers is the result of protonation of a weak base.

To validate this hypothesis, one could use a material with a high dielectric constant instead of oil, or alternatively add ions to the oil phase, for instance in the form of an ionic liquid, to compensate for the low dielectric strength. A minor, additional contribution is the ionic strength of the water phase. Because of added acid or base, the ionic strength is slightly larger than that of distilled water. However, the ionic strength is still negligible compared to that of the pNIPAAm-SPMA sample measured in 0.5 M NaCl, while the contact angle hysteresis is much more pronounced. Besides this, a sample equilibrated in distilled water has a similar hysteresis as well.

3.4 Conclusion

In this chapter we addressed three aspects of contact angle hysteresis in hydrogel wetting: the influence of polymer chemistry on the equilibrium contact angle, the

influence of polymer chemistry on contact line dynamics, and the influence of polymer architecture on contact line dynamics. This was achieved by synthesizing hydrogels from neutral and charged polymers in different mixtures. We repeatedly find a parameter-invariant static contact angle of ∼20° for air, and ∼40° for 1,8-dibromooctane at the hydrogel/water interface. From this we conclude that the surface tension of all systems is comparable. Also, since the contact angle is well above 0°, we can conclude that the corresponding water-in-air system is only partially wetting. The non-variance of equilibrium contact angle with interfacial affinity is attributed to the relative inflexibility of polymer clusters in hydrogels as compared to polymer brushes. This is in disagreement with literature predictions that wetting is determined exclusively by the affinity of the polymer to adsorb to the interface [12]. However, we do find the surface pressure Π to play a role in contact angle dynamics. We find that surface-active pNIPAAm gels can stabilise out-of-equilibrium droplets for an extended period of time, unlike pAAm hydrogels. As a result, we observe significant contact angle hysteresis on the first material but not on the latter.

The picture becomes different when charge is present. A permanently charged pNIPAAm-SPMA hydrogel shows a significant reduction, or even complete absence, of contact angle hysteresis. This hysteresis is only partially restored upon addition of salt to the water phase. To determine whether charge in itself is the most important factor here, we looked into switchable hydrogels. We successfully synthesised a pH-responsive hydrogel by copolymerisation of NIPAAm with 2-aminoethyl methacrylate, which is neutral in a basic environment, but obtains charge in an acidic environment. However, we find significant contact angle hysteresis for acid- as well as base-equilibrated gels, comparable to that of neutral pNIPAAm. This indicates that charge alone does not determine the absence or presence of contact angle hysteresis.

References

[1] A. L. Shapiro, E. Viñuela, and J. V. Maizel. Molecular weight estimation of polypeptide chains by electrophoresis in SDS-polyacrylamide gels. *Biochemical and Biophysical Research Communications*, **1967**. *28*, 815–820. doi:10.1016/0006-291X(67)90391-9.

[2] F. J. Holly and M. F. Refojo. Wettability of Hydrogels. *Journal of biomedical materials research*, **1975**. *9*, 315–326.

[3] J. Zhu. Bioactive modification of poly(ethylene glycol) hydrogels for tissue engineering. *Biomaterials*, **2010**. *31*, 4639–4656. doi:10.1016/j.biomaterials.2010.02.044.

[4] W. H. Rombouts, M. Giesbers, J. van Lent, F. A. de Wolf, and J. van der Gucht. Synergistic stiffening in double-fiber networks. *Biomacromolecules*, **2014**. *15*, 1233–1239. doi:10.1021/bm401810w.

[5] M. K. Włodarczyk-Biegun, M. W. Werten, F. A. de Wolf et al. Genetically engineered silk–collagen-like copolymer for biomedical applications: Production, characterization and evaluation of cellular response. *Acta Biomaterialia*, **2014**. *10*, 3620–3629. doi:http://dx.doi.org/10.1016/j.actbio.2014.05.006.

[6] J. K. Oh, R. Drumright, D. J. Siegwart, and K. Matyjaszewski. The development of microgels/nanogels for drug delivery applications. *Progress in Polymer Science*, **2008**. *33*, 448–477. doi:10.1016/j.progpolymsci.2008.01.002.

[7] B. Brugger, B. A. Rosen, and W. Richtering. Microgels as stimuli-responsive stabilizers for emulsions. *Langmuir*, **2008**. *24*, 12202–12208. doi:10.1021/la8015854.

[8] T. Suzuki, C. Morishita, and M. Kawaguchi. Effects of Surface Properties on Rheological and Interfacial Properties of Pickering Emulsions Prepared by Fumed Silica Suspensions Pre-Adsorbed Poly(N-Isopropylacrylamide). *Journal of Dispersion Science and Technology*, **2010**. *31*, 1479–1488. doi:10.1080/01932690903269701.

[9] H. Monteillet, M. Workamp, J. Appel, J. M. Kleijn, F. A. M. Leermakers, and J. Sprakel. Ultrastrong Anchoring Yet Barrier-Free Adsorption of Composite Microgels at Liquid Interfaces. *Advanced Materials Interfaces*, **2014**. *1*. doi:10.1002/admi.201300121.

[10] T. Kajiya, A. Daerr, T. Narita, L. Royon, F. Lequeux, and L. Limat. Dynamics of the contact line in wetting and diffusing processes of water droplets on

hydrogel (PAMPS–PAAM) substrates. *Soft Matter*, **2011**. *7*, 11425. doi: 10.1039/c1sm05944k.

[11] F. Boulogne, F. Ingremeau, L. Limat, and H. A. Stone. Tuning the Receding Contact Angle on Hydrogels by Addition of Particles. *Langmuir*, **2016**. *32*, 5573–5579. doi:10.1021/acs.langmuir.6b01209.

[12] M. A. Cohen Stuart, W. M. de Vos, and F. A. M. Leermakers. Why surfaces modified by flexible polymers often have a finite contact angle for good solvents. *Langmuir*, **2006**. *22*, 1722–1728. doi:10.1021/la052720v.

[13] A. Revzin, R. J. Russell, V. K. Yadavalli et al. Fabrication of poly (ethylene glycol) hydrogel microstructures using photolithography. *Langmuir*, **2001**. *17*, 5440–5447. doi:10.1021/la010075w.

[14] H. Tokuyama, N. Ishihara, and S. Sakohara. Effects of synthesis-solvent on swelling and elastic properties of poly(N-isopropylacrylamide) hydrogels. *European Polymer Journal*, **2007**. *43*, 4975–4982. doi:10.1016/j.eurpolymj.2007.09.016.

[15] F. J. M. Ruiz-Cabello, M. A. Rodriguez-Valverde, A. Marmur, and M. A. Cabrerizo-Vilchez. Comparison of sessile drop and captive bubble methods on rough homogeneous surfaces: A numerical study. *Langmuir*, **2011**. *27*, 9638–9643. doi:10.1021/la201248z.

[16] J. Zhang and R. Pelton. The surface tension of aqueous poly (N-isopropylacrylamide-co-acrylamide). *Journal of Polymer Science Part A: Polymer Chemistry*, **1999**. *37*, 2137–2143.

[17] M. T. Ghannam. Interfacial Properties of Polyacrylamide Solutions. *Journal of Applied Polymer Science*, **1999**. *74*, 219–227.

[18] Y. Okumura and M. Kawaguchi. Surface pressure-area isotherms and surface dilational moduli of poly (N-isopropyl acrylamide) monolayers spread at air-water interface. *Colloids and Surfaces A: Physicochemical and Engineering Aspects*, **2014**. *441*, 275–280. doi:10.1016/j.colsurfa.2013.09.015.

[19] K. Yokoi and M. Kawaguchi. Effect of temperature on surface pressure-area isotherms and surface dilational moduli of poly(N-isopropyl acrylamide) monolayers spread at air-water interface. *Colloids and Surfaces A: Physicochemical and Engineering Aspects*, **2014**. *457*, 469–475. doi:10.1016/j.colsurfa.2014.06.028.

[20] M. Winterhalter, H. Bürner, S. Marzinka, R. Benz, and J. Kasianowicz. Interaction of poly(ethylene-glycols) with air-water interfaces and lipid monolayers: investigations on surface pressure and surface potential. *Biophysical Journal*, **1995**. *69*, 1372–1381. doi:10.1016/s0006-3495(95)80006-8.

[21] L. He, E. S. Read, S. P. Armes, and D. J. Adams. Direct synthesis of controlled-structure primary amine-based methacrylic polymers by living radical polymerization. *Macromolecules*, **2007**. *40*, 4429–4438. doi:10.1021/ma070670q.

[22] K. L. Thompson, E. S. Read, and S. P. Armes. Chemical degradation of poly(2-aminoethyl methacrylate). *Polymer Degradation and Stability*, **2008**. *93*, 1460–1466. doi:10.1016/j.polymdegradstab.2008.05.013.

Part III

Colloids at anisotropically curved interfaces

Chapter 4

Colloid interactions at anisotropically curved interfaces

Abstract

Spherical colloidal particles at liquid interfaces with non-zero deviatoric curvature cause a quadrupolar deformation of the interface at the three-phase contact line. We measure the resulting capillary pair interactions as a function of interfacial curvature for microgel core-shell particles at mineral oil/water interfaces. The long-range capillary attraction is found from analysis of approach trajectories of pairs of particles. These data are complemented in the short-range from the Boltzmann statistics of bond length fluctuations to obtain the full pair potential. We show that the capillary interactions resulting from the interfacial anisotropy are strongly dependent on interfacial curvature. As a consequence of the strong interactions in quadrupolar symmetry, the self-assembly process proceeds as diffusion-limited aggregation on a square lattice.

Maarten van Heek, Joris Sprakel, and Jasper van der Gucht. Colloid interactions at anisotropically curved interfaces (in preparation)

4.1 Introduction

Small colloidal particles show great affinity for adsorption to liquid interfaces and can therefore be employed to stabilise emulsions [1] or to template low-dimensional materials with well-defined microstructures [2]. For nano- or microscopic colloids, van der Waals forces, electrostatic interactions and hard core repulsion usually dictate their 2D organisation [3, 4]. Capillary forces only come into play when the adsorbed particle locally distorts the liquid interface at the three-phase contact line. Such interfacial deformations can for example be caused by gravitational forces [5–7] or contact line pinning [8]. For isotropic particles at flat or isotropically curved interfaces these interactions are isotropic. However, anisotropic interactions may arise when the particles themselves have geometrical or chemical anisotropy [9–13].

Interestingly, anisotropic interactions may also result between isotropic colloidal spheres when they are adsorbed at a liquid interface which exhibits anisotropy in its curvature [14–16]. The requirement for an adsorbed particle in equilibrium to maintain a constant contact line is satisfied through a capillary distortion of the interface near the contact line. This deformation results in a quadrupolar deformation field around the particle, and in turn this leads to quadrupolar capillary attraction. This process is illustrated in Figure 4.1.

An appropriate method to describe curvature anisotropy is the deviatoric curvature $\mathcal{D} = |(\kappa_1 - \kappa_2)/2|$, in which κ_1 and κ_2 are the principal curvatures. Any interface with a nonzero deviatoric curvature can induce the spontaneous formation of crystalline packings of spherical particles, aligned with the two principal curvature directions. An example of this effect is shown in Figure 4.1. While previous work has shown that the phase behaviour of particles at anisotropic interfaces only depends on $\mathcal{D}$ and not on the shape of the interface, no direct measurements of the range and strength of these curvature-induced capillary interactions are available. Consequently, manipulation of the interface to tune colloidal self-assembly into desired patterns remains empirical.

We present a direct measurement of the capillary interactions between spherical colloids at cylindrically curved interfaces. For cylindrical interfaces, $\kappa_2 = 0$, hence $\mathcal{D} = \kappa_1/2 = 1/(2r_c)$. Here, r_c is the radius of curvature of the interface. We allow colloidal core-shell microgels to adsorb spontaneously to a fluid interface [17] and follow the self-assembly process that ensues with confocal microscopy. From a combination of approach trajectories of pairs of particles during binding, and the statistics of bond length fluctuations in equilibrium we construct the complete interaction potential, including both long- and short-range contributions. For equilibrium fluctuations we only consider free particle pairs, and particles at the end of a string or cluster. Particle pairs within a cluster are not analysed to avoid possible effects of multi-body interactions, which are likely non-additive. We find that the capillary interactions are strong and depend sensitively on $\mathcal{D}$. The interaction strength largely

exceeds the thermal energy $k_B T$. Combined with the quadrupolar symmetry of the interfacial deformation field, we observe that the self-assembly process occurs as diffusion-limited aggregation on a square lattice.

Literature predicts power law scaling for the interaction energy as a function of particle separation and interface curvature anisotropy [15]. The experiment discussed in this chapter shows a much weaker dependency of interaction energy on interface curvature. One significant difference between theory and our experiment is the shape of the particle at the interface. The theoretical prediction assumes a smooth sphere with a 90° contact angle. There is, however, much controversy over the shape of microgel particles at an interface. The current understanding is that these particles spread at an interface, rather than remain spherical [18]. Another subtlety is the fact that the microgel shell is, in essence, a swollen, crosslinked polymer, hence the 'classical' definition of a contact angle may not be relevant in this case. Some of these questions will be investigated in more detail in Chapter 5.

4.2 Materials and methods

Unless stated otherwise, chemicals were obtained from SigmaAldrich. Fluorescent dyes were obtained from Exciton. All chemicals were used as-received.

4.2.1 Particle synthesis

Core-shell microgels were synthesized according to a protocol adapted from literature [20]: 4 g trifluoroethylmethacrylate, 375 mg *N*-Isopropylacrylamide (TCI), 13 g water and 6 mg Nile Red were loaded in a round-bottom flask. The reaction mixture was purged with nitrogen for 10 min. Free-radical polymerisation was initiated by the addition of 10 mg potassium persulfate (KPS) and the reaction was allowed to proceed for 24 h at 65 °C. Particles were filtered and washed with water after preparation, and resuspended in DI water. To grow the microgel shell, 1 g *N*-isopropylacrylamide, 100 µl methacrylic acid, 40 mg bis(methylenebisacrylamide) and 95 g water were loaded in a round bottom flask. To this, 1 mL of a suspension of cores was added. The reaction mixture was sonicated for 2 min to disperse the cores. The reaction mixture was then heated in a water bath to 75 °C and purged with nitrogen for 10 min. Polymerisation of the hydrogel was initiated by the addition of 5 mL of a KPS solution (20 g L^{-1}). The reaction was allowed to proceed for 2 hours. After synthesis the particles were washed 3 times and resuspended in distilled water. No salt was added. The particle diameter $a = 0.9\,\mu m$ was determined with static light scattering.

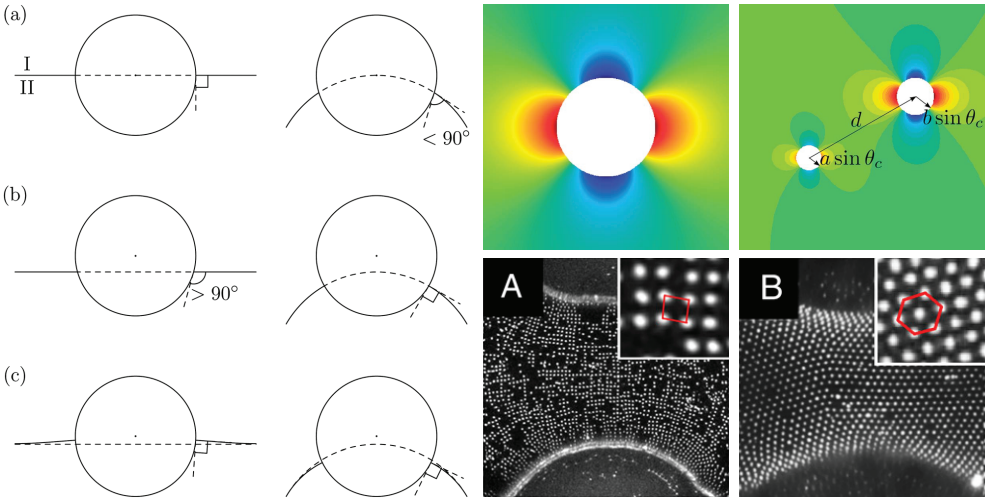

Figure 4.1 – The origin and effects of capillary deformation, as illustrated in literature. The sketch on the left shows the origin of capillary deformation caused by a spherical particle at an anisotropically curved interface: (a) A sphere at a cylindrical interface positioned with a 90° contact angle in the lateral direction has an acute contact angle along the axial direction of the cylinder. (b) Adjusting the axial contact angle to 90° leads to an obtuse lateral angle. (c) In order to keep a constant contact angle, the interface is deformed upwards in the lateral direction, and downwards in the axial direction.
The illustrations on the top right show the quadrupolar deformation field caused by one particle (left), and a superposition of two deformation fields (right). In the latter case, like deformations attract each other.
The bottom part of the image shows two confocal microscope images of colloidal particles at a dumbbell-shaped interface. At low and intermediate density, particles align to the curvature of the interface and form a square crystal (left). At high density, a transition to a hexagonal cluster is observed (right).
The illustrations at the left and top are reproduced from [19], and the microscope images at the bottom from [15].

4.2.2 Preparation of oil/water interfaces

Microscope slides with channel patterns were prepared using standard soft lithography, as described in Section 2.2.1. SU-8 25 (Microchem) was used as a photoresist. The thickness of the photoresist layer was approximately 50 µm. Channels had a width of 50–150 µm and a length of up to 5 mm.

To generate half-cylindrical oil/water interfaces, a drop of mineral oil was deposited at the edge of a channel-patterned slide. The oil was then swept off with a thin glass coverslip in the channel direction, such that all channels were filled with a thin oil layer, while leaving very little excess oil at the surface of the slide. A metal O-ring, with an internal diameter of 12 mm, was then placed over the slide, in order to contain the water phase. Microgel suspensions were prepared by diluting the stock solution with distilled water, after briefly vortexing and sonicating the stock suspension, just prior to preparation of the interface. This suspension was then pipetted in the ring on the microscope slide, and a coverslip was added on top of the metal ring to act as a sample chamber, to minimise the effect of evaporation and other environmental influences.

A complementary fluorescent dye was dissolved in the oil phase to assist in visualisation of the oil/water interface. For the red-fluorescent microgel particles we used green-fluorescent Pyrromethene 546 as the oil phase label.

The dynamic behaviour of colloid interactions was followed with confocal microscopy. For the microgel experiment we used a Zeiss Axiovert 200M microscope with a $63\times$ oil immersion objective. The scanning mirrors were set to a $0.5\times$ magnification, resulting in a field of view of approximately $200 \times 200\,\mu m^2$. The acquisition framerate was close to 1 fps.

To determine the curvature of the interface, we obtained Z stacks and fitted a circle to an (x, y)-projection of each stack. The exact procedure is explained in detail in Appendix A.

4.3 Results and discussion

4.3.1 Dimensionless numbers

In order to get a feel for the type of interaction we have to deal with, we first have a look at a few dimensionless numbers. We identify three relevant quantities: the Bond number (Bo), the Péclet number (Pe), and the particle Reynolds number (Re). We calculate these values for a system of core-shell microgel particles at oil/water interfaces.

The Bond number is a dimensionless number that compares gravity to surface

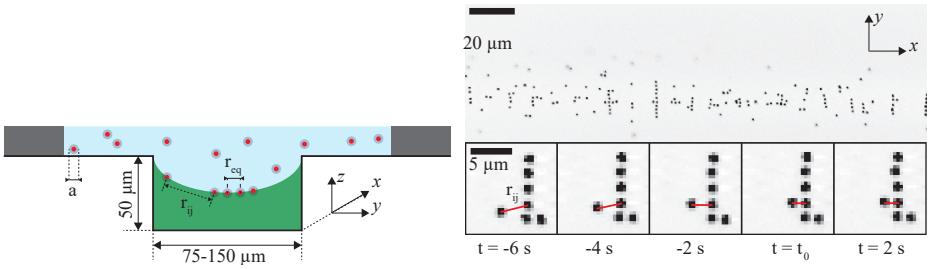

Figure 4.2 – (a) Schematic illustration of the experiment, indicating channel length x, width y, and depth z. Particles of diameter a are dispersed in the aqueous phase and spontaneously adsorb to the oil/water interface where they begin to interact. (b) Typical confocal microscopy image of a particle-covered interface at intermediate particle density. The inset shows an approach trajectory of an isolated particle attaching to an existing cluster. The drawn line indicates the Euclidean distance r_{ij} between particles that will bond; t_0 is defined as the moment the particle reaches its equilibrium position. In the last two frames the particle has attached; $\langle r_{ij} \rangle \equiv r_{eq}$.

tension forces. It is defined as

$$\mathrm{Bo} = \frac{\Delta\rho g a^2}{\gamma}, \tag{4.1}$$

with $\Delta\rho$ the difference in density between the two phases, g the gravitational constant, a a characteristic length scale, and γ the surface tension.

The next dimensionless number is the Péclet number, which measures the influence of convection relative to diffusion:

$$\mathrm{Pe} = \frac{a\mathbf{v}}{D_\mathrm{T}}. \tag{4.2}$$

The contribution of convective transport is defined by a characteristic length a, and a velocity $\mathbf{v}$. D_T is the translational diffusion coefficient.

Since we study particles at liquid-liquid interfaces, rather than in bulk, the Stokes-Einstein relation $D = kT/6\pi\eta r = \frac{k_\mathrm{B}T}{3\pi\eta a}$ may not hold. Diffusion of a particle at an interface results in Stokes streamlines in both phases, as illustrated in Figure 4.3a. As the contribution of various parameters depends on the exact composition of the interface, as well as the contact angle of the particle, an a priori determination of these values is difficult. Therefore, we determine D_T from experimental data.

The third dimensionless number, the Reynolds number, is a measure for the ratio

Table 4.1 – Particle variables and calculation of dimensionless numbers

	Microgel	Unit
ρ (oil)	0.8×10^{3}	$\mathrm{kg\,m^{-3}}$
ρ (particle)	1×10^{3}	$\mathrm{kg\,m^{-3}}$
$\Delta\rho$	0.2×10^{3}	$\mathrm{kg\,m^{-3}}$
a (particle diameter)	0.9×10^{-6}	m
$\mathbf{v}$ (terminal approach velocity)	0.5×10^{-6}	$\mathrm{m\,s^{-1}}$
D_T	0.02×10^{-12}	$\mathrm{m^2\,s^{-1}}$
η (water)	1×10^{-3}	$\mathrm{N\,m^{-2}\,s}$
g	9.81	$\mathrm{m\,s^{-2}}$
γ (oil/water)	40×10^{-3}	$\mathrm{N\,m^{-1}}$
E	2×10^{4}	$\mathrm{N\,m^{-2}}$
Bo	4.04×10^{-8}	
Pe	2.27×10^{-1}	
Re	3.63×10^{-7}	
L_ec	2×10^{-6}	m

between inertia and viscous forces. It is defined as

$$\mathrm{Re} = \frac{\rho \mathbf{v} a}{\eta}, \tag{4.3}$$

where we find the fluid density ρ, the local flow velocity $\mathbf{v}$, and a characteristic length a in the numerator, and the dynamic viscosity η of the liquid in the denominator.

Besides these dimensionless numbers, we estimate the elastocapillary length L_ec. This is a measure of the deformation of a particle under the influence of surface tension, an effect that is ignored by Young's law. The elastocapillary length is defined as

$$L_\mathrm{ec} = \frac{\gamma}{E}, \tag{4.4}$$

where γ is the surface tension of the liquid, and E is the Young's modulus of the particle. For soft particles a significant deformation is expected [21, 22]. This effect is schematically drawn in Figure 4.3b.

Table 4.1 lists a number of experimentally determined quantities or reference values for the variables defined in Equations 4.1–4.4. We use the particle diameter a as an approximation for the characteristic length, and the terminal approach velocity $\mathbf{v}$ of pairs for both the flow velocity in Equation 4.2 and the particle velocity in Equation 4.3. Both the Bond number and the Reynolds number are $\ll 1$ with these input

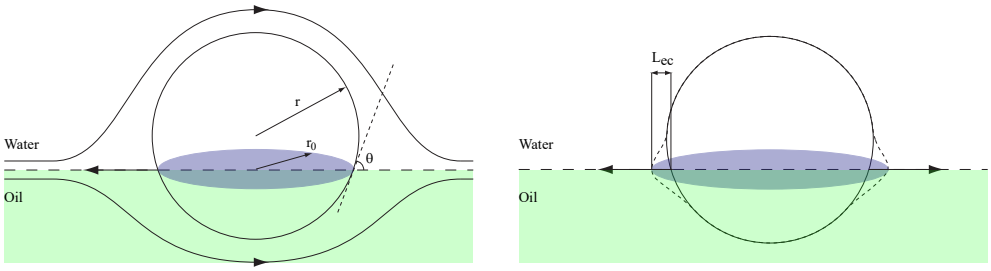

Figure 4.3 – Illustration of a particle at an oil/water interface. (a) A particle with radius r and a contact angle θ has an effective contact area with a radius r_0. Particle motion (in this example, to the left) will generate Stokes flow lines in both liquid phases. (b) Soft particles may deform under influence of the surface tension. The elastocapillary length L_{ec} is indicated as the difference between the original particle size and the stretched particle, schematically indicated with a dashed line.

parameters. This shows that surface tension and viscous forces indeed dominate particle interactions.

For the Péclet number, the picture is slightly different. We find Pe $\sim 10^{-1}$. As we calculate the Péclet number from the terminal approach velocity, this is the upper bound of the range, and its value is significantly lower for most of the duration of the experiment. This indicates that particle movement is significantly affected by diffusion, although diffusion does not dominate the interaction. Because of this, thermal noise is significant in our experiment. As a result, averaging of multiple approach trajectories is necessary to obtain a fair estimate of the particle interaction energy U. Furthermore, we observe that the elastocapillary length is significant for microgel particles, with a value in the same order of magnitude as the particle diameter. As the elastocapillary length is calculated for bulk gel samples, and the particles discussed here have a solid core, the actual deformation is expected to be lower, but still significant.

4.3.2 Pair interactions: Microgels

At the start of the experiment we attempt to focus the microscope near the oil/water interface, as indicated by the fluorescent label in the oil phase. During the initial stage of particle adsorption, isolated particles appear in the field of view. Particles diffuse randomly, until they diffuse into the interaction range of other particles or existing clusters; at this point, the particles approach each other rapidly. The moment at which two particles come into contact, or when a particle is attached to an existing

cluster, is defined as t_0. As a result of the quadrupolar deformation of the interface by the particle [15], particles align on a square lattice. A typical confocal image of a particle-laden interface is shown in Figure 4.2b; the inset shows a magnified view of a particle diffusing into contact with an existing cluster.

Since the experiment operates in a low Reynolds number regime, it is safe to assume that Stokes drag is the main force acting on these particles. The net force acting on these particles can then be determined as $F = \xi \cdot v$, where ξ is the Stokes friction coefficient of the particle at the interface.

To determine ξ we measure the mean-squared displacement $\langle \Delta r^2 \rangle$ (MSD) [23] of isolated particles at these interfaces, shown in Figure 4.4a. Here we only consider diffusion in the x-direction, for which curvature effects are minimal. Our data is robust to this choice; the two-dimensional MSD of these particles at a flat interface yields the same result. From this MSD analysis we can determine the translational diffusion coefficient D_T, which is found to be independent of interfacial curvature (inset Figure 4.4a). The diffusion coefficient we determine for particles at interfaces is approximately an order of magnitude smaller than that for the same particles in pure water. This is caused by the much higher viscosity of the oil phase in which the particles are partially immersed when anchored to the interface. From the average translational diffusion coefficient of $0.022\,\mu\mathrm{m}^2\,\mathrm{s}^{-1}$, we then find, using the Einstein relation $D_\mathrm{T} = k_\mathrm{B}T/\xi$, that $\xi = 1.8 \times 10^{-7}\,\mathrm{N\,s\,m}^{-1}$.

Approach events are analysed by computing the Euclidean distance r_ij between approaching particle pairs, from the coordinates that are obtained from standard particle tracking algorithms with a resolution of approximately 20 nm [24]. Individual approach events, as shown by the particle separation r_ij vs. time, centered at t_0, contain significant noise. This thermal noise can be reduced by averaging multiple approach events between different pairs of particles. As interface curvature is not a control parameter, we have to determine the radius of curvature r_c of each interface individually, and then calculate the deviatoric curvature $\mathcal{D}$. To obtain sufficient statistics, data is binned for interfaces with strong ($\mathcal{D} > 1/300\,\mu\mathrm{m}^{-1}$), medium ($1/300 \geq \mathcal{D} > 1/1200\,\mu\mathrm{m}^{-1}$), and low curvature anisotropy ($\mathcal{D} \leq 1/1200\,\mu\mathrm{m}^{-1}$). Below we will show that our results are robust to the choice of these limits. Average approach curves are shown in Figure 4.4b, together with the raw data of interfaces with strong curvature anisotropy. It is clear from this graph that particles do not interact at long distance, but near t_0 we find that approach curves start to overlap, resulting in relatively smooth average approach curves.

We now derive the approach velocity $v = dr_\mathrm{ij}/dt$ for each ensemble of curves at $t \leq t_0$ from the approach curves. Knowing ξ, the attractive forces acting on the pair of particles can be computed directly from the velocity. The force fluctuates around zero at large separation ($r_\mathrm{ij} \gg 6\,\mu\mathrm{m}$), and increases steeply with decreasing separation. These force curves are shown in Figure 4.4c. For flat interfaces, capillary interactions

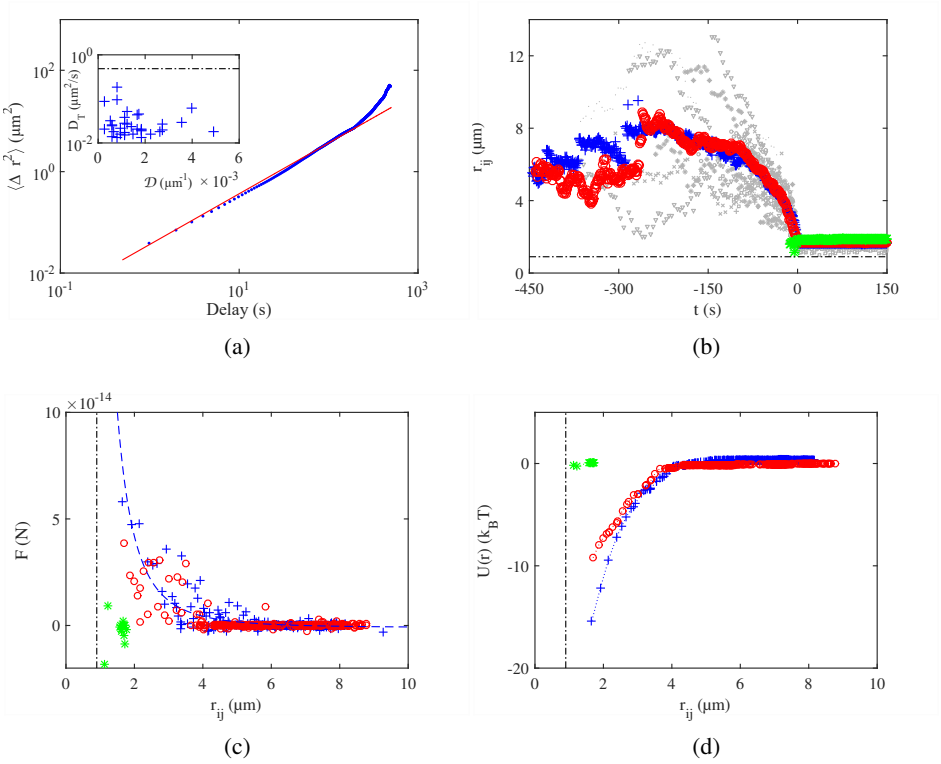

Figure 4.4 – Analysis of the long-range interaction between microgel particles at a mineral oil/water interface. (a) Average MSD curve (blue dots) of an ensemble of 64 free particles at a particular interface. The red line is a linear fit to the first quarter of data points. The deviation of the curvature at a delay $\geq 1 \times 10^2$ s is an artefact as a result of particle drift. Inset: the diffusion coefficient D_T is independent of interface curvature $\mathcal{D}$; the dash-dotted line shows the approximate diffusion coefficient in water. (b) Average particle approach curves ($t \leq t_0$), and part of equilibrium curves ($t > t_0$). Raw data for interfaces with strong anisotropy is shown in smaller, grey symbols. For clarity, only 20 % of data points are shown.
(c) Inter-particle force curves, calculated from the velocity profile of the corresponding approach curves. The dashed line is shown as a guide to the eye.
(d) Approach energy curves, obtained by integrating the force curves. In (b)–(d), data is grouped by curvature anisotropy: + strong, ○ medium, or * low anisotropy. The particle diameter is indicated by a dash-dotted line.

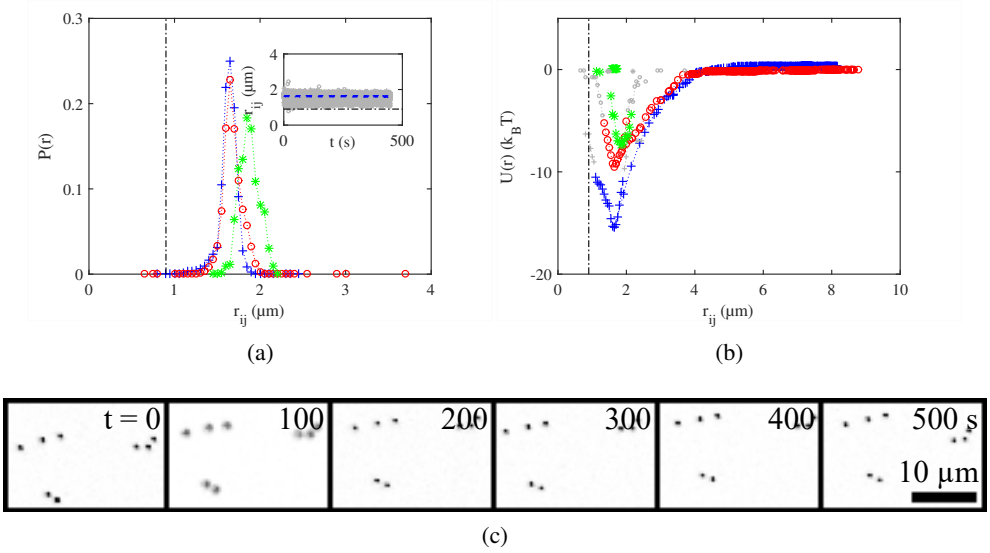

Figure 4.5 – Equilibrium analysis. (a) Probability distribution of the equilibrium distance, plotted for interfaces with strong, medium, and low curvature anisotropy. The inset shows raw data (grey symbols) and the average particle separation $\langle r_{ij} \rangle$ (dashed line) for particles at strongly anisotropic interfaces. (b) Overlay of potential energy curves from the long-range and the equilibrium analysis; less reliable data ($U/k_BT > 5$) is indicated with smaller, grey symbols. The dash-dotted line represents the particle diameter. (c) Time sequence showing an example of an anomalous particle equilibrium distance, found at an interface with low curvature anisotropy. Most particle pairs are found at an average distance r_{eq}, but the string in upper left corner has stable separation $r_{ij} \gg r_{eq}$.

should vanish; indeed we did not find a significant number of approach events for these experiments. The pair interaction potential $U(r)$ is then found by integration over $F dr_{ij}$. W find that the long-range interactions become stronger and longer ranged when the anisotropy in interfacial curvature is increased, as predicted by theory. A plot of potential energy as a function of separation is shown in Figure 4.4d. The interaction is stronger on surfaces with stronger anisotropy.

In our experiments, we rarely see a particle escape from a cluster or string. Already at separations as large as ~ 4 times the particle diameter, the interaction energy exceeds the thermal energy k_BT, making it virtually impossible for particles to escape once contact is established. Once bonded, pairs of particles fluctuate around their equilibrium position, characterised by an equilibrium distance $r_{eq} = \langle r_{ij} \rangle$. The

inset in Figure 4.5a shows that the average particle separation does not change over time, which indicates that our particles are indeed in equilibrium. Consequently, these bond-length fluctuations must obey Boltzmann statistics, so that the local potential energy in the short-range can be measured as $U(r) = -k_B T \ln P(r_{ij}) + c^*$. Here c^* is a constant, which sets the absolute depth of the potential energy minimum.

For the analysis of the interaction energy in equilibrium we look at the equilibrium vibrations of particle pairs. We also include particle pairs at the end of a string in our analysis. Since interactions may not be pairwise additive, we do not include particles within a string or cluster in this analysis. We calculate the probability distribution of bond lengths $P(r_{ij})$ in the range $0 < r_{ij} \leq 4\,\mu m$, with a bin size of $0.05\,\mu m$ (Figure 4.5a). The probability distribution is steepest for interfaces with a high deviatoric curvature, again confirming that the strength of attractive bonds increases with $\mathcal{D}$. The bond length distributions are not symmetric; fluctuations $r_{ij} < r_{eq}$ are governed by the repulsive interactions between bonded neighbours while fluctuations to larger separations $r_{ij} > r_{eq}$ mostly probe the local curvature of the attractive interactions due to capillary effects. From $P(r_{ij})$ we can determine the shape of the local potential energy minimum, as $\ln P(r_{ij})$. Reliable statistics from this thermal equilibrium analysis are only obtained for small values of $U/k_B T$, we therefore plot data for $U/k_B T > 5$ in grey. In absence of a reference point, analysis of Boltzmann statistics only yield the shape of the local energy, but not the absolute energy scale. We thus superpose the long-range attractive energy, obtained from approach events, with the local energy curvature obtained as $\ln P(r_{ij})$ by matching the values at r_{eq}. This yields the full pair interaction potential between particles at interfaces with different curvatures (Figure 4.5b). Note that for the weakly curved interfaces, insufficient approach events were observed to construct the long-range potential energy curve. As a result, the superposition with $U(r_{ij})$ from the bond length analysis is not possible. For comparison we included this data by vertical shifting such that $U_{max} = 0$.

The soft repulsive interactions between the particles are most likely a combination of electrostatic and elastic contributions. If we assume that these interactions are independent of curvature, an increase in steepness of the capillary attraction with $\mathcal{D}$ must lead to shorter equilibrium distances. Indeed we find that the pair potentials show a clear dependence on $\mathcal{D}$ with a pronounced minimum at r_{eq}, which shifts to lower pair separations with increasing anisotropy of the interface (Figure 4.6a). Concomitantly, this minimum increases in depth U_{min} with increasing deviatoric curvature (Figure 4.6b). Clearly, the strength of the capillary attraction can be tailored by adjusting the shape of the interface, from just exceeding the thermal energy to situations where it is sufficiently strong to render thermally-activated detachment negligible.

It was mentioned earlier that our data analysis is robust with regards to the choice

of limits of $\mathcal{D}$. We repeated the above analysis with 5 bins. As limits we chose $\mathcal{D} = 1/150, 1/300, 1/600, 1/1200$ and $1/1800\,\mu\text{m}^{-1}$. Effectively this interpolates the results from the described 3-bin approach. Indeed, results from this analysis follow the same trend as the three-bin analysis, as is clear from Figure 4.6.

Recently, we performed numerical calculations for solid particles at a curved interface, which showed that the capillary interaction scales as $U_{\text{cap}} \sim \gamma \mathcal{D}^2 a_0^4 (r/a_0)^{-6}$, with γ the interfacial tension and $a_0 = a \sin\theta$ the effective radius of the particle at the interface [15], θ being the equilibrium contact angle (see the schematic drawing in Figure 4.3a). Together with a short-range repulsive contribution, arising from steric or electrostatic interactions, this indeed predicts a finite equilibrium separation that decreases with increasing $\mathcal{D}$. However, for any form of the repulsion that decreases monotonically with r, the depth of the energy minimum increases at least quadratically with $\mathcal{D}$. In our experiments we find a much weaker dependence on $\mathcal{D}$. This indicates that the situation is more complex for our microgel particles than for solid particles with a fixed three-phase contact line. For soft particles, such as the microgel particles in our experiment, the interfacial deformation is significant, as depicted in Figure 4.3b. The elastocapillary length is estimated to be $\sim 100\,\text{nm}$, which is the same order of magnitude as the original particle diameter. It is possible that the deformation of the particles at the interface modifies the curvature dependence of the capillary interaction. Besides this, theory only considers equilibration of particle pairs. Our analysis also includes particle pairs at the end of clusters. It is likely that these particles experience attractive and repulsive contributions from nearby particles. These multipole moments are neglected in our analysis, although they will have a finite effect on the interaction potential.

An indication of the potential subtle complexities of the pair potential which our current analysis does not reveal is indicated by the fact that in some experiments we observe stable strings of particles in which the separation distance is much larger than r_{eq} found for most particle pairs (see Figure 4.5c). This only occurs for samples at (nearly) flat interfaces; careful analysis of these pairs with both brightfield and confocal microscopy reveals that there is no additional particle or impurity separating these bonded colloids. This may indicate the presence of a weak secondary minimum in the pair potential due to the combined effects of particle deformation [21, 22], and resulting anomalous elastic interactions [25], electrostatic interactions, which can be surprisingly heterogeneous at liquid interfaces [26], and long-ranged capillary interactions.

4.3.3 Fractal structures

The bond strength between pairs of particles we measure here well exceeds the thermal energy. While ordered structures, such as square and hexagonal crystals [15]

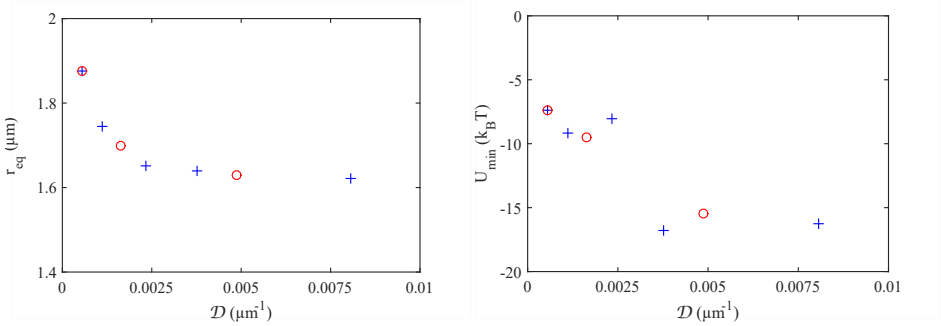

(a) (b)

Figure 4.6 – (a) Equilibrium distance, and (b) Potential energy minimum for spherical colloids at anisotropically curved interfaces as a function of deviatoric curvature $\mathcal{D}$. Analysis with + 5 bins or ○ 3 bins.

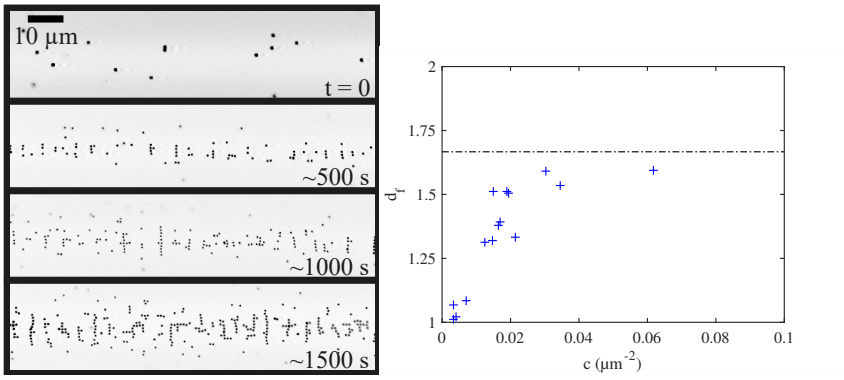

(a) (b)

Figure 4.7 – (a) Time series of particle assembly at an interface. Initially we find single particles, which group in string-like structures and ultimately more branched fractals. (b) The fractal dimension d_f as a function of surface packing density c for particles at interfaces with $\mathcal{D} > 1/600\,\mu m^{-1}$. The dash-dotted line shows the theoretical prediction of 5/3 for aggregation on a square lattice.

can be formed at anisotropic interfaces at high packing densities, the high bonding energy suggests that capillary interactions mediate structure formation through a non-equilibrium process such as diffusion-limited aggregation, rather than through nucleation and growth as expected for equilibrium crystals. At low densities, the structures that form are indeed tenuous fractal objects rather then dense crystallites (Figure 4.2b and 4.7a), which, due to the quadrupolar nature of the interfacial deformations, take the shape of 'lattice animals' on a square lattice. For diffusion-limited aggregation on a two-dimensional square lattice a characteristic fractal dimension $d_f = 5/3$ is predicted [27]. We measure the fractal dimension d_f of the self-assembled structures at the interface as a function of surface density of particles. At low packing fractions, the particles form string-like objects with $d_f \approx 1$. As the concentration is increased the strings begin to branch until a percolated network structure forms, which approaches the predicted fractal dimension, as shown in Figure 4.7b. If the packing fraction is increased much more, we expect the formation of a square crystal, and potentially a hexagonal crystal at even higher number densities, as described in literature [15].

4.4 Conclusion

Our results illustrate how both long- and short-range interactions between small colloidal particles at liquid interfaces can be experimentally determined to construct their full pair interaction potentials. For particles at anisotropically curved interfaces we observe anisotropic interactions mediated by quadrupolar interfacial deformations, the strength of which depends strongly on the deviatoric curvature $\mathcal{D}$ of the interface. The high equilibrium bond strength between pairs of particles at strongly curved interfaces, combined with their quadrupolar symmetry, leads to the formation of fractal structures which obey the statistics for diffusion-limited aggregation on a square lattice. The results presented here only consider the interactions between free particle pairs and pairs at the end of strings, but not pairs within a cluster where interactions can be affected by the presence of multiple additional neighbours. The local interfacial deformations which cause the capillary attractions are non-additive by nature. Future work is aimed at elucidating many-body effects in capillary self-assembly to obtain a full understanding of the driving forces behind the formation of low-dimensional structures at liquid interfaces. Moreover, the results presented here indicate that the softness of and charge on the particles may generate a subtle and complex interaction potential, with possible secondary minima. While additional study is needed to clarify the effects of particle softness on capillary self-assembly, the interplay of interfacial curvature, electrostatic repulsions and particle deformability may offer a means to create complex interactions in simple systems to create yet unrealised self-assembled structures [28].

References

[1] A. D. Dinsmore, M. F. Hsu, M. G. Nikolaides, M. Marquez, A. R. Bausch, and D. A. Weitz. Colloidosomes: selectively permeable capsules composed of colloidal particles. *Science (New York, N.Y.)*, **2002**. *298*, 1006–1009. doi: 10.1126/science.1074868.

[2] M. P. Boneschanscher, W. H. Evers, J. J. Geuchies et al. Long-range orientation and atomic attachment of nanocrystals in 2D honeycomb superlattices. *Science (New York, N.Y.)*, **2014**. *344*, 1377–80. doi:10.1126/science.1252642.

[3] J. Ruiz-Garcia, R. Gamez-Corrales, and B. I. Ivlev. Foam and cluster structure formation by latex particles at the air/water interface. *Physica A*, **1997**. *236*, 97–104. doi:10.1016/S0378-4371(96)00399-8.

[4] M. G. Nikolaides, A. R. Bausch, M. F. Hsu et al. Electric-Field-Induced Capillary Attraction between Like-Charged Particles at Liquid Interfaces. *Nature*, **2002**. *420*, 299—-301.

[5] D. Vella and L. Mahadevan. The 'Cheerios effect'. *American Journal of Physics*, **2004**. *02138*, 10. doi:10.1119/1.1898523.

[6] M. P. Boneva, K. D. Danov, N. C. Christov, and P. A. Kralchevsky. Attraction between particles at a liquid interface due to the interplay of gravity- And electric-field-induced interfacial deformations. *Langmuir*, **2009**. *25*, 9129–9139. doi:10.1021/la9006873.

[7] J. Bleibel, A. Domínguez, and M. Oettel. Colloidal particles at fluid interfaces: Effective interactions, dynamics and a gravitation-like instability. *European Physical Journal: Special Topics*, **2013**. *222*, 3071–3087. doi:10.1140/epjst/e2013-02076-9.

[8] D. Stamou, C. Duschl, and D. Johannsmann. Long-range attraction between colloidal spheres at the air-water interface: The consequence of an irregular meniscus. *Physical Review E - Statistical Physics, Plasmas, Fluids, and Related Interdisciplinary Topics*, **2000**. *62*, 5263–5272. doi:10.1103/PhysRevE.62.5263.

[9] E. P. Lewandowski, M. Cavallaro, L. Botto, J. C. Bernate, V. Garbin, and K. J. Stebe. Orientation and self-assembly of cylindrical particles by anisotropic capillary interactions. *Langmuir*, **2010**. *26*, 15142–15154. doi:10.1021/la1012632.

[10] M. Cavallaro, L. Botto, E. P. Lewandowski, M. Wang, and K. J. Stebe. Curvature-driven capillary migration and assembly of rod-like particles. *Proceedings of the National Academy of Sciences*, **2011**. *108*, 20923–20928. doi:10.1073/pnas.1116344108.

[11] L. Botto, L. Yao, R. L. Leheny, and K. J. Stebe. Capillary bond between rod-like particles and the micromechanics of particle-laden interfaces. *Soft Matter*, **2012**. *8*, 4971. doi:10.1039/c2sm25211b.

[12] S. Dasgupta, M. Katava, M. Faraj, T. Auth, and G. Gompper. Capillary assembly of microscale ellipsoidal, cuboidal, and spherical particles at interfaces. *Langmuir : the ACS journal of surfaces and colloids*, **2014**. *30*, 11873–82. doi:10.1021/la502627h.

[13] G. B. Davies, T. Krüger, P. V. Coveney, J. Harting, and F. Bresme. Assembling ellipsoidal particles at fluid interfaces using switchable dipolar capillary interactions. *Advanced Materials*, **2014**. *26*, 6715–9. doi:10.1002/adma.201402419.

[14] C. Zeng, F. Brau, B. Davidovitch, and A. D. Dinsmore. Capillary interactions among spherical particles at curved liquid interfaces. *Soft Matter*, **2012**. *8*, 8582. doi:10.1039/c2sm25871d.

[15] D. Ershov, J. Sprakel, J. Appel, M. A. Cohen Stuart, and J. van der Gucht. Capillarity-induced ordering of spherical colloids on an interface with anisotropic curvature. *Proceedings of the National Academy of Sciences of the United States of America*, **2013**. *110*, 9220–4. doi:10.1073/pnas.1222196110.

[16] A. Würger. Curvature-induced capillary interaction of spherical particles at a liquid interface. *Physical Review E - Statistical, Nonlinear, and Soft Matter Physics*, **2006**. *74*, 041402. doi:10.1103/PhysRevE.74.041402.

[17] H. Monteillet, M. Workamp, J. Appel, J. M. Kleijn, F. A. M. Leermakers, and J. Sprakel. Ultrastrong Anchoring Yet Barrier-Free Adsorption of Composite Microgels at Liquid Interfaces. *Advanced Materials Interfaces*, **2014**. *1*. doi:10.1002/admi.201300121.

[18] Z. Li, K. Geisel, W. Richtering, and T. Ngai. Poly(N-isopropylacrylamide) microgels at the oil–water interface: adsorption kinetics. *Soft Matter*, **2013**. *9*, 9939. doi:10.1039/c3sm52168k.

[19] C. Zheng, F. Brau, B. Davidovitch, and A. D. Dinsmore. Capillary interactions among spherical particles at curved liquid interfaces. *Soft Matter*, **2012**. pp. 8582–8594.

[20] J. Appel, N. de Lange, H. van der Kooij et al. Temperature controlled sequential gelation in composite microgel suspensions. *Particle and Particle Systems Characterization*, **2015**.

[21] O. S. Deshmukh, D. van den Ende, M. A. Cohen Stuart, F. Mugele, and M. H. G. G. Duits. Hard and soft colloids at fluid interfaces: Adsorption, interactions, assembly & rheology. *Advances in Colloid and Interface Science*, **2014**. *222*, 215–227. doi:10.1016/j.cis.2014.09.003.

[22] R. W. Style, L. Isa, and E. R. Dufresne. Adsorption of soft particles at fluid interfaces. *Soft Matter*, **2015**. *11*, 1–8. doi:10.1039/C5SM01743B.

[23] N. Tarantino, J. Y. Tinevez, E. F. Crowell et al. TNF and IL-1 exhibit distinct ubiquitin requirements for inducing NEMO-IKK supramolecular structures. *Journal of Cell Biology*, **2014**. *204*, 231–245. doi:10.1083/jcb.201307172.

[24] V. Pelletier, N. Gal, P. Fournier, and M. L. Kilfoil. Microrheology of microtubule solutions and actin-microtubule composite networks. *Physical Review Letters*, **2009**. *102*, 188303. doi:10.1103/PhysRevLett.102.188303.

[25] K. Geisel, L. Isa, and W. Richtering. Unraveling the 3D localization and deformation of responsive microgels at oil/water interfaces: A step forward in understanding soft emulsion stabilizers. *Langmuir*, **2012**. *28*, 15770–15776. doi:10.1021/la302974j.

[26] B. J. Park, J. Vermant, and E. M. Furst. Heterogeneity of the electrostatic repulsion between colloids at the oil–water interface. *Soft Matter*, **2010**. *6*, 5327. doi:10.1039/c0sm00485e.

[27] T. A. Witten and L. M. Sander. Diffusion-limited aggregation, a kinetic critical phenomenon. *Physical Review Letters*, **1981**. *47*, 1400–1403. doi:10.1103/PhysRevLett.47.1400.

[28] S. Torquato. Inverse Optimization Techniques for Targeted Self-Assembly. *Soft Matter*, **2009**. *5*, 1157–1173. doi:10.1039/b814211b.

Chapter 5

Anisotropic interfaces: a foolproof pathway to anisotropic particle interactions?

Abstract

Previous experiments suggest a correlation between the deviatoric curvature of an interface, and the strength of capillary interactions between particles adsorbed to that interface, but fall short to reproduce theoretical predictions. In this chapter we attempt to replicate the experiment, using a potentially more straightforward approach with solid spherical colloids, which lack the deformability of the microgels used previously. However, we find an unforeseen short range and low strength of capillary interactions. A bond angle analysis shows that interactions depend only weakly on the deviatoric curvature of the interface, and are significantly influenced by the chemical composition of the oil phase.

5.1 Introduction

In Chapter 4 we discussed the spontaneous adsorption and the subsequent organisation of microgel colloids at anisotropically curved oil/water interfaces. Although we found the range and strength of interaction to correlate with the deviatoric curvature of the interface, this dependence is not as strong as predicted by calculations. As discussed, a possible origin for this deviation is the deformability of the microgels used in those studies. To explore the robustness of the findings, and to eliminate interfacial deformation of the colloids, we study a system of rigid spherical colloids at liquid interfaces.

One of the questions with the previous experiment is the shape of the contact line. Theory assumes a rigid particle and an arbitrary contact angle, but calculations were only performed for a model system with a contact angle of 90°. As the current view in literature is that microgel particles deform at an interface [1, 2], the experimental system does not reflect the theoretical assumptions. Even if the particle were not to spread at the interface, its low elastic modulus gives rise to a significant elastocapillary length. Besides these considerations about particle rigidity, the concept of a 'contact angle' is questionable for a particle that consists mostly of solvent.

The aim of the research described in this chapter is to verify theoretical predictions, and to test the hypothesis that any system of colloidal particles at anisotropically curved interfaces will exhibit anisotropic interactions, the range and strength of which are determined by the deviatoric curvature of the interface.

In order to address the problem, we define three requirements for a modified experimental system: the particles to be used should have a high elastic modulus, in order to neglect elastocapillary effects; a fluorescent core, in order to facilitate particle visualisation and tracking by confocal microscopy; and adsorb spontaneously to oil/water interfaces, such that additional force is not needed to drive the particles to the interface, which could potentially disturb the fragile oil/water interface in our microchannels.

Silica particles appear to be a suitable candidate. Their high elastic modulus of about 1×10^2 GPa practically eliminates any elastocapillary deformation, and they can be labelled with a fluorescent dye. The reason why these particles were not used in earlier experiments is that unmodified, clean silica particles do not adsorb spontaneously to liquid interfaces, as they are completely wetted by water. However, recent research in our group indicated that spontaneous adsorption of silica particles to oil/water interfaces is possible if an ionic liquid is present in the oil phase [3]. It is speculated that this is a result of coacervation of the positively charged group of the ionic liquid with the negative surface charge acquired by the silica particles in water. This process is illustrated in Figure 5.1.

In this chapter we investigate the organisation of silica spheres with a fluorescent

Table 5.1 – Comparison of dimensionless numbers calculated for a system consisting of microgel colloids vs. silica colloids

	Microgel	Silica	Unit
ρ (oil)	0.8×10^{3}	1.48×10^{3}	$\mathrm{kg\,m^{-3}}$
ρ (particle)	1×10^{3}	2.65×10^{3}	$\mathrm{kg\,m^{-3}}$
$\Delta\rho$	0.2×10^{3}	1.73×10^{3}	$\mathrm{kg\,m^{-3}}$
a (particle diameter)	0.9×10^{-6}	0.7×10^{-6}	m
$\mathbf{v}$ (terminal approach velocity)	0.5×10^{-6}	1.5×10^{-6}	$\mathrm{m\,s^{-1}}$
D_{T}[a]	0.02×10^{-12}	0.4×10^{-12}	$\mathrm{m^2\,s^{-1}}$
η (water)	1×10^{-3}	1×10^{-3}	$\mathrm{N\,m^{-2}\,s}$
g	9.81	9.81	$\mathrm{m\,s^{-2}}$
γ (oil/water)	40×10^{-3}	25×10^{-3}	$\mathrm{N\,m^{-1}}$
E	2×10^{4}	1×10^{11}	$\mathrm{N\,m^{-2}}$
Bo	4.04×10^{-8}	2.37×10^{-7}	
Pe	2.27×10^{-1}	2.69×10^{0}	
Re	3.63×10^{-7}	1.59×10^{-6}	
L_{ec}	2×10^{-6}	2.5×10^{-13}	m

a. Average (microgel) or maximum calculated value (silica)

silica core at anisotropically curved 1,8-dibromooctane/water or bromobenzene/water interfaces, in presence of a small amount of ionic liquid in the oil phase. We find that silica particles adsorb spontaneously to these interfaces, and organise in a square pattern, as with the previous experiments. However, we find that the range and strength of interaction for these particles is drastically smaller than for the microgel system described in Chapter 4. Thermal fluctuations dominate a large part of the interaction. Due to the shorter range and lower strength, particles seem to organise in denser clusters as compared to the rather fractal structures observed with the microgel experiments. This shows that colloid physics, even for comparatively easy models, still offer a large, undisclosed area of intricate interactions.

5.2 Materials and methods

Core-shell silica particles were prepared following established protocols [4]. Briefly: green-fluorescent cores were prepared in a batchwise Stöber synthesis in which the adduct of aminopropyl triethoxysilane and fluorescein isothiocyanate was used to covalently label the particles. Core particles with a diameter of 0.4 µm were subsequently coated by a nonfluorescent shell by the dropwise addition of additional tetraethyl orthosilicate untill a shell of 0.16 µm was formed. Silica particles were

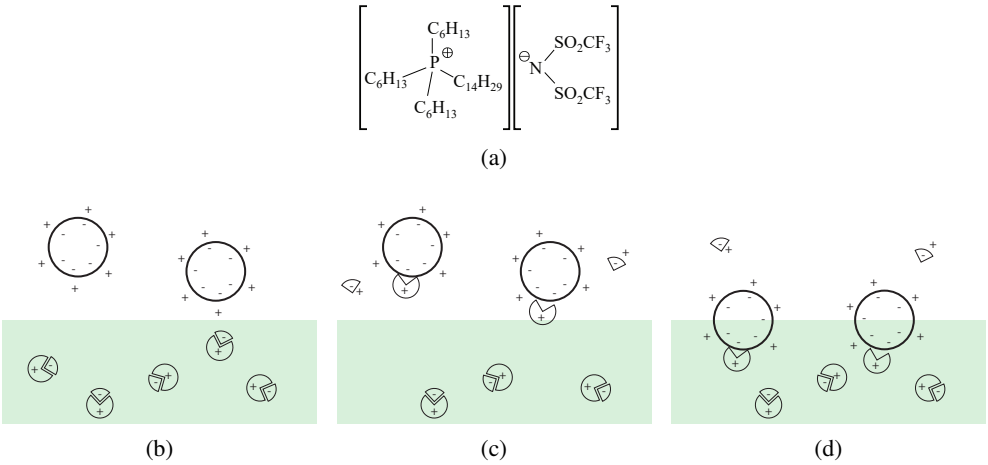

Figure 5.1 – (a) Chemical structure of the ionic liquid IL-109, used in this experiment. (b)–(d): Sketch of a possible mechanism of adsorption of silica particles to the interface, through complexation of the cation from the ionic liquid with the negatively charged particle. This complex then adsorbs to the oil/water interface.

purified with centrifugation, and resuspended in distilled water. An initial $10\times$ dilute stock suspension was prepared to prevent spoiling the concentrated stock solution. Particles had a diameter $a = 0.72\,\mu\text{m}$, with a standard deviation $\sigma = 0.06\,\mu\text{m}$, as determined by light scattering.

Interfaces were prepared as described in Section 4.2.2. In short, a small amount of oil was placed on a patterned microscope slide, and wiped off in order to fill the channels with oil. After this, a metal ring was added to contain the water phase, consisting of a dilute silica suspension. The oil phase consisted of either 1,8-dibromooctane (DBO) or bromobenzene (BBZ), fluorescently labelled with either Pyrromethene 605 or Nile Red to facilitate detection of the interface. To induce spontaneous adsorption of silica particles, 1–10 mM of the ionic liquid trihexyl(tetradecyl)phosphonium bistriflamide (IL-109, Cyphos) was added to the oil phase.

Just prior to each experiment, the dilute silica stock suspension was sonicated for 5 min, after which a final dilution was made. Salt was added in a number of cases, such that the water phase contained 0–5 mM NaCl.

To estimate the silica/oil/water contact angle, we placed a $1\,\text{cm}^2$ piece of a silica wafer in a cuvette. We then filled the cuvette with water, and deposited a $20\,\mu\text{L}$ oil droplet at the silica/water interface. We followed the evolution of the contact angle for a period of 900 s; experiments were repeated 10 times. The contact angle was estimated from a tangential fit to the droplet.

The oil/water surface tension was measured with a Sinterface PAT-1 surface tensiometer.

For imaging of colloids at oil/water interfaces, we used a Visitech Infinity 3 setup, with a $100\times$ oil immersion objective, resulting in a field of view of about $90\times90\,\mu m^2$. The scan rate was set to 10 fps. Images were recorded in the centre of the channel, to eliminate wall effects of the channel ends.

5.3 Results

5.3.1 Contact angle and surface tension

To estimate the three-phase contact angle of silica particles at these oil/water interfaces, we measure the equilibrium contact angle between a droplet of 1,8-dibromooctane at a silica wafer, which is placed in a cuvette filled with 0.5 M NaCl. We measure this for pure oil, and for oil with ionic liquid and/or the fluorescent dye Pyrromethene 605. The contact angle is measured through the water phase. The average contact angle is shown in Figure 5.2a. We observe that for each experiment the contact angle initially increases and then stabilises. Although the presence of ionic liquid or a dye affects the equilibrium contact angle, dynamics are not significantly changed, as in each experiment the equilibrium contact angle is reached within the first minute. We find an equilibrium contact angle of approximately 60° for the 1,8-dibromooctane/water/silica three-phase contact line, in the presence of 1×10^{-3} M ionic liquid and Pyrromethene 605. This indicates that in case of interface adsorption, particles will only be partly submerged in the oil phase, and remain predominantly in the water phase.

It is essential that the oil/water interface is free from impurities, as these can have a significant effect on particle dynamics and interactions. The surface tension is a good proxy for this, as it is generally very sensitive to surface-active impurities. Results of a surface tension measurement of bromobenzene are shown in Figure 5.2b. We tested clean bromobenzene, as well as bromobenzene with both ionic liquid, and Nile Red dissolved.

On a linear scale, it appears that a surface tension equilibrium is reached within the first minute. However, a logarithmic plot of surface tension vs. time, as shown in Figure 5.2b reveals that this is not actually the case, as the surface tension keeps dropping over the course of at least 1×10^3 s. The addition of ionic liquid or Nile Red does not significantly affect the surface tension value or the equilibration time. However, the most significant drop in surface tension takes place during the first $\sim 1\times10^2$ s. Given that the time scale for preparation of interfaces, loading with particles, and the actual acquisition of image sequences well exceeds this initial 'stabilisation' period, it is safe to assume that the surface tension and the contact angle are constant during the experiment.

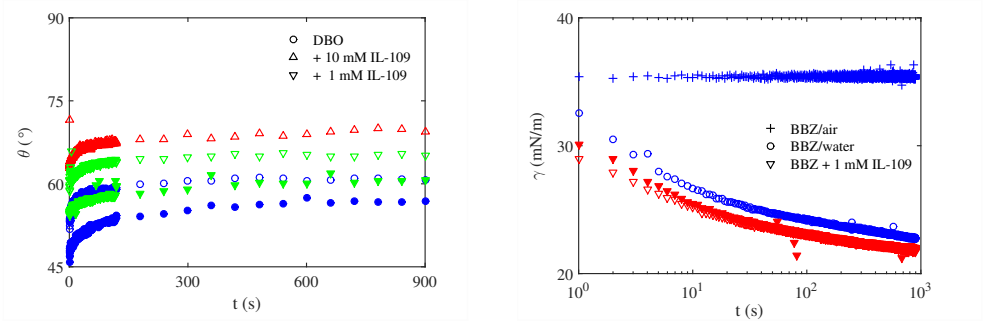

(a) (b)

Figure 5.2 – Contact angle and surface tension: (a) The contact angle between 1,8-dibromooctane, water, and silica. Experiments with the dye Pyrromethene 605 added to the oil phase are indicated by a filled symbol. (b) The surface tension γ of bromobenzene. Experiments with the dye Nile Red added to the oil phase are indicated by a filled symbol. In both cases we see that environment variables affect the equilibrium result, but dynamics are relatively unaffected, as in each case equilibrium is reached or approximated within approximately 2 min from the start of the experiment.

5.3.2 Silica particles at interfaces

The apparent mobility of silica particles at the oil/water interface is much greater than in the experiment with microgel particles. As a result of faster movements, a higher acquisition rate (10 fps vs. ~1 fps) is employed to ensure sufficient tracking resolution. This increase in framerate is in line with a decrease in oil viscosity, as literature reports a viscosity of approximately 1×10^{-3} Pa s for bromobenzene or 1,8-dibromooctane [5], versus a viscosity of 1×10^{-2} Pa s for mineral oil [6] as used in the microgel experiments.

Although we find that silica particles adsorb spontaneously to oil/water interfaces, it appears more challenging to find an interface with a sufficient number of particles to display a reasonable amount of capillary interaction, as compared to the microgel experiment. The apparent capillary interaction range and strength are much smaller, as particle pairs and clusters are significantly less stable compared to the microgel case. Particles still arrange in a quadropolar pattern, which confirms that interactions are still capillary-force driven by interface curvature anisotropy. We observe significant photobleaching, which effectively limits the acquisition time to about 1×10^3 frames. This means that a long-term evolution of cluster formation can not be tracked in real time.

Three observations indicate a weak pair potential: pair detachment, where a particle pair disintegrates after being in apparent equilibrium; pair reattachment, where a particle moves well beyond the usual limit of equilibrium vibrations, followed by a return to (apparent) equilibrium; and cluster rearrangement, where a particle detaches and subsequently reattaches to a different position within the same cluster, usually at the neighbouring position. A montage of a silica cluster at an oil/water interface is shown in Figure 5.3. Within 20 s, we observe pair detachment, as we see a complete particle cluster disintegrate between 5–8 s. The cluster then reforms, with most of the particles being placed at their 'original' position. This is an example of pair reattachment. Cluster rearrangement occurs a number of times, for instance between 10–14 s, where we see an L-shaped cluster rearrange into a T-shape. The shorter interaction range is also visible, as a number of other particles in these frames remains unaffected by the presence of this cluster. From these observation we expect an interaction energy in the same order of magnitude as the thermal energy $k_\mathrm{B}T$.

We attempt to construct the pair interaction potential from particle approach curves following the method already discussed in Chapter 4. In short, particle pairs are tracked and aligned to $t = t_0$, which we define as the first moment of contact between particles. Traces are grouped together based on the deviatoric curvature $\mathcal{D}$ of the interface, and we then calculate the approach velocity from the average approach trajectories at $t < t_0$. With the assumption that Stokes drag is the main force counteracting particle movement, we find the driving force for particle attraction as $F = \xi \cdot v$, where ξ is the Stokes friction coefficient. The integral of this force curve

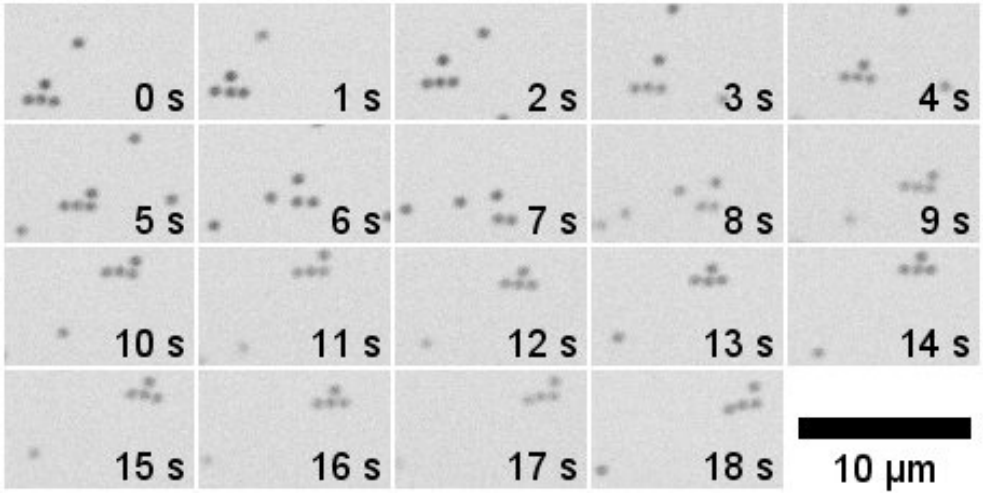

Figure 5.3 – Montage of silica particles interacting at an oil/water interface. The original T-shaped cluster in the first frame ($t = 0\,\mathrm{s}$) disintegrates and rearranges a number of times within less than 20 s.

then yields the pair potential $U(r)$. We use three bins to characterise our sample: strong ($\mathcal{D} > 1/300\,\mu\mathrm{m}^{-1}$), medium ($1/300\,\mu\mathrm{m}^{-1} \geq \mathcal{D} > 1/1200\,\mu\mathrm{m}^{-1}$), and low ($\mathcal{D} \leq 1/1200\,\mu\mathrm{m}^{-1}$) curvature anisotropy. Pair traces at $t \geq t_0$ can be used for a calculation of the equilibrium distance r_{eq}, and the equilibrium potential energy is found as $U(r) \propto -\ln P(r) + \mathrm{cst}$.

Experimental results are shown in Figure 5.4. Individual pair tracks are shown in grey in the background of Figure 5.4a, for interfaces with strong anisotropy. Although approach curves converge towards the contact time $t = t_0$, they do not collapse onto a clear master curve due to thermal fluctuations. Consequently, the mean approach curves are noisy. This results in spiked velocity curves, as shown in the inset in Figure 5.4a.

The spikes immediately impact the reliability of this curve, as each spike contributes to the integral $U(r)$. This is most significant for particles at interfaces with medium curvature anisotropy, as the approach curve for this set of measurements shows a disproportionate amount of positive spikes. Each of these results in a jump in the (cumulative) approach energy $U(r)$, as shown in Figure 5.4b. As the interaction potential for particles at interfaces with strong anisotropy is the least affected by spikes, we assume this is the most reliable curve. We find that the maximum interaction energy for this experiment is in the same order of magnitude as the thermal energy $k_{\mathrm{B}}T$. This is in agreement with the observation of pair separation and cluster rearrangements. Unlike the experiment with microgel colloids described in

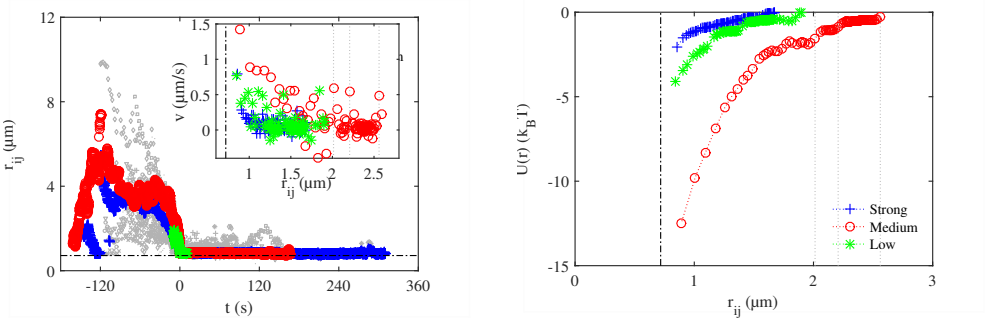

(a) (b)

Figure 5.4 – Long-range interaction between silica particles. (a) Approach curves. Raw data, shown in grey symbols for interfaces with strong anisotropy, show the excessive post-equilibrium fluctuations. Inset: the derived velocity curves show large fluctuations as a result. (b) The interaction potential, constructed from particle approach curves, may be negatively impacted by fluctuations, and thus less reliable. The dash-dotted line indicates the particle diameter. For clarity, only 5 % of raw data points are shown. A thin, gray line indicates the position of three outliers in the velocity curve that have a significant effect on the energy curve (medium anisotropy).

Chapter 4, we cannot distinguish a clear trend between interface curvature anisotropy and particle interactions, neither the range or strength of interactions, or the stability or formation of (extended) particle clusters.

An attempt was made to calculate the equilibrium potential from pair fluctuations, using Boltzmann statistics of bond length fluctuation as a proxy for the equilibrium potential, similar to the approach described in Chapter 4. However, we find that this approach is not feasible as a result of weak pair interactions. The reasons for this are discussed in following section.

It is, however, instructive to briefly consider the pair equilibrium distance. For the microgel system we found a clear correlation between the particle equilibrium distance r_{eq} and interface curvature anisotropy $\mathcal{D}$, as discussed in Section 4.3.2. On the other hand, for the current experiment with silica particles we find an overall average equilibrium $r_{eq} = (0.83 \pm 0.15)\,\mu m$; the equilibrium distance for either curvature bin ranges from 0.82–0.83 µm, with a standard deviation of 0.08–0.20 µm. The error given here is the standard deviation σ. The nearly identical averages, but mostly the error range (up to 24 % in the worst case), indicate that deviatoric curvature does not significantly affect the silica equilibrium distance.

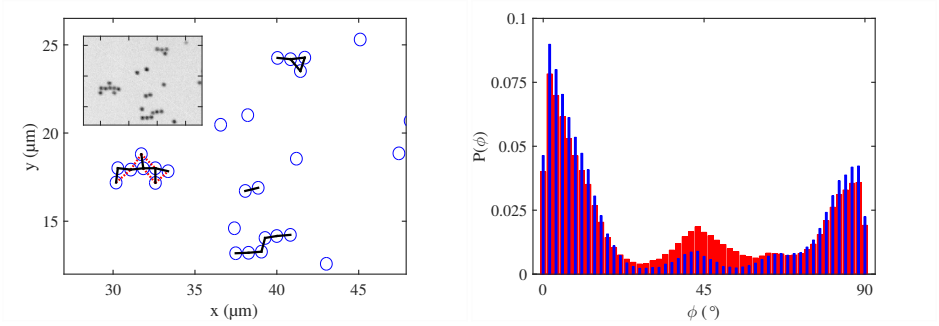

(a) (b)

Figure 5.5 – Bond angle analysis: method. (a) Magnified view of silica particles at an oil/water interface. Identified particles are shown in blue circles; black lines indicate particle bonds with a cutoff length of 1 µm. Red, dotted lines show a cutoff length of 1.2 µm. The inset shows the corresponding section of the original image frame. (b) Histogram showing the probability distribution $P(\phi)$ of bond angles ϕ at an interface, for a bond length of 1 µm (blue, narrow bars), and 1.2 µm (red, wide bars). The histogram is calculated for the complete field of view for the entire image sequence.

5.3.3 Bond angle analysis

The calculation of a pair interaction potential as described in the previous section requires a sizeable amount of manual input, and is therefore prone to error. Automation of the analysis is not straightforward. Besides these considerations, pair stability is also a variable, as the calculation of an equilibrium interaction potential assumes particles vibrating around an energy minimum. For our system with silica particles, we find that the range and strength of interaction are insufficient for this calculation.

A bond angle analysis, on the other hand, is more easily automated. Only nearest-neighbour interactions are taken into account by means of a cutoff length, and the bond direction between particle pairs is calculated on a per-frame basis. The effect of thermal fluctuations on pair stability is therefore greatly reduced.

Pairs are selected as follows. After particle centroid tracking, we calculate a distance matrix from the Cartesian particle coordinates, for each frame of an image sequence. This procedure takes all possible particle pairs into account. Pairs at a distance larger than the cutoff length are discarded. For the remaining particles, the bond direction is calculated.

The particles in our system are subject to quadrupolar capillary interactions, dictated by the curvature of the interface. As a result of this quadrupolar symmetry,

we expect particles to align to the principal curvature axes of the interface. If we compare the bond direction between particles to the local curvature, we arrive at the bond angle ϕ. It is possible to perform this calculation for arbitrarily shaped interfaces, as long as the shape of the interface is known [7]. In our case, the calculation is simplified as our interfaces have half-cylindrical interfaces, the axis of which are aligned to the x-axis of the microscope image. As the principal directions of curvature of a cylinder are perpendicular to each other, we arrive at the bond angle ϕ simply by comparing the absolute value of the bond direction relative to the x-axis of the image.

For a system with quadrupolar capillary interactions, we expect a major contribution of parallel and perpendicular orientations. A suitable metric in this case is the $\langle\cos(4\phi)\rangle$ value. We first calculate bond angle probability distribution $P(\phi)$ between 0° and 90°, in 50 bins. We then find

$$\langle\cos(4\phi)\rangle = \Sigma P(\phi) \cdot \cos(4\phi), \tag{5.1}$$

which equates to 1 for exactly 0° or 90°, and decreases for deviations of perfect parallel or perpendicular alignment. This average is therefore a good descriptor of the average order in the system.

In Figure 5.5a we show the process of pair selection, and the relevance of cutoff length choice. Identified particles are shown as open circles. Particle bonds are indicated as black lines for a cutoff length of 1 µm, and as red lines for a cutoff length of 1.2 µm. The longer cutoff length results in the unwanted inclusion of non-nearest neighbours. The probability histogram, calculated for the full field of view and the entire image sequence, is shown for each case in Figure 5.5b. We see a significant increase of the peak around 45° when a longer cutoff length is used. In this particular example, the $\langle\cos(4\phi)\rangle$ value decreases from 0.63 to 0.44. We observe a bias in the histogram for parallel (0°) versus perpendicular (90°) pair alignment. This does not affect the results, as the contribution of parallel and perpendicular interactions to the calculation is the same.

The cutoff length is determined as follows. For the microgel experiment described in Chapter 4 we find a curvature-dependent equilibrium distance r_{eq} of 1.6–1.8 µm, with a standard deviation σ of 0.1 µm (6–7 %). The equilibrium distance of silica particles, as described above, is 0.83 µm, with a standard deviation of 0.15 µm (18 %). Based on these numbers we choose a bond length of 2 µm ($\sim r_{eq} + 2\sigma$) for the analysis of the microgel bond angles, and 1 µm ($\sim r_{eq} + \sigma$) for the silica system. Sampling of a number of interfaces for both systems indicates that these values are suitable for further computation.

A scatter plot that shows the $\langle\cos(4\phi)\rangle$ value for a large number of interfaces is shown in the background in each plot of Figure 5.6. Raw data shows a wide distribution of values, largely independent of the deviatoric curvature. Locally, the

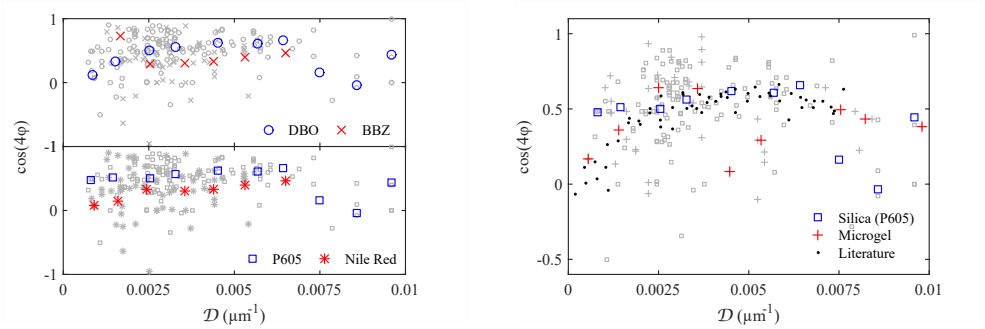

(a) (b)

Figure 5.6 – Bond angle analysis: results. Small, grey symbols are the raw data for each individual interface. Average values are calculated for 10 bins, each $2 \times 10^{-3}\,\mu m^{-1}$ wide. (a) Silica bond angles, analysed for oil type (top), and fluorescent label (bottom). At first sight, $\langle \cos(4\phi) \rangle$ for dibromooctane (DBO) appears to go through a maximum at intermediate $\mathcal{D}$. However, closer inspection reveals that the fluorescent label is responsible for this effect. (b) Comparison of silica samples at interfaces labelled with Pyrromethene 605 and microgel bond angles. There appears to be no correlation between $\mathcal{D}$ and $\langle \cos(4\phi) \rangle$ for these systems but we find a rather constant $\langle \cos(4\phi) \rangle \approx 0.6$; in both systems deviating values (high $\mathcal{D}$ for silica; low and intermediate $\mathcal{D}$ for microgels) coincide with a small number of particle detections. Black dots indicate literature reference values [7].

Table 5.2 – Total number of detections, specified by experimental parameters

	Count	%
Total	4 033 582	100
1,8-Dibromooctane	3 277 455	81.25
Bromobenzene	756 127	18.75
Pyrromethene 605	2 657 184	65.88
Nile Red	1 250 968	31.01
DBO & P605	2 657 184	65.88
DBO & NR	617 993	15.32
BBZ & P605	0	0
BBZ & NR	632 975	15.69

$\langle\cos(4\phi)\rangle$ value can be as high as 1, indicating perfect alignment to local curvature, but the average of an ensemble of particles reaches a maximum $\langle\cos(4\phi)\rangle \approx 0.6$. This is in line with an earlier study [7]. To gain more insight, we group the samples in 10 bins, based on the deviatoric curvature of the interface, with a bin size of $2 \times 10^{-3}\,\mu m^{-1}$. We can further split these samples based on ionic liquid or salt concentration, oil type, or fluorescent label. Careful examination of the appropriate results reveals that the concentration of ionic liquid (1×10^{-2} M or 1×10^{-3} M in most cases) has negligible influence on these results.

We find an *apparent* increase in $\langle\cos(4\phi)\rangle$ when comparing 1×10^{-3} M NaCl with 5×10^{-3} M NaCl, suggesting that a decrease in salt concentration increases order. However, there is also limited evidence that the complete absence of salt has a negative impact on $\langle\cos(4\phi)\rangle$ values. Moreover, the salt concentration mainly coincided with choice of oil phase and/or fluorescent label. In view of this, combined with the mentioned contradictory observations, it appears plausible that salt concentration, at least in the investigated range of a few mM, has negligible impact on the order of the silica system.

If we then turn our attention to the oil phase and fluorescent label, it appears that both have a significant impact on $\langle\cos(4\phi)\rangle$ values, as shown in Figure 5.6a. For DBO we find an apparent maximum of $\langle\cos(4\phi)\rangle$ at intermediate $\mathcal{D}$. We also find slightly higher $\langle\cos(4\phi)\rangle$ values for DBO than for bromobenzene. However, we like to remark that the erratic results at high deviatoric curvature are likely caused by the significantly lower number of samples (the last four bins, $\mathcal{D} > 0.014\,\mu m^{-1}$, contain only ~2 % of all observed 'bonds').

Instead of oil type, we can also explore the effect of fluorescent label. Especially the first bin (low curvature anisotropy) is appealing, as the rather low overall average is split in an even lower value for interfaces labelled with Nile Red, and a significantly higher average for interfaces labelled with Pyrromethene 605. In general we find that samples labelled with Pyrromethene 605 attain a higher $\langle\cos(4\phi)\rangle$ value than Nile Red-labelled samples. For both data sets we observe a slight increase in $\langle\cos(4\phi)\rangle$ with $\mathcal{D}$. This increase is slightly more pronounced for Nile Red. However, for both oil and fluorescent label we have to interpret these results with caution, as a result of the large spread in individual sample values.

Approximately 66 % of all samples consist of dibromooctane, labelled with Pyrromethene 605. The remainder is nearly equally distributed between dibromooctane and bromobenzene, each labelled with Nile Red. No samples with bromobenzene and Pyrromethene 605 were analysed.

We propose the following hypothesis to explain the variations in this system: the $\langle\cos(4\phi)\rangle$ value depends on $\mathcal{D}$, but is easily influenced by surface properties. Nile Red is a known to exhibit surface activity. We can use this to explain both the lower value of $\langle\cos(4\phi)\rangle$, and stronger dependence on $\mathcal{D}$, as compared to samples with a

non-surface active label. Particle interactions are determined by capillary interactions. In Section 5.3.2, we discussed that these interactions are weak and short-ranged for the system under investigation. As with a repulsion-driven ordering, which is easily broken upon addition of excess salt, a capillary force-driven order is easily altered in the presence of surfactants. If the surface activity of Nile Red is sufficiently large, this can explain the loss of order, or rather the decrease of direction-specific order, in the system. The surfactant contribution to the overall force is larger at interfaces with lower deviatoric curvature. As for the *apparent* difference between DBO and BBZ samples, this observation coincides mostly with the choice of label, and is therefore not a valid observation.

We briefly compare the results for silica particles at oil/water interfaces with the microgel particles discussed in Chapter 4, for which we know that the strength of interaction does depend on $\mathcal{D}$. Results are shown in Figure 5.6b. For silica particles, we only show results of interfaces labelled with Pyrromethene 605. We see that microgel bond angles have erratic behaviour. However, like with silica particles at high deviatoric curvature, each of these erratic low values coincides with a low number of observations. As a result, we cannot draw a clear conclusion from this analysis with regards to microgel particles, other than that, in the case of sufficient statistics, the $\langle\cos(4\phi)\rangle$ value is likely to be relatively unaffected by $\mathcal{D}$.

5.4 Discussion

5.4.1 On the short range and low strength of interaction

As shown above, silica particles do adsorb to oil/water interfaces, provided a small amount of ionic liquid is present in the oil phase. Ionic liquids do not readily dissolve in (mineral) oil, but halogenated oils are capable of dissolving ionic liquid. We chose to use bromobenzene and 1,8-dibromooctane as the oil phase for our experiments.

As expected, silica particles do exhibit anisotropic capillary attraction when adsorbed at an anisotropically curved interface. However, in Section 5.3.2 we have shown that the range as well as the strength of these interactions is severely limited, compared to experiments with different particles. This short range and low strength can have different reasons. In order for anisotropic interactions to take place, there needs to be an anisotropic deformation of the interface, but the magnitude of this deformation is correlated to the particle contact angle. For instance, a very hydrophobic or very hydrophilic particle with a contact angle of 0° or 180° could sit at the interface without disturbing it. Silica particles at oil-water interfaces are reported to have contact angles in the range from 20° to 140°, depending on surfactant concentration [8, 9]. Another possibility is that the particles sit at the interface without acquiring an equilibrium contact angle, thus avoiding the necessary interface deformation to

satisfy the constant contact angle requirement. These two effects could contribute to the absence or decrease of anisotropic capillary interactions.

Also, silica particles acquire surface charge when suspended in water. This charge leads to electrostatic repulsion, partly counteracting the capillary attraction. Another possibility is modification of the contact line as a result of particle roughness. This alteration in turn affects the curvature-induced deformation of the oil/water interface, potentially reducing the capillary attraction. Halogenated oils are known to be subject to degradation, especially under influence of light. Degradation products may therefore be present in the oil phase, and these can be surface-active. This may have a significant impact on the balance of the various surface forces that ultimately determine the magnitude of capillary attraction.

The low overall strength of interaction between silica particles in these experiments is likely a combination of these factors.

5.4.2 Experimental challenges

Contact angle measurements of dibromooctane, water, and silica show an initial increase followed by a stabilisation of the contact angle. This increase is likely the result of contact line relaxation, as the droplet is inflated to its maximum volume while in contact with the silica surface, and is then allowed to relax after the needle is withdrawn.

Although the surface tension of bromobenzene in air is stable, we find that this is not true for bromobenzene in water. We hypothesize that this is due to the presence of surface-active degradation products in the oil phase, the origin of which is discussed briefly in Section 5.4.1. Another possibility is the occurrence of trace amounts of impurities in the oil.

Significant photobleaching is observed for these silica particles, especially compared to the microgel system discussed in Chapter 4. A number of possibilities exist. As a result of faster particle movement, a significantly higher acquisition rate is necessary, and this in turn requires the laser intensity to be higher. This can be a reason for increased photobleaching. The effect could also be related to the confocal microscope setup, since a significantly different setup was used, but experiments with identical particles with both microscopes do not point out a significant effect on photostability. Another possibility is the particle material affecting photostability as a matrix effect. However, we believe that the major contribution comes from the photostability of the dye itself; fluorescein, the dye used to label the silica particles, is significantly less stable than Nile Red, the dye used in the microgel experiment.

The apparent short range and low strength of capillary interactions as described in Section 5.3.2 and Figure 5.3 impose various difficulties to the particle tracking method. On a particle level, pair rearrangement and cluster rearrangement are the same process, but they have different implications for particle tracking. In case of a cluster rearrangement, where a particle detaches and reattaches in a different position, tracking needs to be terminated as otherwise a next-nearest neighbour distance is monitored. This is not necessary for a pair rearrangement. Although upon separation the interparticle distance will temporarily increase to a larger value, it returns to the same equilibrium distance upon return. It would be possible to discard all particle tracks that go beyond a certain cutoff separation distance after being initially in equilibrium. Although this would remove erratic particle pairs from the analysis, it would also lose a significant number of proper pairs. This is undesirable from a statistics perspective. Therefore, all tracks are manually monitored and terminated where necessary, to improve statistics at the cost of manual input.

Individual outliers in an otherwise clean dataset can be considered a measurement error. A correction for these outliers is straightforward and acceptable. However, our experiments result in noisy datasets, and we find a significant number of spikes in the approach velocity curves. More important is that the spikes and the background fluctuation have a similar order of magnitude. In this context, a correction is not appropriate.

An equilibrium energy potential for the silica system could not be calculated successfully. In a few obvious cases, pair tracking is terminated, for instance when a particle escapes beyond the capillary interaction range and does not return to re-form a bond. Tracking is also terminated upon cluster rearrangement, as this would otherwise result in tracking of diagonal, non-nearest neighbour pairs. However, pair tracking should not be terminated for brief particle excursions at larger-than-usual separations, provided the particle reattaches to reform the same pair, since these excursions reflect the shallower, wider equilibrium potential they are in. For a system with a limited, reasonably symmetric vibration around a clearly defined equilibrium distance, a cutoff distance can be defined for the maximum pair distance. In the current system, such a cutoff would result in a truncated potential, since part of the escape and return trajectory of particles is removed from the probability calculation. Consequently, the interaction range for the equilibrium analysis would be much larger than the capillary range. An estimate for the capillary range is given by the approach curves to be around 1 µm; the equilibrium calculation would extend beyond 2 µm. This defeats the purpose of the two-step calculation, where a small overlap between the approach and equilibrium curve is used to construct the cumulative interaction potential.

Cherry picking suitable particle pairs for tracking has a number of drawbacks. Possible errors as a result of manual particle track selection include the omission of certain particle pairs, or incorrect assignment of t_0 or the end of a tracking event. Pair selection errors, for instance by copying incorrect particle numbers, are manually removed from the analysis at a later stage and are thus of no concern. The problems described in the previous section could potentially be solved by analysis of a larger, cleaner dataset. This would require extensive automation, in order to make the process more facile, as well as more reproducible.

Sources of error in an automated bond angle analysis are unavoidable. Misdetections, such as the erroneous detection of a single particle as two, and the detection of non-adsorbed particles, temporarily introduce new particle bonds. However, their overall contribution is considered negligible. Most of these temporary bonds are beyond the cutoff length. Non-adsorbed particles may temporarily move into the field of view, but their velocity is generally higher than adsorbed particles, hence their contribution is short lived. This means that statistics are dominated by particle pairs with a longer lifetime, and therefore the advantages of the fully automated approach outweigh these minor disadvantages.

The bias in the histogram for bond angles towards 0° versus 90° is a result of image alignment. Two factors may attribute to this. First, the long axis of the channel is aligned to the image x-axis. As a result, more particles are available to probe the x-direction, increasing the chance of an encounter or formation of an elongated chain in that direction. Apart from this, as the channel is curved in the y-direction, a longer chain would have to bend in order to conform to the curvature of the interface. Although gravity effects are negligible for individual particles, as reflected by the Bond number calculated in Section 4.3.1, this chain bending may result in an energy difference between a 'parallel' and 'perpendicular' arrangement of particles relative to the curvature direction.

Exact parallel or perpendicular alignment is rare, as indicated by the lower population of the bins at the extreme ends of Figure 5.5b. This is likely the effect of a small image alingment mismatch. While care is taken to align channels as best as possible to the image axis, and although visibly misaligned images are straightened before processing, a minor misalignment is unavoidable. Generally, image misalignment $\lesssim 1°$ is very hard to observe. A bin size of $\pi/100 = 1.8°$ was used to calculate the histogram, and this covers more than the estimated lower limit of image alignment precision. As the bond angle ϕ is calculated directly from the bond direction compared to the image axis, it is likely that this misalignment is the source of this error.

5.5 Conclusion

The title of this chapter asked a question: do anisotropically curved interfaces provide a foolproof way to induce anisotropic particle interactions? The simple answer to this question is affirmative, as both of the significantly different systems of colloidal particles at oil/water interfaces studied in this and the previous chapter yield anisotropic capillary interactions. However, as shown in the discussion, this is not as straightforward in reality. In this chapter, we attempted to simplify the experimental system, in order to approximate the theoretical model, through the study of colloidal silica spheres at oil/water interfaces with half-cylindrical curvature.

For this system we do find attractive interactions between individual particles, although the range and strength of this interaction is severely reduced compared to earlier experiments with microgel particles. As a result of this short-range, weakly attractive interaction, it was not possible to construct a long-range approach and interaction potential as in Chapter 4. A bond angle analysis revealed that short-term, short-distance order does occur for this system, and the average order is in line with literature results and results from the microgel experiment. Our results are therefore in line with the basic theoretical prediction that particles organise under the influence of capillary interactions, as a result of a capillary deformation of the interface by the particle. These results prove that the hypothesis is valid for a number of physically and chemically significantly different experimental systems.

One major assumption, however, did not prove true: silica particles, in this configuration, do not provide a 'simple' implementation of a hard sphere model. A number of possible reasons has been discussed. To summarise, the short range and low strength of interaction may be a result of a modification of the capillary interface deformation as a result of particle surface roughness, leading to a decrease of the attractive component of the combined pair interaction potential. On the other side is a possible increase in the repulsive contribution as a result of particle surface charge.

The research conducted in this chapter shows that an attempt to simplify an experiment by simplification of the apparently most significant part of an experiment, without keeping a close eye to the increased complexity of the other parameters, can lead to surprising results. Further simplification of the experiment is required to verify the theoretical prediction that the strength of interaction between spherical particles at anisotropically curved interfaces is a function of deviatoric curvature. In an ideal case, one should find a system of smooth, spherical colloids that adsorb spontaneously to liquid/liquid interfaces. The liquids themselves should be chemically stable, and preferably be purified prior to the experiment. Although non-surface active fluorescent labels exist, it is also possible to fit the interface curvature from particle positions, if coverage of the interface is sufficient. Ultimately, the reduction of any research question to its most basic components should yield the closest match to theory. Once a

solid understanding of the matter is reached, and preferably a basic proof of theory has been found, the complexity of the system can be increased to generalise the findings. Theory can then be updated as needed, for instance through inclusion of empirical constants or correction factors.

Finally, the contact angle of particles at the interface needs to be known in order to calculate the interaction potential for the actual system. Here we estimated the contact angle from a macroscopic model with a conventional drop shape analysis. It would be advantageous to use an in vitro technique on the actual experimental system. Alternatively, a semi-in vitro techniques like flash freezing or replica molding can be employed, although these have the disadvantage of potentially disturbing the (weak) equilibrium they are meant to preserve.

References

[1] O. S. Deshmukh, D. van den Ende, M. A. Cohen Stuart, F. Mugele, and M. H. G. G. Duits. Hard and soft colloids at fluid interfaces: Adsorption, interactions, assembly & rheology. *Advances in Colloid and Interface Science*, **2014**. *222*, 215–227. doi:10.1016/j.cis.2014.09.003.

[2] R. W. Style, L. Isa, and E. R. Dufresne. Adsorption of soft particles at fluid interfaces. *Soft Matter*, **2015**. *11*, 1–8. doi:10.1039/C5SM01743B.

[3] H. Monteillet, M. Workamp, J. Appel, J. M. Kleijn, F. A. M. Leermakers, and J. Sprakel. Ultrastrong Anchoring Yet Barrier-Free Adsorption of Composite Microgels at Liquid Interfaces. *Advanced Materials Interfaces*, **2014**. *1*. doi: 10.1002/admi.201300121.

[4] A. van Blaaderen and A. Vrij. Synthesis and characterization of colloidal dispersions of fluorescent, monodisperse silica spheres. *Langmuir*, **1992**. *8*, 2921–2931. doi:10.1021/la00048a013.

[5] S. Parthasarathi, K. Saravanakuamr, R. Baskaran, and T. R. Kubendran. A Volumetric and Viscosity Study for the Binary Mixtures of Dimethylsulfoxide with Benzene , Ethyl benzene , Chlorobenzene and. *International Journal of Science and Technology*, **2011**. *1*, 96–101.

[6] SigmaAldrich. Mineral oil (light) Product Specification sheet, **2016**. http://www.sigmaaldrich.com/catalog/product/sial/330779.

[7] D. Ershov, J. Sprakel, J. Appel, M. A. Cohen Stuart, and J. van der Gucht. Capillarity-induced ordering of spherical colloids on an interface with anisotropic curvature. *Proceedings of the National Academy of Sciences of the United States of America*, **2013**. *110*, 9220–4. doi:10.1073/pnas.1222196110.

[8] B. P. Binks and C. P. Whitby. Nanoparticle silica-stabilised oil-in-water emulsions: Improving emulsion stability. *Colloids and Surfaces A: Physicochemical and Engineering Aspects*, **2005**. *253*, 105–115. doi:10.1016/j.colsurfa.2004.10.116.

[9] B. P. Binks, L. Isa, and A. Therhemen Tyowua. Direct Measurement of Contact Angles of Silica Particles in Relation to Double Inversion of Pickering Emulsions. *Langmuir*, **2013**. pp. 4923–4927. doi:10.1021/la4006899.

Chapter 6

General discussion

The domain of soft matter stretches far and wide, and is a defining subject within the field of physical chemistry. In this thesis, we addressed three different subjects, with the common denominator that soft interactions are at the core of the studied systems. Repeatedly, observed that the combination of several small interactions result in large-scale interactions. Our work addressed several open questions on the effectiveness and operating mode of patterned adhesives; the wetting properties of soft materials, chiefly various functionalised hydrogels; as well as a thorough analysis on the kinetics of two-dimensional colloidal self-assembly on liquid-liquid interfaces with anisotropic surfaces, for two different model systems.

Naturally, the research described in the preceding chapters opens up a wealth of additional questions, suggestions for improvement of the existing work or experimental conditions, as well as valuable suggestions for future work. We discuss our findings and recommendations below.

6.1 Patterned adhesives

In Chapter 2, we studied bio-inspired patterned silicone adhesives. We focused on two distinct areas of interest, to study the effect of surface pattern hierarchy through clustering of adhesive pillars, and the effect of pattern ordering by placing the pillars in different geometries. Besides this, the effect of adhesive geometry was briefly investigated by comparing samples with a square or circle geometry. Although experimental results indicate no or very limited effect of pattern and geometry on adhesive performance, supporting computer simulations did suggest a beneficial effect of clustering patterned adhesives under certain circumstances in constant rate experiments.

6.1.1 Adhesive testing

The measurement of adhesive force is notoriously difficult due to a range of experimental complications. Adhesives, in particular patterned silicones, are sensitive to the experimental history. A well-known effect is the fouling of a substrate by silicone residue, as a result of silicone monomer or oligomer transfer from the adhesive to the substate [1]. In our experiments we chose to limit the influence of fouling by dust and silicone residue buildup by reusing the same glass substrate for multiple experiments. This way, the amount of silicone build up on the glass substrate can be considered to be constant and ignored when comparing results between experiments. A different approach would be to use a clean slide for each experiment. Although this offers a benefit with regards to substrate cleanliness, a disadvantage is that repeat runs of a single sample would likely show a decrease in adhesive performance throughout the experiment. To counteract this effect, one could start any adhesive experiment on a clean substrate with a given number of calibration runs prior to collecting experimental data.

Preload effects may occur for pressure-sensitive adhesives. For patterned adhesives, an optimal preload regime may exist. At too low preload, pillars do not make sufficient contact with the substrate, while at excessive preload, pillars start to buckle, and adhesion is reduced. We found that for patterned adhesive samples tested against flat substrates, there is no distinctive preload effect for values between these two extremes. Somewhat related to the preload effect is the duration of initial contact. This effect was not investigated in our work; generally, our samples were equilibrated under a constant preload for a set time prior to detachment, so that any preload duration effect is mitigated.

Other factors affecting adhesive testing are the cleanliness of the sample and substrate, and sample alignment. In our experiments these two factors were addressed by cleaning both substrate and sample with tape prior to an experiment to remove accumulated dust particles, and by attaching the measurement probe to the sample already aligned to the substrate. Some authors suggest using spherical or convex probes to circumvent alignment issues [2, 3]. Although misalignment between a sphere and a flat surface does not exist, the use of a convex probe results in partial attachment only, as well as the rise of significant preload effects, due to the center pillars being pressed into contact more strongly than edge pillars.

We briefly investigated the use of spherical probes in our work. However, we found the reduction in contact area to be too drastic to be able to accurately measure an adhesive force. Upon closer inspection, we find significant differences between our experiment and those described in literature. The first article considers pillars with a radius of 2.5 µm and a length of 20 µm, or an aspect ratio of approximately 10 [2]. The other article considers a substrate patterned with holes, with radii ranging from 25–250 µm at a maximum depth of 20 µm, or an aspect ratio of 0.1–1 [3]. Effectively,

one article describes a system with much longer, more compliant pillars, while the other considers a shallow, inverted substrate compared to our experimental system. In both of these more extreme cases, spherical probes may be beneficial. Longer, more compliant pillars may be able to attach to the spherical probe more easily, and accept a wider preload range than our relatively short, stiff pillars. On the opposite end of the spectrum, a spherical probe allows for exact alignment with the edge of a hole.

We tested our patterned adhesives exclusively using a perpendicular pull test setup, with the probe connected to a motorised stage, at a constant rate of withdrawal. A significant amount of time was invested in the improvement of the method. This methodology has a high degree of reproducibility, but resulted in rather coarse data acquisition. This was especially around the critical point, the peak of the adhesive force curve. Because our results indicate that adhesive failure is a catastrophic, potentially self-catalytic process, using a simple constant-rate pull with no force feedback can mean that adhesive failure takes place between two data points.

Two possible, albeit somewhat palliative, solutions are to either reduce the withdrawal rate, or to increase the data acquisition rate. Both methods have their disadvantages. Because most of the adhesive testing consists of waiting for adhesive failure to commence, slowing down the rate linearly increases the wait time between experiments. An intermediate solution could be to have different withdrawal rates for the 'linear' and the 'catastrophic' parts of the measurement, but this may complicate the test. First, it requires knowledge of the exact separation at which adhesive failure starts, in order to slow down the probe before it reaches this separation. Secondly, a decrease in withdrawal rate during the experiment might affect the physics, as our adhesive pillars essentially behave as springs that might bounce upon acceleration or deceleration of the probe. To increase the data rate is not always possible, for instance when the maximum data acquisition rate of the equipment is reached, or because it generates excessively large amounts of data.

An interesting case for extended study is to instead change the constant rate protocol to a constant force mode. This may be more realistic from a practical perspective as well; generally, when removing an adhesive, one applies a certain force, and not a certain rate of removal. Also, this shows the load-bearing force of an adhesive, and improvements in adhesive performance in this way could lead to delayed failure and an improved service life thereof. In theory, a motorised stage with force feedback could be employed for this protocol. However, there are several disadvantages to this approach as well: there will be a signal delay, and the equipment needs to be properly calibrated for each sample, in order to prevent excessive jitter due to overcompensation in either direction, resulting in repeated acceleration and deceleration of the probe.

However, there is one omnipresent, stable force of nature that we could use. Instead of controlling separation and measuring force, we could measure separation

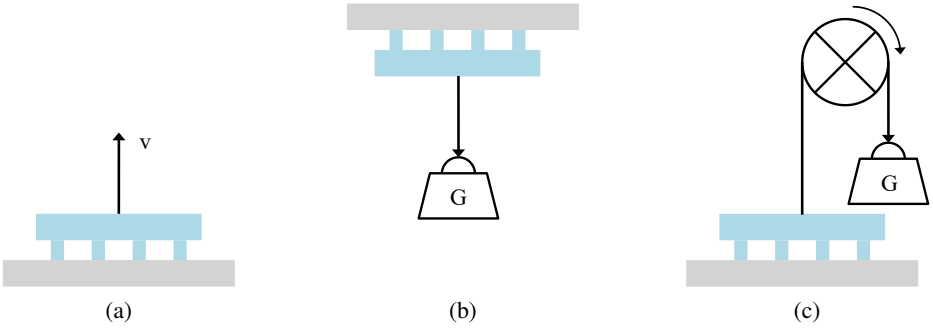

Figure 6.1 – Different adhesion setups. (a) The setup as used in our experiments described in Chapter 2, where the adhesive is pulled from a substrate at a constant rate. (b) An inverted gravitational setup, and (c) a gravitational setup using a pulley and a rotation sensor to detach a sample from a substrate.

and use gravity to perform a constant-force experiment. The substrate can either be attached upside-down, relative to our experiments described in Chapter 2, with a weight pulling down on it. A setup that might be easier in practice would use the same sample orientation as in our previous experiments, with the weight suspended over a pulley, adding in a rotary motion sensor to measure the distance travelled. This setup can be easily adjusted to different sample sizes by adding or removing weight from the probe. A sketch of the previously used setup and the suggested gravitational setups is provided in Figure 6.1. A variation of the pulley setup using a cantilever, with the sample and weight on opposite sides of a pivot, has been described in literature [4].

Finally, literature also suggests that various cleaning and storage protocols may limit the effect of silicone fouling of the substrate [1]. Although we did recognise the effect of ageing on silicone adhesives in general, we did not consciously take the exact sample age into account. Generally, adhesive samples would be between one day and one week old, although at times, we may have run (repeat) test with older samples. This may have negatively affected the margin of error in our experiments.

6.1.2 Adhesive sample design

One complication in the testing of patterned (adhesive) samples is the enormous parameter space to be explored: sample and feature size and shape, the relative amount of features on a given area of substrate, as well as substrate properties, such as material choice and in the case of gels, gel strength.

One important aspect of the gecko's adhesive system is the multidimensional approach to adhesion, as shown in literature [5] and briefly summarized in Chapter 2. All

these different dimensions play a certain role in the remarkable adhesive properties, from the macroscopic animal itself, via 'fingerprints' on its toes and hair-like setae, finally branching into spatula-shaped adhesive patches. We find that this multidimensional nature of adhesion is severely underrepresented in both literature [2, 3, 6–10] and our work: these articles, like our work, generally focus on one-dimensional surface patterning, for instance with holes or pillars, with variable feature size and ordering. Some authors investigate somewhat more complex situations, for example the comparison of the adhesive properties of an adhesive block with that of blocks of variable aspect ratio, multiple posts in a row, and some more complex shapes, such as a setup where a few adhesive pillars are attached under an angle to the end of a larger seta-like structure [11]. A review article mentions fibrillar arrays with various exotic tip end shapes, but still mostly covers onedimensional approaches to biomimetic adhesion [12]. We can find multidimensional adhesive simulation results published as an MSc thesis [13], and a feature article that highlights several multidimensional patterns [14]. A rather more in-depth investigation into multidimensional pillar hierarchies is provided by Rohrig et al. The authors describe how they use direct laser writing to generate patterned adhesives with multidimensional pillar hierarchies, and include the effect of pillar tip shape as well. The authors conclude that mushroom-shaped tips generally improve adhesion, and that the dry adhesion of a hierarchical design responds positively to appropriate preload [15].

We designed a contact mask for a clustered adhesive design, with final features of the same size as our regular patterned adhesives, and a secondary contact mask intended to project an additional higher dimension on top of these structures. An illustration of such a process and the expected results is shown in Figure 6.2. However, due to experimental challenges encountered with producing standard lithography, we did not attempt to create this multidimensional sample.

Other ways to explore the aforementioned parameter space are for instance patterned adhesives with variable pillar diameters. A rather mundane difficulty that arises here is the processing cost and time needed to generate adhesive substrates. It starts with a mask design. Although multiple masks can be designed or auto-generated with relative ease, we find that it is difficult to plan ahead too much, as experimental results may point out flaws with a certain design. In our case, we found that the square feature shape in our original design, as well as the total sample size, were not optimal. If a lot of effort is put in designing ahead, this can be a setback, so it appears to be best to approach the subject in smaller steps. Besides the mask design, the production of lithographic masters for adhesive substrates is very time-consuming. Improvements are possible, but prohibitively expensive in terms of material cost.

Computer simulations may prove suitable in assessing this vast parameter space. Our results obtained with a stochastic model described in Chapter 2 showed promising results, and indicate possible directions for future work and advanced sample design.

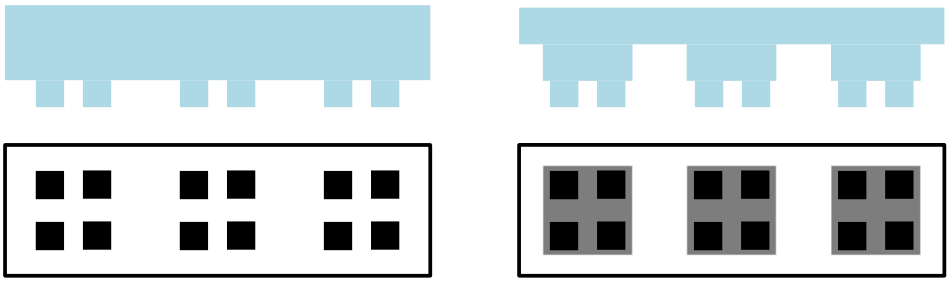

Figure 6.2 – Illustration of a possible multidimensional lithography process. (a) Side view (top) and photomask (bottom) for a standard one-step lithography process with 3 clusters of 4 pillars each. (b) A multidimensional patterned sample, where the 3 clusters are now combined together into one larger pillar in the secondary step. The illustration in the bottom shows an overlay of the primary and secondary photomask. The secondary mask is shown in a lighter shade for clarity.

One observation was that clustering could be effective, albeit at much larger cluster to sample ratios than those tested in the laboratory. This suggests that sample design parameters should be investigated relative to each other, and not exclusively based on absolute values of individual properties. Preliminary results obtained with this model also indicated a possible positive effect of variable pillar sizes on adhesive performance.

Our simulation results indicate that two distinct regimes of adhesive failure exist, a deterministic regime and a stochastic regime. As our laboratory experiments showed the deterministic regime exclusively, this was the focus area of our computer simulations. It could however be advantageous to explore the stochastic regime as well, in order to discover adhesives with a wider range of applications, for instance an adhesive pattern that is both resistant to slow detachment process, as well as being resistant to a sudden high-velocity pull. Computer simulations could also be employed to map the boundaries between these two regimes more precisely.

With regards to the aforementioned increase in computational power, it is worth to note that our simulated samples were significantly smaller in number than our laboratory experiments. Our simulations were carried out with samples of $N = 900$ pillars, as opposed to our initial experiments with $N = 57\,600$ pillars. This is somewhat conflicting: our laboratory experiments were limited in physical size mainly due to the experimental setup and increasing difficulties with sample flatness and alignment for increasingly large samples. These effects are not applicable to computer simulations, where the surface area could theoretically be made infinitely

large. However, given the fact that the time t required to run a simulation of N pillars scales as $\sim t^N$, computational hardware becomes the limiting factor. We found simulation samples with 900 pillars to be a reasonable tradeoff in terms of accuracy and performance. Improvements are possible, primarily through the increase of computational power, the use of periodic boundary conditions, but possibly also by incorporating cutoff length in the algorithm, beyond which pillar pair interactions are no longer taken into account.

Each of these suggestions has advantages and disadvantages. An exponential increase in computational power should improve throughput speeds at a linear rate with regards to N. Moore's law predicts a duplication in the number of transistors in an integrated circuit approximately every two years [16], which is currently still valid [17]. This means that over time, more extensive simulations can be performed. Since our results suggest that edge effects are a key factor in determining adhesive performance, periodic boundaries should not be used in all dimensions, but could be employed in one direction to simulate an (infinitely) long sample, restricted only in width. An advantage of a cutoff length is that the number of pillar-pillar interactions is drastically reduced across the sample, but a drawback is that one needs to be careful again with early optimisation, as satisfactory results obtained this way for one geometry might not reflect on other sample geometries, sizes, or pillar distributions. This runs the risk of finding later results to require additional fine-tuning of the algorithm, which then needs to be applied in retrospect to the already carried out simulations, although this is to some extent also true for improvements in laboratory protocols.

6.2 Hydrogels

The introduction to this thesis stated that for wetting of soft materials, molecular effects are systematically underestimated. We attempted to characterise various static and dynamic wetting properties of gels, both for surface-active as well as for surface-inactive gels, and for various functionalised gels. In agreement with earlier studies [18], we found that surface active gels such as pNIPAAm have the ability to stabilise out-of-equilibrium contact angles, resulting in significant contact angle hysteresis, unlike for instance the not surface-active pAAm gels. We related the observed contact angle hysteresis to polymer adsorption at the contact line.

If polymer chains adsorb to the water-air or water-oil interface close to the contact line, advancing the contact line requires desorption of these polymer chains. Polymer desorption, in particular for long dangling chains, is known to be a slow process [19]. This desorption rate is related to chain length. To test the hypothesis that contact angle hysteresis is caused by polymer adsorption to and desorption from the contact line, we followed the relaxation of a 1,8-dibromooctane droplet at a 0.5 % crosslinked

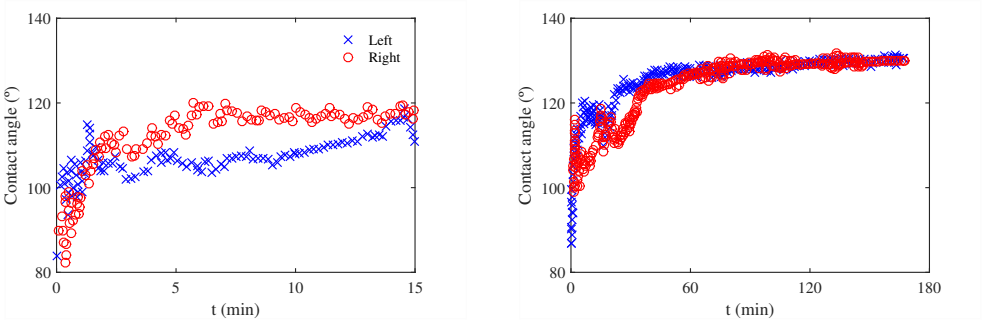

Figure 6.3 – Relaxation of pinned contact lines. (a) The initial and (b) full relaxation curves for the left and right contact angle of a dibromooctane droplet at a 0.5 % crosslinked poly(*N*-isopropylacrylamide) hydrogel, followed for approximately 3 h.

poly(*N*-isopropylacrylamide) gel surface. Figure 6.3 shows the left and right contact angle of this droplet, separated in a graph highlighting the initial relaxation and an overview of relaxation over a period of almost three hours. The out-of-equilibrium droplet is prepared by deflating a 20 µL droplet, until a transient contact angle of about 80° is reached. We observe that relaxation takes place in two regimes: a fast regime with a timescale in the 10 s order of magnitude, and a slow regime, with a timescale in the order of one hour. We attempt to fit a biexponential curve, according to

$$\alpha(t) = \alpha_{\text{end}} - A \exp\left(\frac{1}{\tau_{\text{slow}}}\right) - B \exp\left(\frac{1}{\tau_{\text{fast}}}\right), \tag{6.1}$$

where α the contact angle and τ a factor for the timescale of relaxation. Fits for these two graphs result in the following values: α_{end} =129.6°–130.7°; τ_{fast} = 2.2–60.5 s, and τ_{slow} = 28–35 min. Especially the large spread in τ_{fast} requires a more thorough investigation; we suspect that initial environmental conditions or local features play a decisive role for this parameter. The smaller range in the long timescale parameter could indicate that the long-term relaxation is less affected by initial conditions, or that localised differences average out. This test was performed on only one gel; a suggestion for future research is to study polymer adsorption and desorption kinetics on a range of gels or polymer brushes with different chain lengths, in order to systematically quantify this effect.

We attempted to synthesise three different functionalised gels: gels with permanent charge, acid-functionalised, and base-functionalised gels. The synthesis of charged and base-functionalised hydrogels was successfully demonstrated in Chapter 3. We have shown that with our radical polymerisation method it was not possible

to obtain an acid-functionalised gel using methacrylic acid as a copolymer, probably due to deactivation of the radical initiator TEMED in the sligthly acidic synthesis medium. Literature reports the synthesis of gold-pNIPAAm-acrylic acid nanoparticles, however, using an APS-initiated reaction [20]. This approach could be tried for our macroscopic gels as well, but care should be taken to also attempt this polymerisation protocol for the base-functionalised and non-functionalised hydrogel, in order to exclude any differences potentially brought forward by the change in protocol.

Our contact angle hysteresis results showed somewhat large error bars, potentially obscuring minute differences between samples. A possible reason for these measurement errors is the limitation of the contact angle measurement setup. The Krüss setup used for our measurements is an optical device that takes side view images of a droplet or bubble on a substrate. The supplied contact angle analysis software is able to fit the droplet shape with high accuracy, but due to the soft gel surface not always being perfectly flat or level, the baseline detection can be slightly more complex, resulting in small experimental errors. Also, because the device essentially shows a planar section of the droplet, only the left and right contact angle can be measured. When one of these cannot be fitted for a variety of reasons, half of the acquired data is lost. An improvement in experimental accuracy and reproducibility could be made by changing to a device capable of measuring a 360° contact angle.

6.3 Colloids at anisotropically curved interfaces

Our work in Chapters 4 and 5 describes our effort to validate a literature prediction for power law scaling of the colloid pair interaction potential at anisotropically curved interfaces [21] for two distinct colloidal systems. We indeed found scaling of the interaction potential U with the deviatoric curvature of the interface $\mathcal{D}$, but to a lower extent than the predicted power law scaling. These results were described in Chapter 4, where we studied a system of spherical microgel core-shell colloids at mineral oil/water interfaces.

For this system, with an estimated particle Young's modulus $E = 2 \times 10^4\,\mathrm{N\,m^{-2}}$ and an oil/water surface tension of $40\,\mathrm{N\,m^{-1}}$, we arrive at an estimated elastocapillary length $L_{\mathrm{ec}} = 2 \times 10^{-6}\,\mathrm{m}$ for the microgel particles, or slightly larger than the particle diameter. The indication of an elastocapillary length in or near the same order of magnitude as the particle is significant, and we speculate that this has influenced our results. If the particles were indeed inflated to about twice their synthesis diameter, we expect steric repulsion to play a more significant part already at larger separation, reducing the observed attractive interaction. Indeed, we found that the average equilibrium distance for these particles is approximately equal to two times their diameter.

Moreover, these particles are shown to change shape as they adsorb to oil/water

interfaces [22], which in turn could affect the magnitude of interface deformation required to maintain a constant contact angle. Nevertheless, if the particle swelling or deformation is solely determined by the particle stiffness and relative surface tensions, its effect on interface deformation is a constant, independent of interface curvature. As a result, an interface with a stronger anisotropic curvature will still require a greater deformation to maintain a constant contact angle. This was convincingly demonstrated in our experiments, as we found a positive correlation between the interface curvature and particle interaction potential, albeit lower than the prediction.

We investigated a secondary system, based on solid silica colloids. It was previously reported that these colloids also adsob to oil/water interfaces if ionic liquid is added to the oil phase [23]. We calculated the elastocapillary length for these particles to be less than a picometer, several orders of magnitude smaller than the particle diameter. Theoretically, this should result in a less complicated particle interaction profile. Initial results indicated that these particles indeed adsorb to oil/water interfaces and show attractive interactions, but also that these interactions are significantly shorter ranged and less specific than those observed for microgel particles. With hindsight, the 'less complicated' solid particle system proposed in Chapter 5 is actually more complicated than the microgel particle system in Chapter 4. The significant differences observed between these two systems, both of them based on spherical colloids of approximately identical dimensions, both adsorbed to an oil/water interface, suggests that there may not be a generic effect of interface curvature, or at least that this is not the exclusive factor contributing to colloidal self-assembly for these systems. Although we found that the magnitude of curvature anisotropy does influence particle interactions in both studied systems, there are other indications that several other parameters also interact, including but not limited to a certain fluorescent label for the oil phase. This oversight stresses the importance of careful experimental design.

A redesign of the system should take these factors into account: preferably, particles ought to be as rigid as possible, while no additives should be required to enable spontaneous anchoring of particles to the oil/water interface. A hybrid silica-microgel could potentially be employed, combining the surface-active properties of the microgel shell with a solid core, limiting the elastocapillary length. If possible, fluorescent markers free in solution, such as those used to mark our oil phases, should be avoided. If this is not possible, they should be checked for surface-active properties. In our experiments, the deviatoric curvature of the interface was a semi-controlled variable, in that we had access to channels of different widths. Narrow channels allow for a greater maximum curvature, while wider channels have a larger surface area, thus enabling a larger field-of-view and generally being more versatile. However, the actual interface curvature also depends on the amount of oil deposited into the channel, as well as the surface tension. It would be ideal to design an experiment where the curvature of the interface is predetermined, so that no label is required

to find the actual interface curvature. A suggestion for future research is to develop a system in which the interface curvature is (continously) variable, such that one could study the effect of changing interface curvature on the strength and stability of particle interactions and clusters. Microfluidics potentially fill this niche: if a channel is connected to an oil pump, the oil level and thereby the interface curvature can be adjusted during the experiment.

The imaging methodology poses a significant limitation in the research described in Chapters 4 and 5. While confocal fluorescent microscopy offers excellent contrast for imaging individual particles, the technology is inherently slow. This disadvantage can be mitigated to some extent by carefully aligning the (rectangular) samples in the line scanning direction, and by reducing the size and resolution of the acquisition window. By using an optical grating instead of a line scanner, a significant breakthrough in acquisition speed is achieved, but we find that this affects the image quality to some extent.

Considering the significance of short timescales in this experiment, we chose to discard spatial resolution in favour of time resolution. A potentially beneficial technique is holograhic microscopy [24–27]. Here, a collimated laser beam illuminates particles in a suspension. The interference of light scattered by the particles with the unscattered light from the laser beam creates holographic patterns, as illustrated in Figure 6.4. The lateral position of a particle can be accurately determined from the center of the interferogram, while the vertical position can be calculated from the intensity difference and spacing between lines of constructive and destructive interference. It has been demonstrated that holographic microscopy can accurately track single colloidal particles in three dimensions [25, 26], but significant effort is also invested in extending the technology to allow tracking of multiple particles or particle clusters [27, 28].

(a) (b)

Figure 6.4 – Holographic microscopy of a single particle. (a) A collimated laser beam (solid arrows) illuminates a particle. The scattered light of this particle (dashed lines) interferes with the planes of the unscattered light beam (solid lines). This hologram can be captured by a detector at the bottom of this setup. (b) A sample hologram, reproduced from [27].

References

[1] E. Kroner, R. Maboudian, and E. Arzt. Adhesion characteristics of pdms surfaces during repeated pull-off force measurements. *Advanced Engineering Materials*, **2010**. *12*, 398–404. doi:10.1002/adem.201000090.

[2] C. Greiner, A. Del Campo, and E. Arzt. Adhesion of bioinspired micropatterned surfaces: Effects of pillar radius, aspect ratio, and preload. *Langmuir*, **2007**. *23*, 3495–3502. doi:10.1021/la0633987.

[3] T. Thomas and A. J. Crosby. Controlling Adhesion with Surface Hole Patterns. *The Journal of Adhesion*, **2006**. *82*, 311–329. doi:10.1080/00218460600646610.

[4] L. Shen, N. J. Glassmaker, A. Jagota, and C.-Y. Hui. Strongly enhanced static friction using a film-terminated fibrillar interface. *Soft Matter*, **2008**. pp. 618–625. doi:10.1039/b714737f.

[5] K. Autumn. Gecko adhesion: Structure, function, and applications. *MRS Bulletin*, **2007**. *32*, 473–478. doi:10.1557/mrs2007.80.

[6] S. Akerboom, J. Appel, D. Labonte, W. Federle, J. Sprakel, and M. Kamperman. Enhanced adhesion of bioinspired nanopatterned elastomers via colloidal surface assembly. *Journal of the Royal Society, Interface / the Royal Society*, **2015**. *12*, 20141061. doi:10.1098/rsif.2014.1061.

[7] H. E. Bakker, S. B. Lindström, and J. Sprakel. Geometry- and rate-dependent adhesive failure of micropatterned surfaces. *Journal of Physics: Condensed Matter*, **2012**. *24*, 065103. doi:10.1088/0953-8984/24/6/065103.

[8] S. Hu and Z. Xia. Rational design and nanofabrication of gecko-inspired fibrillar adhesives. *Small*, **2012**. *8*, 2464–2468. doi:10.1002/smll.201200413.

[9] M. Kamperman, E. Kroner, A. Del Campo, R. M. McMeeking, and E. Arzt. Functional adhesive surfaces with "Gecko" effect: The concept of contact splitting. *Advanced Engineering Materials*, **2010**. *12*, 335–348. doi:10.1002/adem.201000104.

[10] C. Poulard, F. Restagno, R. Weil, and L. Léger. Mechanical tuning of adhesion through micro-patterning of elastic surfaces. *Soft Matter*, **2011**. *7*, 2543. doi:10.1039/c0sm01099e.

[11] M. D. Bartlett, A. B. Croll, and A. J. Crosby. Designing bio-inspired adhesives for shear loading: From simple structures to complex patterns. *Advanced Functional Materials*, **2012**. *22*, 4985–4992. doi:10.1002/adfm.201201344.

[12] A. Jagota and C.-Y. Hui. Adhesion, friction, and compliance of bio-mimetic and bio-inspired structured interfaces. *Materials Science and Engineering: R: Reports*, **2011**. *72*, 253–292. doi:10.1016/j.mser.2011.08.001.

[13] E. Ginebre and S. B. Lindström. *Geometry-dependence of the adhesive strength of biomimetic, micropatterned surfaces*. Master's thesis, Linköping University, **2012**.

[14] M. K. Kwak, C. Pang, H. E. Jeong et al. Towards the next level of bioinspired dry adhesives: New designs and applications. *Advanced Functional Materials*, **2011**. *21*, 3606–3616. doi:10.1002/adfm.201100982.

[15] M. Röhrig, M. Thiel, M. Worgull, and H. Hölscher. 3D Direct laser writing of nano- and microstructured hierarchical gecko-mimicking surfaces. *Small*, **2012**. *8*, 3009–3015. doi:10.1002/smll.201200308.

[16] G. E. Moore. Cramming more components onto integrated circuits. *Electronics*, **1965**. *38*.

[17] Online. https://www.karlrupp.net/2018/02/42-years-of-microprocessor-trend-data/.

[18] M. A. Cohen Stuart, W. M. de Vos, and F. A. M. Leermakers. Why surfaces modified by flexible polymers often have a finite contact angle for good solvents. *Langmuir*, **2006**. *22*, 1722–1728. doi:10.1021/la052720v.

[19] J. F. Douglas, H. E. Johnson, and S. Granick. A simple kinetic model of polymer adsorption and desorption. *Science*, **1993**. *262*, 2010–2012. doi:10.1126/science.262.5142.2010.

[20] M.-Y. Park, S. Lim, and S.-W. Lee. Relative Parameter Contributions for Encapsulating Silica-Gold Nanoshells by Poly(N-isopropylacrylamide-co-acrylic acid) Hydrogels. *Macromolecular Research*, **2009**. *17*, 307–312.

[21] D. Ershov, J. Sprakel, J. Appel, M. A. Cohen Stuart, and J. van der Gucht. Capillarity-induced ordering of spherical colloids on an interface with anisotropic curvature. *Proceedings of the National Academy of Sciences of the United States of America*, **2013**. *110*, 9220–4. doi:10.1073/pnas.1222196110.

[22] O. S. Deshmukh, D. van den Ende, M. A. Cohen Stuart, F. Mugele, and M. H. G. G. Duits. Hard and soft colloids at fluid interfaces: Adsorption, interactions, assembly & rheology. *Advances in Colloid and Interface Science*, **2014**. *222*, 215–227. doi:10.1016/j.cis.2014.09.003.

[23] H. Monteillet, M. Workamp, J. Appel, J. M. Kleijn, F. A. M. Leermakers, and J. Sprakel. Ultrastrong Anchoring Yet Barrier-Free Adsorption of Composite Microgels at Liquid Interfaces. *Advanced Materials Interfaces*, **2014**. *1*. doi: 10.1002/admi.201300121.

[24] S.-H. Lee and D. G. Grier. Holographic microscopy of holographically trapped three-dimensional structures. *Optics express*, **2007**. *15*, 1505–1512. doi:10.1364/OE.15.001505.

[25] S.-H. Lee, Y. Roichman, G.-R. Yi et al. Characterizing and tracking single colloidal particles with video holographic microscopy. *Optics Express*, **2008**. *0*, 1–6. doi:10.1364/OE.15.018275.

[26] F. C. Cheong, B. J. Krishnatreya, and D. G. Grier. Strategies for three-dimensional particle tracking with holographic video microscopy. *Optics express*, **2010**. *18*, 13563–13573. doi:10.1364/OE.18.013563.

[27] J. Fung, R. W. Perry, T. G. Dimiduk, and V. N. Manoharan. Imaging multiple colloidal particles by fitting electromagnetic scattering solutions to digital holograms. *Journal of Quantitative Spectroscopy and Radiative Transfer*, **2012**. *113*, 2482–2489. doi:10.1016/j.jqsrt.2012.06.007.

[28] P. Memmolo, L. Miccio, M. Paturzo et al. Recent advances in holographic 3D particle tracking. *Advances in Optics and Photonics*, **2015**. *7*, 713. doi: 10.1364/AOP.7.000713.

Summary

This thesis describes our work on soft matter, divided in three parts and four chapters.

In Chapter 2, we investigate and improve the effects of surface patterning on adhesive properties. We create these adhesives by patterning silicone rubber (PDMS) with pillars of approximately 20 µm diameter, and measure adhesive properties against a glass substrate. We distinguish two classes of patterned adhesives in this research: for the first part we look at samples with varying degrees of feature clustering, while for the second part we investigate samples with different patterning geometries. We look at samples with square, hexagonal, or random geometry.

Literature suggests a beneficial effect of patterning towards adhesive properties. One reason for an improved effectiveness of a patterned adhesive, compared to a monolithic sample, is as a result of contact splitting, which improves sample-substrate compliance, and therefore increase the effective contact area. However, from our investigations we conclude that it is difficult to prove this theory. We find that many trivial experimental details affect the outcome of our experiments. We describe our efforts to control these parameters. Regardless, we find no statistically significant impact of either clustering or ordered versus disordered patterning methods on adhesive properties within the experimental noise. We perform computer simulations to further investigate patterned adhesives. These simulations show that clustering can yield an approximately 10 % improvement in adhesive performance, but only for cluster sizes significantly larger than those investigated in our earlier experiments.

In Chapter 3, we investigate the static and dynamic wetting properties of water-swollen poly(acrylamide) (pAAm) and poly(N-isopropyl acrylamide) (pNIPAAm) hydrogels, in air and under water. We look at the influence of polymer chemistry on contact angle equilibrium, the influence of polymer chemistry on contact line dynamics, and the influence of polymer architecture on contact line dynamics. We find that our hydrogels have a constant static contact angle of air or 1,8-dibromooctane at the hydrogel/water interface, independent of hydrogel composition.

We perform dynamic contact angle measurements to further investigate hydrogel wetting. We find that surface-active pNIPAAm gels can stabilise out-of-equilibrium droplets for an extended period of time, unlike pAAm hydrogels. We also show that

pNIPAAm hydrogels show a significant contact angle hysteresis.

In the remainder of this chapter, we look at charged hydrogels. We find that the presence of charged building blocks significantly affects hydrogel properties, such as a complete absence of contact angle hysteresis in permanently charged pNIPAAm hydrogels. We also investigate pH-switchable hydrogels by co-polymerising NIPAAm with 2-aminoethyl methacrylate. These gels acquire charge in an acidic environment, and neutralise in a basic environment. We show that these gels have wetting properties comparable to that of neutral pNIPAAm hydrogels, regardless of the charge state. However, hydrogel swelling is significantly affected by the environmental parameters.

In Chapter 4, we investigate the self-assembly of spherical, colloidal silica/microgel core-shell particles at anisotropically curved oil-water interfaces. From long- and short-range colloid interactions, we construct the full pair interaction potential, and show that this potential is strongly dependent on the deviatoric curvature of the interface. We observe the formation of two-dimensional fractal structures with quadrupolar symmetry.

This colloidal interaction potential indicates that the softness of and charge on the particles may generate a subtle and complex interaction potential. To further investigate this system, we focus our work in Chapter 5 on solid colloidal particles instead. We show that unmodified silica particles are capable of adsorbing spontaneously to oil-water interfaces, if the oil interface contains a small amount of ionic liquid. Unlike the microgel system described above, pair interactions for the silica system are generally much weaker. As a result, only small particle clusters are observed, and particles frequently escape after initial 'bonding'. Although the aforementioned quadrupolar symmetry is also present in this case, we regularly find particles in triangular clusters, suggesting a deeper secondary minimum in the interaction potential, which may be stronger than the quadrupolar repulsion that is expected at non-right angles.

Samenvatting

Dit proefschrift beschrijft ons onderzoek naar zachte materie, verdeeld in drie delen en vier hoofdstukken.

In Hoofdstuk 2 kijken we naar het effect van patronen op adhesieve eigenschappen, en proberen deze eigenschappen te verbeteren. Deze adhesieven maken wij door pilaartjes van ongeveer 20 µm diameter aan te brengen in siliconenrubber (PDMS), en de kleefkracht bepalen we aan de hand van metingen tegen een glazen oppervlak. We onderscheiden twee klassen van adhesieven: eerst kijken we naar monsters met verschillende mate van clustervorming, en daarna kijken we naar monsters met patronen in verschillende geometrieën. We kijken naar patronen met vierkante, zeshoekige, of willekeurige geometrie.

In de literatuur vinden we beschreven dat patroonvorming voordelig zou zijn voor adhesieve eigenschappen. Een van de redenen van verbeterde adhesie van een monster met een patroon ten opzichte van een monolithisch monster is het resultaat van contactsplitsing. Dit verbetert de hechting van het monster aan een oneffen oppervlak, waardoor effectief een groter contactoppervlak ontstaat. Echter, uit ons werk bijkt dat dit lastig te bewijzen is. We beschrijven hoe verschillende triviale experimentele details invloed kunnen hebben op de uitkomst van een onderzoek. We beschrijven onze pogingen om deze eigenschappen naar onze hand te zetten en hun invloed te minimaliseren. Desalniettemin vinden we geen statistisch significant effect van clustervorming of patroongeometrie op adhesieve eigenschappen, binnen de experimentele ruis. We doen computersimulaties om adhesieven met een patroon verder te onderzoeken. Deze simulaties tonen aan dat de adhesie van een geclusterd patroon een verbetering van ongeveer 10 % kan bereiken, maar alleen voor clusters die aanzienlijk groter zijn dan die in ons eerdere experiment.

In Hoofdstuk 3 kijken we naar de statische en dynamische bevochtigingseigenschappen van in water gewelde poly(acrylamide) (pAAm) en poly(N-isopropyl acrylamide) (pNIPAAm) hydrogelen, aan de lucht en onder water. We onderzoeken de invloed van de chemische samenstelling van deze hydrogelen op de evenwichtscontacthoek, de invloed van de samenstelling op de dynamische eigenschappen van de contacthoek, en de invloed van polymeerarchitectuur op de dynamische eigenshappen

van de contacthoek. We tonen aan dat onze hydrogelen een constante evenwichtscontacthoek hebben van lucht of 1,8-dibroomoctaan aan het gel/water-grensvlak, onafhankelijk van de samenstelling van de hydrogel.

We voeren dynamische contacthoekmetingen uit om verder onderzoek te doen naar de bevochtiging van hydrogelen. We tonen aan dat de oppervlakte-actieve pNIPAAm-gelen voor langere tijd in staat zijn een niet-evenwichtscontacthoek te stabiliseren, in tegenstelling tot pAAm hydrogelen. We laten ook zien dat pNIPAAm-hydrogelen een grote contacthoekhysterese vertonen.

In het vervolg van dit hoofdstuk kijken we naar geladen hydrogelen. We komen erachter dat de aanwezigheid van geladen bouwstenen in de hydrogel een significante invloed uitoefent op de eigenschappen van de gel, zoals de afwezigheid van contacthoekhysterese in een geladen pNIPAAm-hydrogel aantoont. Verder kijken we naar pH-gevoelige hydrogelen door pNIPAAm te co-synthetiseren met 2-aminoethyl methacrylaat. Deze gelen krijgen een positieve lading in een zuur milieu, en zijn neutraal in basisch milieu. We laten zien dat deze gelen bevochtigingseigenschappen hebben die vergelijkbaar zijn met die van ongeladen pNIPAAm-hydrogelen, ongeacht of de gel geladen of neutraal is. De lading heeft wel een grote invloed op de zwelling van de gel.

In Hoofdstuk 4 kijken we naar de zelfassemblage van bolvormige colloidale silica/microgel kern-schaaldeeltjes op anisotropisch gekromde olie-watergrensvlakken. We construeren de paarpotentiaal aan de hand van lange- en korte-afstandsinteracties tussen de colloïden. We tonen aan dat deze potentiaal sterk afhankelijk is van de deviatorische kromming van het grensvlak. We observeren de vorming van tweedimensionale fractale structuren met vierkante symmetrie.

Deze interactiepotentiaal toont aan dat de zachtheid en lading van de colloïdale deeltjes mogelijk tot een subtiel-complexe interactiepotentiaal leidt. Om het systeem verder te onderzoeken kijken we in Hoofstuk 5 naar vaste colloïden. We laten zien dat ongewijzigde silicadeeltjes in staat zijn spontaan aan een olie-watergrensvlak te adsorberen, mits de oliefase een klein beetje ionische vloeistof bevat. In tegenstelling tot het microgelsysteem dat we hiervoor beschrijven, vinden we veel zwakkere paarinteracties. Dit heeft tot gevolg dat slechts kleine deeltjesclusters kunnen worden geobserveerd. Ook blijkt vaak dat deeltjes uit een cluster ontsnappen na aanvankelijk een ‘binding’ te zijn aangegaan. Hoewel de vierkante symmetrie ook in dit systeem duidelijk aanwezig is, vinden we ook vaak deeltjes in driehoekige clusters. Dit suggereert dat er mogelijk een dieper tweede minimum in de interactiepotentiaal aanwezig is, die sterker is dan de vierhoekige afstoting die we verwachten voor niet-rechte hoeken.

Appendix A

Determination of interface curvature

The curvature of oil-water interfaces was determined semi-automatically using ImageJ. This procedure requires the user to import a Z stack as an image sequence. User input is provided through dialog boxes. We found that in some low quality images, the application of a Gaussian blur can improve the quality of the fit. The default blur radius is set to 0 (no blur). After this, the user has the possibility to adjust the image threshold, if needed.

After a number of operations, the user is required to select the arc representing the oil/water interface. The following measurement parameters need to be set prior to running the circle fitting algorithm:

- Area
- Shape descriptors

Other parameters are optional. By default, ImageJ only measures the visible area of any selection. The Shape descriptor includes the value of this fraction. The total area of the selection then is Area/Fraction.

Curve fitting algorithm

```
//Procedure:
run("Select None");
run("Reslice [/]...", "output=1.000 start=Left avoid");
run("Z Project...", "start=1 stop=9999 projection=
    [Sum Slices]");
run("Save");
blur = getNumber("Blur radius (0 if not stripey): ",0);
run("Gaussian Blur...", "sigma="+blur);
run("8-bit");
run("Find Edges");
//now some interaction:
run("Threshold...");
setAutoThreshold("MaxEntropy dark");
waitForUser('Adjust threshold, then click OK')
run("Convert to Mask");
run("Canvas Size...",
    "width=5000 height=5000 position=Center zero");
//Select the line
setTool("wand");
waitForUser('Select the curve, then click OK');
// Manually select line if it fails,
// then run below to fit and measure circle
run("Area to Line");
run("Fit Circle");
run("Measure");
waitForUser('Done')
close();
close();
close();
```

Acknowledgements

As everyone knows, the acknowledgements are the best read part of any thesis, in my experience followed closely by a glance at the figures, followed by perhaps the summary and a brief read of the more interesting scientific content.

First I would like to thank all the scientific and support staff at Physical Chemistry and Colloid Science, for without you there is no research going to happen any time soon. Thank you for discussions, valuable input, and assistance with the wealth of experimental setups and administrative tasks required to perform scientific research.

Some names that I would like to call out are Aljosha, for your contribution to the wetting of soft gels described in Chapter 3, and Dmitry, for your initial assistance with the confocal setup and all those peculiar particle interactions, as well as Jeroen, Ties and Hélène for supplying me with various particles and oils to deposit at interfaces.

Gosia, Hanne, Natalia and Wolf, I think we had a lot of fun organising the UK PhD-trip. Unfortunately, the gold medal for best PhD trip was already taken, but I think we did a good job regardless.

Nadia and Hélène, my office mates for two years each: thank you for sharing your office time with me, keeping my love for (and practice of) the French language alive.

Special thanks go (of course, who didn't see this coming) to Lennart. Thank you for just being there, allowing me to become my weird self to an even higher degree than before, and for the lasting friendship.

Thanks to all the other wonderful people I met in Wageningen. I cannot mention all of you in particular, for I would certainly miss names, but you made me feel very comfortable in the small, international world of PhD research in Wageningen, always up for potluck dinners and other friendly get-togethers.

Mijn dank gaat ook uit naar mijn familie. Hoewel het niet altijd makkelijk is, voel ik toch jullie onvoorwaardelijke steun. Als verste nestvlieder is dat toch best wel speciaal. Dank voor jullie steun aan mij in het algemeen, en jullie getoonde interesse in mijn werk in het bijzonder.

عمیر احمد ، میرا پہلا ہونے کے لیے شکریہ ۔ ہمارے پاس ہمارے اختلافات تھے ، اور زندگی کی منصوبہ بندی کے طور پر نہیں جانا تھا ، لیکن مجھے لگتا ہے کہ ہم نے ایک دوسرے کے لئے بہترین تھا. خاص طور پر میں اپنے دوسرے سال میں چھوڑنے کی حمایت کرنے کے لئے آپ کا شکریہ ادا کرنا چاہتا ہوں. آپ کی حمایت کے بغیر ، یہ مقالہ نہیں بن گا جو یہ ہے.

泽明，埃迪，露露...最后但并非最不重要的一点，感谢您在我身边并让我成为我自己。

About the author

Maarten van Heek was born on the 2nd of July 1987 in Rijssen, The Netherlands. In 2005 he graduated from the Jacobus Fruijtier Scholengemeenschap in Apeldoorn. That year he started studying Chemistry at the Universiteit Utrecht. He wrote a bachelor thesis on the effects of acid and bace leaching to induce mesopore formation in mordenite at the Inorganic Chemistry and Catalysis group under supervision of Adri van Laak and Prof. Krijn de Jong. For his master thesis thesis he did a project on catalytic oxidation of cyclohexane in the same group, under supervision of Bart Hereijgers and Prof. Bert Weckhuysen. He did an intership at AkzoNobel Chemicals in Deventer, The Netherlands, under supervision of Henk-Jan van Manen (AkzoNobel) and Andrew Beale (UU), on a quantitative application of Raman spectroscopy in slurries.

In April 2012 he started as a PhD candidate at the department of Physical Chemistry and Soft Matter at Wageningen University under supervision of Dr Joris Sprakel, with Prof. Jasper van der Gucht as his promotor. His research about Soft Matter at Interfaces is described in this thesis.

Overview of completed training activities

Course, meeting	Organising institute	Location	Year
Discipline specific activities			
Dutch Soft Matter Meeting	Dutch universities	Amsterdam	2012
Advanced Soft Matter	PCC	Wageningen	2012
Dutch Soft Matter Meeting	Dutch universities	Amsterdam	2012
Physics@FOM	FOM	Veldhoven	2013 [a]
Droplets 2013	IUSTI Marseille	Marseille (F)	2013
Han-sur-Lesse Winterschool	Dutch universities	Han-sur-Lesse (B)	2014
IACIS2015	Max Planck Institute for Polymer Research & GDCh	Mainz (D)	2015 [b]
General courses			
PhD competence assesment	WGS	Wageningen	2013
Scientific Writing	WU Language Centre	Wageningen	2014
Project and time management	WGS	Wageningen	2014
Programming in Python	INF	Wageningen	2014
Career perspectives	WGS	Wageningen	2015

a. Poster presentation
b. Oral presentation

Optionals			
Project proposal	PCC	Wageningen	2012
Weekly group meetings	PCC	Wageningen	-
PhD study tour USA	PCC	Wageningen	2013 [ab]
Statistical Thermodynamics	PCC	Wageningen	2013
Organisation PhD trip	PCC	Wageningen	2015
PhD study tour UK	PCC	Wageningen	2015 [ab]

[a.] Poster presentation
[b.] Oral presentation

Cover design by Maarten van Heek
Printed by proefschriftmaken.nl on FSC-certified paper